Published in final edited form as:
Coord Chem Rev. 2010 August 1; 254(15-16): 1769–1802. doi:10.1016/j.ccr.2009.12.023.

Electrochemistry of redox-active self-assembled monolayers

Amanda L. Eckermann, **Daniel J. Feld**, **Justine A. Shaw**, and **Thomas J. Meade**

Abstract

Redox-active self-assembled monolayers (SAMs) provide an excellent platform for investigating electron transfer kinetics. Using a well-defined bridge, a redox center can be positioned at a fixed distance from the electrode and electron transfer kinetics probed using a variety of electrochemical techniques. Cyclic voltammetry, AC voltammetry, electrochemical impedance spectroscopy, and chronoamperometry are most commonly used to determine the rate of electron transfer of redox-activated SAMs. A variety of redox species have been attached to SAMs, and include transition metal complexes (e.g., ferrocene, ruthenium pentaammine, osmium bisbipyridine, metal clusters) and organic molecules (e.g., galvinol, C_{60}). SAMs offer an ideal environment to study the outer-sphere interactions of redox species. The composition and integrity of the monolayer and the electrode material influence the electron transfer kinetics and can be investigated using electrochemical methods. Theoretical models have been developed for investigating SAM structure. This review discusses methods and monolayer compositions for electrochemical measurements of redox-active SAMs.

1. Introduction

Electron transfer has been extensively studied in the context of biological processes, sensors, artificial photosynthesis, and molecular electronics [1–23]. Marcus theory predicts that the rate of electron transfer between a donor and an acceptor is dependent on the Gibbs free energy (ΔG), reorganization energy (λ), temperature (T) and the electronic coupling between a electron donor and acceptor (H_{AB}) [24]. A significant body of work has been reported that examines each of these variables in the context of long-range biological electron transfer, molecular systems including artificial photosynthetic centers, highly conjugated molecular wires, and mixed valence systems [6–8,10,21,25–34]. Focus on electron transfer kinetics has greatly increased in the field of molecular electronics (rectifiers, junctions, switches, transistors, sensors, etc.), to delineate electron transport between electrodes through molecular bridges [3,6,20,35,36].

Recent interest in surface (electrode) modification has led to the study of electron transfer using electrodes modified with self-assembled monolayers (SAMs) [1,37–43]. SAMs provide an excellent platform for exploiting electrochemistry to study electron transfer processes because each variable (ΔG, H_{AB}, λ, T) can be controlled experimentally. For example, SAMs allow double layer effects to be controlled and eliminate problems associated with diffusive mass transport. Redox-modified SAMs have been designed to systematically study the correlation of ΔG, λ, and H_{AB} to SAM components. These components include the distance between the

redox center and the electrode, the molecular environment of the redox center, and bridge structure (Figure 1.1) [1,44,45].

A variety of electrochemical techniques are used to probe each of these electron transfer variables. The bridge controls the distance and coupling between the redox center and the electrode. Reorganization energy can be probed by changing the molecular environment of the redox center by using a variety of solvents or by changing the SAM composition. The effects of changing each of these variables can be quantified using electrochemical techniques.

SAMs provide an excellent platform for using electrochemistry to study long-range electron transfer events on electrodes. However, the multitude of electrochemical techniques available (and subsequent data analysis) can be daunting to novices of the field. In this review, we describe the most commonly used electrochemical methods to measure k_{ET}, λ, H_{AB} using redox-modified SAM systems. These analytical methods include cyclic voltammetry, AC voltammetry, chronoamperometry, and electrochemical impedance spectroscopy. Each of these methods has advantages and limitations that will be described in Section 2. Further, a detailed description of data analysis for each of these techniques will be described. Table 1.1 lists k_{ET} of ferrocene alkane thiols in SAMs for various lengths of the alkane bridge and the method of determining k_{ET} is listed for comparison.

We review *additional* aspects of SAM electrochemistry that are critical to acquiring reliable and accurate ET measurements. The fundamental properties of redox active molecules are discussed in terms of SAM applicability. The formation and characterization of the SAM structure is discussed, along with the variety of compositions of bridges connecting the electrode and redox centers. The qualities of various electrode materials are described and we include a summary of computational approaches to modeling of SAMs.

2. Electrochemical methods

There are four electrochemical techniques typically used for determining k_{ET} in redox-active SAMs; cyclic voltammetry (CV), chronoamperometry (CA), alternating current voltammetry (ACV), and electrochemical impedance spectroscopy (EIS). In this section we describe the basic theory behind each method and outline the advantages and disadvantages of each approach. Methods used to a lesser extent such as indirect laser induced temperature jump (ILIT) and scanning electrochemical microscopy (SECM) are included.

2.1. Cyclic voltammetry (CV)

The most widely recognized electrochemical technique, cyclic voltammetry (CV) is a potential sweep method where the potential is varied and the current is measured of a redox event [46–50]. CV does not require expensive or highly sophisticated instrumentation, and is therefore widely available. This method is less sensitive to kinetic heterogeneity than other electrochemical techniques. Kinetic heterogeneity is a distribution of electron transfer rates due to variations in the molecular environment of the redox center caused by SAM defects. Using the mathematical models described below, CV can be used to determine k_{ET}, λ, and H_{AB}.

A wealth of information can be obtained from a cyclic voltammogram that can be used to evaluate ET of monolayer surface-bound electroactive species. (Figure 2.1) The background and peak currents, and the peak potentials are of importance in determining the rate constant of electron transfer reactions. The integrity of the monolayer is important because disorder can cause a dispersion of measured rate constants. For the measurement of k_{ET}, the redox centers should ideally be isolated from one another and local molecular environments homogeneous. Figure 2.1 shows the relevant parameters that can be determined from CV data.

The background current (charging or capacitive current, i_{ch}) can be correlated to the thickness of the SAM. (Figure 2.1) The double layer capacitance, C_{DL}, is often normalized to the surface area, A_{SUR}, for comparison. The effects of disorder in the monolayer on the capacitance will be discussed further in section 5.2.

$$\frac{i_{ch}}{A_{SUR}} = \frac{C_{DL}}{A_{SUR}} \nu \tag{2.1}$$

The faradaic current (i_p, Figure 2.1) is directly proportional to the scan rate, ν, as described by Equation 2.2 [46]. The surface coverage, Γ, can be determined from the slope of the line of i_p vs. ν. This value is often compared to a theoretical maximum based on the molecular surface area of the adsorbate as in Equation 2.2.

$$i_p = \frac{n^2 F^2}{4RT} \nu A_{SUR} \Gamma \tag{2.2}$$

The peak shape is diagnostic of the homogeneity of the monolayer and can be evaluated by the full width at half of the peak maximum height (FWHM, Figure 2.1) as described by Equation 2.3. Values of FWHM that are larger or smaller than theoretical FWHM have been attributed to electrostatic effects incurred by neighboring charged species [46,51,52].

$$FWHM = 3.53 \frac{RT}{nF} = \frac{90.6}{n} \tag{2.3}$$

The redox potential, E^0, is determined from the average of the anodic and cathodic peak potentials, E_{pa} and E_{pc}, and the peak separation, ΔE_p, is calculated by E_{pa}-E_{pc}. As scan rate increases, peak separation increases. At slow scan rates the peak separation is 0 because the redox center is adsorbed onto the electrode and diffusion does not play a role [46].

The amount of charge, Q, that is passed can be determined by integrating the background-subtracted peaks as shown by the shaded area in Figure 2.1. The overpotential, η, is defined according to Equation 2.4 as the difference between peak potential E_p and the formal potential of the complex.[1] For each scan rate, $k_s(\eta)$, the rate constant for electron transfer at a particular overpotential, can be determined from Equation 2.5. A plot of η vs. log $k_s(\eta)$ is known as a Tafel plot and importantly, can be used to determine k_{ET} [38,53]. Fitting this plot using the Marcus density-of-states model will be discussed in Section 2.3.

$$\eta = E_p - E^\circ \tag{2.4}$$

$$k_s = \frac{i_p}{Q} \tag{2.5}$$

[1]The term overpotential is sometimes used to refer to the difference in applied potential and the formal potential of the redox species, as in chronoamperometry. In electrochemical texts, overpotential may refer to the amount by which an activation energy is lowered for a process at an electrode surface. This overpotential decreases the energy barrier that must be overcome and increases the rate of electron transfer.

Experimentally, an initial potential is chosen such that the oxidation state of the redox centers remains unchanged at the onset of a scan. The potential is scanned past the formal potential $E^{0'}$ to a point at which the current returns to baseline. The direction of the scan is then reversed and returned to the initial starting potential. In subsequent experiments, the scan rate is varied to give a range η values that can be used to determine k_{ET}.

In summary, ideal reversible electrochemical behavior results when both the reduced and oxidized form of the redox species are strongly adsorbed to the electrode. The CV shows (1) symmetric peaks, (2) a linear relationship between the peak current and scan rate, and (3) ΔE_p equal to 0 at low scan rates for a completely reversible system. For example, the peak shape for a one electron process, described by the FWHM, should be 90.6 mV at 25 °C (Equation 2.3) [46].

2.2. Laviron method for the determination of k_{ET}

In 1979 E. Laviron published the mathematical treatment for using linear sweep voltammetry to determine k_{ET} of species adsorbed to an electrode [54]. The method is based on the Butler-Volmer approach, and the only experimental data required to use this method are overpotentials (Eq. 2.4).

The Laviron method is widely used for determining the electron transfer rate constant, however, it is subject to a number of constraints that limit its application [54]. First, this method relies on α, the transfer coefficient, which is a measure of the symmetry of the energy barrier of the redox reaction. Ideally, α = 0.5 for all overpotentials, however in many cases α deviates from 0.5. Therefore, determination of α is crucial to finding k_{ET}. To determine α, the peak potential E_p is plotted vs. log ν [54]. E_{pa} and E_{pc} are plotted separately in this way to give two branches. At higher scan rates where η > 100 mV, the data should be a straight line where the slope of the line is given in Equation 2.6.

$$slope = -\frac{2.3RT}{\alpha nF} \tag{2.6}$$

The k_{ET} can be determined by applying the constraint of η = 0 to Equation 2.7 which reduces to Equation 2.8. Determining the x-intercepts of the lines for the anodic and the cathodic branches provides ν_a and ν_c respectively, values that are used in Equation 2.8 to determine k_{ET}.

$$\log k_{APP} = \alpha \log(1-\alpha) + (1-\alpha)\log\alpha - \log\left(\frac{RT}{nF\nu}\right) - \frac{\alpha(1-\alpha)nF\eta}{2.3RT} \tag{2.7}$$

$$k_{ET} = \frac{\alpha nF\nu_c}{RT} = (1-\alpha)\frac{nF\nu_a}{RT} \tag{2.8}$$

2.3. Marcus density of states theory for the determination of k_{ET}

The rate constant of nonadiabatic (weakly coupled) electron transfer between an electron donor A and acceptor B in solution is described by the Marcus semiclassical expression of Equation 2.9. Marcus theory is based on a continuum description of the solvent contribution to the activation energy of ET reactions [55, 58–61]. Free energy curves for electron transfer are shown in Figure 2.2. Constants in the equation are *h* (Planck's constant), R (the ideal gas constant), and k_B (Boltzmann's constant). H_{AB} is the electronic coupling between A and B, λ

is the reorganization energy, and T is temperature. Numerous electron transfer studies have focused on probing electronic coupling by varying the length and the nature of the bridge between the donor and the acceptor (covalent, conjugated, hydrogen bonds, “through space” [1,3,42,45,56,57].

$$k_{ET}=\frac{4\pi^2 H_{AB}^2}{h\sqrt{4\pi\lambda RT}}\exp\left[\frac{-(\Delta G+\lambda)^2}{4\lambda k_B T}\right] \tag{2.9}$$

Reorganization energy is the energy required to reorient all atoms (from equilibrium state to the product state) and consists of two parts: $\lambda = \lambda_i + \lambda_o$. The “inner” contribution λ_i relates the energy required to change bond distances and, in some cases, spin state. The “outer” contribution λ_o relates the energy needed to reorient the solvent and is given by Equation 2.10 This equation uses a simple geometric assumption that the donor and acceptor are spherical bodies and treats the solvent as a dielectric continuum [58–61]. The variables r_A and r_B, are the radii of the redox centers A and B, d is the distance between the redox centers, and ε_{op} and ε_s are the optical and static dielectric constants of the solvent respectively. Determining Marcus's “inverted region” using Eq. 2.9 for the conditions at which $-\Delta G = \lambda$ and the electron transfer rate constant reaches a maximum, is the most experimentally studied role of reorganization energy [19,62–67].

$$\lambda_O=N_A e^2\left(\frac{1}{2r_A}+\frac{1}{2r_B}-\frac{1}{d}\right)\left(\frac{1}{\varepsilon_{op}}-\frac{1}{\varepsilon_s}\right) \tag{2.10}$$

For redox processes at an electrode, a parameterization of the potential dependence of electrochemical rates is shown in equations 2.11 and 2.12. In these equations λ, ε_0, e_0, k_{ET}, k_B, η, and T are respectively, the reorganization energy, static dielectric constant, charge of an electron, equilibrium ET rate at zero applied overpotential, Boltzmann constant, the applied overpotential, and temperature. These are the classical Butler-Volmer equations wherein the activation energies for both the cathodic and anodic rates are assumed to be a linear function of η and a transfer coefficient is assumed to be 0.5 [46,68].

$$k_{ox}=k_{ET}\exp\left[-\frac{\lambda-2e_0\eta}{4k_B T}\right] \tag{2.11}$$

$$k_{red}=k_{ET}\exp\left[-\frac{\lambda+2e_0\eta}{4k_B T}\right] \tag{2.12}$$

At high overpotentials, second order terms of the potential dependence on electrochemical rate constants become significant and Equations 2.11 and 2.12 are no longer valid [68]. Moreover, Butler-Volmer theory does not consider a parabolic reaction surface as is the case in Marcus theory. By approximating the reaction surface as parabolic, the electrochemical analog of the Marcus inverted region can be observed [69,70]. These Marcus rate relations are shown in equations 2.13 and 2.14.

$$k_{ox}=k_{ET}\exp\left[-\frac{(\lambda-2e_0\eta)^2}{4\lambda k_B T}\right] \tag{2.13}$$

$$k_{red}=k_{ET}\exp\left[-\frac{(\lambda+2e_0\eta)^2}{4\lambda k_B T}\right] \quad (2.14)$$

The parabolic potential included in Marcus theory is approximated by a linear function as in the Butler-Volmer approach when $\eta/\lambda << 1$ (for example, the 25 eV curve in Figure 2.3) and Equations 2.13 and 2.14 reduce to 2.11 and 2.12.

Cathodic and anodic rate constants for electron transfer between a redox-active molecule and a metal electrode can be calculated by numerical integration of donor and acceptor levels over a range of energies ε, the energy level relative to the Fermi energy level of a metal [1]. Here, we consider only the cathodic expression for the rate constant since the anodic rate constant expression differs from the cathodic expression only in symmetry.

$$k_{ox}=A\int_{-\infty}^{\infty} d\varepsilon D_{ox}(\varepsilon)\rho(\varepsilon) f(\varepsilon) \quad (2.15)$$

$$D_{ox}(\varepsilon)=\frac{1}{\sqrt{4\pi\lambda k_B T}}\exp\left[-\frac{(\lambda-\varepsilon+e_0\eta)^2}{4\lambda k_B T}\right] \quad (2.16)$$

The Fermi function $f(\varepsilon)$ of the metal is the probability that a given available electron energy state will be occupied at a given temperature [71]. The density of states of the metal $\rho(\varepsilon)$ varies slowly near the Fermi level and is assumed constant over the range of energies used to evaluate the integral [68]. The distribution of electron acceptor levels of the redox center is represented by a Gaussian function $D_{ox}(\varepsilon)$ whose widths are defined as the reorganization energy. The preintegral factor, *A*, includes factors such as electronic coupling, the probability of tunneling through an electronic barrier and surface coverage of redox active sites [72].

If λ is similar in magnitude to the applied potential, a plateau region becomes apparent where increasing η no longer increases the rate (For example, the 0.2 eV–1.0 eV curves in Figure 2.3). Equations 2.15 and 2.16 predict that as η approaches λ (the advent of the inverted region) the rate constants will not continue to increase exponentially as predicted by Butler-Volmer equations, but will reach a maximum when $\eta = \pm \lambda$ [68].

When the $\eta >> \lambda$, the entire distribution of redox active sites overlaps with states in the electrode that are available for electron transfer [68]. Increasing the driving force (and hence η) does not make new states available for electron transfer and does not increase the probability of electron transfer [70]. In the regime where $\eta > \lambda$, the inverted region, the rate constants do not decrease with increasing driving force as expected in molecular donor-acceptor electron transfer. In fact, the rate constants become independent of the driving force [70]. As Weber et al. emphasize, the magnitude of η for which these effects are important is the on the order of λ for a common redox species such as ferrocene. Therefore, these effects require experimental consideration.

In order to determine k_{ET} by fitting simulated CVs to experimental CVs, the following method has been developed. This description is based on the outline given by Eggers et al. for a ferrocene-modified SAM [73]. CVs are simulated using equations 2.17 and 2.18. The current, i, as a function of time, t, during a CV sweep is given by Equation 2.17. Γ_T is the total coverage of Fc and θ_{Fc} is the fractional coverage of the ferrocenium ion (Γ_O/Γ_T). The change in θ_{Fc} with time for oxidation is calculated from equation 2.18. The values of k_O and k_R are determined from Equations 2.20 and 2.21.

$$i(t) = F\frac{d\theta_{Fc}(t)}{dt}\Gamma_T \tag{2.17}$$

$$\frac{d\theta_{Fc}}{dt} = k_O\left[1 - \theta_{Fc}(t)\left(1 + e^{\frac{-\eta F}{RT}}\right)\right] \tag{2.18}$$

$$i(t) = F\Gamma T\left(k_O\left[1 - \theta_{Fc}(t)\right] - k_R\theta_{Fc}(t)\right) \tag{2.19}$$

Equations 2.20 and 2.21 were developed to calculate the rate constants for oxidation (k_O) and reduction (k_R) of the redox species [1,69,70]. Values of k_O and k_R are calculated using Marcus theory with Levich-Dogonadze electrode modifications in equations 2.20 and 2.21. These equations generate values for k_O and k_R that are used in Equations 2.17 and 2.18. From these equations, CVs of surface-bound redox species can be fit to give E^0, λ, and k_{ET}. The simulated peak potentials are fit to the experimentally determined peak potentials. To limit the number of CV fit parameters, the apparent formal potential $E^{0'}$ from experimental data is used (the average of the Ep_c and Ep_a) and reorganization energy is fixed, if known from experimental data. Finally k_O and k_R are varied (by varying E_p in $\eta = E_p - E^{0'}$) until the fits of the simulated CV E_p values to the experimental E_p values yield a reasonable goodness of fit. However, this approach is not appropriate if there is significant kinetic heterogeneity in the system.

$$k_O(\eta) = \frac{\rho|H_{AB}|^2}{\hbar}\left(\frac{\pi}{kT\lambda}\right)^{1/2}\int_{-\infty}^{\infty}\exp\left[-\frac{(\varepsilon_F - \varepsilon + \eta - \lambda)^2}{4\lambda kT}\right]\times\left(\frac{\exp\left[(\varepsilon - \varepsilon_F)/kT\right]}{1+\exp\left[(\varepsilon - \varepsilon_F)/kT\right]}\right)d\varepsilon \tag{2.20}$$

$$k_R(\eta) = \frac{\rho|H_{AB}|^2}{\hbar}\left(\frac{\pi}{kT\lambda}\right)^{1/2}\int_{-\infty}^{\infty}\exp\left[-\frac{(\varepsilon_F - \varepsilon + \eta + \lambda)^2}{4\lambda kT}\right]\times\left(\frac{1}{1+\exp\left[(\varepsilon - \varepsilon_F)/kT\right]}\right)d\varepsilon \tag{2.21}$$

2.4. Chronoamperometry (CA)

Chronoamperometry is a potential step method [46]. In a single step experiment, an overpotential is applied to the working electrode and the current decay is immediately measured as a function of time. (Figure 2.4) In a double step experiment, the potential is applied symmetrically around the formal potential of the redox center in small increments. For example, if the formal potential of the redox center is 0.0 V, the first and second applied potentials would be +0.05V and −0.05V. The potential limits of the electrolyte and electrode must be taken into account when setting the potential limits. Importantly, the initial potential should be chosen such that all redox centers are in the same oxidation state.

An important aspect is the length of time between potential steps, which must allow for the complete decay of the current. For accurate measurements is critical that the time be long enough for the faradaic current to be separated from the charging current (the initial current spike). High charging currents are generated initially and decay with time and can therefore be temporally separated from the faradaic response as long as the time constant for the charging current is smaller than the rate constant for the faradaic current. Large potential steps can lead to charging currents much larger than the faradaic currents, complicating data analysis. The

appropriate time must be determined experimentally by observing the time it takes for the current to return to baseline levels.

The measured current and applied potential vs. time are required data for rate analysis. The overpotential (η) should be corrected for iR drop as shown in Equation 2.22. R_{SOL} can be determined using electrochemical impedance spectroscopy (Section 2.6).

$$\eta(t) = E(t) - E^{\circ} - i(t)R_{SOL} \tag{2.22}$$

The total current i_T is the sum of the faradaic and the charging current (i_f and i_{ch}, Equation 2.23). The charging current i_{ch} can be determined as Equation 2.24. C_{DL} can be determined using electrochemical impedance spectroscopy (Section 2.6).

$$i_T(t) = i_f(t) + i_{ch}(t) \tag{2.23}$$

$$i_{ch}(t) = C_{DL}\left(\frac{\Delta\eta}{\Delta t}\right) \tag{2.24}$$

The total charge passed, Q_T, can be obtained by integrating the faradaic current over the total time as in Equation 2.25.

$$Q_T = \int i_f(t)\,dt \tag{2.25}$$

The charge remaining at any given time t is derived from Equation 2.26:

$$Q(t) = Q_T - \int_0^t i_f(t)\,dt \tag{2.26}$$

Finally, the rate constant at a given time k_{APP} is calculated as shown in Equation 2.27:

$$k_{APP}(t) = \frac{i_f(t)}{Q(t)} \tag{2.27}$$

The rate as a function of time, $k_{APP}(t)$, may be used rather than rate as a function of overpotential, k(η), due to kinetic heterogeneity. A simple means to determine if a distribution of kinetic sites is apparent is to plot ln(*i*) vs. time. If this plot is curved rather than linear as predicted, then kinetic heterogeneity must be considered [74,75]. Different apparent rates can be observed during the current decay depending on the amount of time passed. Therefore, the current decay may be divided into regimes where different amounts of current (and time) have passed (for example, 80%, 50%, and 20%) [76].

An experimental Tafel plot can be generated by plotting each overpotential against the measured $k_{APP}(t)$. This experimental Tafel curve can be fit to a theorerical curve generated using the Marcus density-of-states model (equations. 2.15, 2.16). The fit parameters of the Marcus density of states model represent k_{ET}, λ and H_{AB} [53]. This method has been used to analyze the electron transfer kinetics for a variety of systems, including ferrocene and Ru $(NH_3)_5$ systems [1,74,76].

2.5. Alternating current voltammetry (ACV)

Alternating current (AC) voltammetry is similar to cyclic voltammetry in that it is a potential sweep method [46]. The equivalent circuit model, the Randles circuit is shown in Figure 2.5, and the waveform of ACV is shown in Figure 2.6a. A starting and ending potential are specified that index the E^0 of the redox species. In addition, a sinusoidally oscillating AC wave is superimposed on the potential waveform. The frequency of the AC can be varied; the magnitude of the AC oscillations is small compared to the overall change in voltage. The resulting alternating current is recorded and the electrochemical response appears as a single peak.

Creager et al. have developed a method of determining the rate of electron transfer for redox species in a SAM [77]. A series of AC voltammograms are collected for a range of AC frequencies, where the ratio of the peak current, i_p, to the background current, i_b, is determined for each frequency. The values of i_p/i_b are plotted vs. the log of the AC frequency. (Figure 2.5b) This plot can be fit to the Randles equivalent circuit model [77]. The only variables needed for determining k_{ET} are the double-layer capacitance (C_{DL}), the charge transfer resistance, (R_{CT}), electrode surface area (A_{SUR}), and surface coverage (Γ). Γ is measured independently using Equation 2.2. The four parameters in the Randles circuit are given by Equations 2.28–2.31.

$$C_{DL} = \left(\frac{C}{A_{SUR}}\right) A_{SUR} \tag{2.28}$$

$$C_{AD} = \frac{F^2 A \Gamma}{4RT} \tag{2.29}$$

$$R_{SOL} = \frac{1}{4\pi r_0 \kappa} \tag{2.30}$$

$$R_{CT} = \frac{2RT}{F^2 A \Gamma k_{ET}} \tag{2.31}$$

A number of articles have appeared that take advantage of this approach to measure k_{ET} in peptides [78–80], short bridges [45,57,81–84], and other novel systems [16,85–89]. There are several advantages to using this method to determine k_{ET}. First, the input variables (C_{DL}, Γ, A_{SUR}, R_{SOL}) are easily obtained from CV or EIS measurements. Second, very low surface coverages can be probed due to the inherent sensitivity of the ACV method. Further, Creager et al. expanded the application of this method to describe systems that have a distribution of rates, or systems with pronounced kinetic heterogeneity (due to variations in the molecular environment caused by SAM or surface defects) [90]. (Figure 2.6c) Variations within rate ranges affect the fit of the simulation to a segment of the i_p/i_b ratio plot. For example, variations of the fit within the 5,000–10,000 s^{-1} range affect the simulated i_p/i_b data at high frequencies while changes within the 1–100 s^{-1} range affect the simulated data at low frequencies. (Figure 2.6d) The disadvantage of this approach is that *only* k_{ET} can be obtained; no information regarding reorganization energy or electronic coupling can be determined.

2.6. Electrochemical impedance spectroscopy (EIS)

The Randles circuit is one of the simplest models for electron transfer for a redox species attached to a monolayer, and will be used to discuss electrochemical impedance spectroscopy (EIS) (Figure 2.5) [46,77,91]. EIS measures the frequency response of a system by measuring impedance, Z. This is done by applying a small AC signal over a range of frequencies at a specified potential. Varying the frequency changes the relative contribution of each of the elements in the Randles circuit to the overall impedance. Measuring impedances over a wide range of frequencies allows the value of each individual element of the Randles circuit to be determined [46,92–94].

R_{SOL} and R_{CT} only contribute to the in-phase, or, real component of impedance (Z_{Re}). A resistor has no effect on the phase, φ, between the voltage and current, so across R_{SOL} and $R_{CT,}$ voltage and current remain in phase (see Figure 2.7). As shown in Figure 2.7, the voltage lags the current by 90° across a capacitor so the voltage and current are out-of-phase across C_{DL} and C_{AD}. As such, C_{DL} and C_{AD} contribute to the out of phase, or, imaginary component of impedance (Z_{Im}) [46].

Using Z_{Re} and Z_{Im}, the general formula for Z can be written in complex notation as in Equation 2.32, where ω is the angular frequency of the AC signal:

$$Z(\omega) = Z_{Re} - jZ_{Im}$$
$$j = \sqrt{-1} \tag{2.32}$$

In general, the magnitude of the impedance (Z) in complex form is given by Equation 2.33.

$$Z = \sqrt{Z_{Re}^2 + Z_{Im}^2} \tag{2.33}$$

The phase of the impedance (φ) in complex form is given by Equation 2.34.

$$\phi = \tan^{-1}\left(\frac{Z_{Im}}{Z_{Re}}\right) \tag{2.34}$$

EIS data is generally plotted in one of two ways, a Bode plot or a Nyquist plot [46,93,94]. In Bode plots, the log of the magnitude of the impedance, log(Z) (from Equation 2.33), and the phase, φ (from Equation 2.34), are plotted separately vs. log(frequency) [46]. An example of a Bode plot is shown in Figure 2.8. In Nyquist, or, complex-plane impedance plots, the ordinate is the imaginary axis, Z_{Im}, and the abscissa is the real axis, Z_{Re}. For data analysis, Nyquist plots are used much more frequently than Bode plots and are discussed in more detail.

In the simplest case, a potential is chosen such that no ET occurs (i.e., away from the E^0 of the redox species attached to the monolayer). In this case, the faradaic component of the Randles circuit is not considered [46,77]. Only R_{SOL} and C_{DL}, connected in series, are considered, and the impedances from each are additive. At high frequencies ($\omega \rightarrow \infty$) there is no time for C_{DL} to charge, and the curve approaches the Z_{Re} axis at R_{SOL}. As the frequency decreases there is more time for C_{DL} to charge, and, at low frequencies ($\omega \rightarrow 0$), the main contribution to the impedance is from C_{DL}. The result is a vertical line on the Nyquist plot, as the impedance contribution from R_{SOL} is unaffected by the frequency. (Figure 2.9)

When a specific potential is chosen where ET occurs (i.e., at or near the E^0 of the redox species attached to the monolayer) the entire Randles circuit is considered. The additional R_{CT} and

C_{AD} contributions to the impedance complicate the derivation of the equation representing the Nyquist plot, and the derivation will not be presented here [95–97]. Only general trends of the resulting Nyquist plot (an example is shown in Figure 2.10) will be discussed.

At high frequencies, the plot is in the shape of an ellipse [77,97]. As $\omega \rightarrow \infty$ there is no time for ET to occur (R_{CT} and C_{AD} become negligible), and there is no time for C_{DL} to charge. Thus, as $\omega \rightarrow \infty$ the high frequency portion of the ellipse approaches the Z_{Re} axis at R_{SOL}. Equation 2.35 shows the center of the ellipse is located on the real axis at the point [97]

$$Ellipse_{center(ZRe)} = R_{SOL} + \frac{R_{CT}}{2\left(1+\frac{C_{DL}}{C_{AD}}\right)^2} \tag{2.35}$$

Equation 2.36 shows the maximum of the ellipse on the Z_{Im} axis is

$$Ellipse_{max(ZIm)} = \frac{R_{CT}}{2\left(1+\frac{C_{DL}}{C_{AD}}\right)} \tag{2.36}$$

As shown in Equation 2.37, the point at which the ellipse would cross the Z_{Re} axis at low frequency ($\omega \rightarrow 0$) is

$$Ellipse_{Low(\omega)(ZRe)} = R_{SOL} + \frac{R_{CT}}{\left(1+\frac{C_{DL}}{C_{AD}}\right)^2} \tag{2.37}$$

However, at low frequencies the Nyquist plot ellipse never approaches the Z_{Re} axis. Instead, the plot becomes a vertical line with an increasingly large Z_{Im} component, as the C_{DL} and C_{AD} contributions dominate the impedance. If the vertical line continues to the Z_{Re} axis, the intercept would be at the same point where the ellipse would cross the Z_{Re} axis as $\omega \rightarrow 0$ (Equation 2.37, Figure 2.10).

In this case, R_{SOL} can be directly measured, but fitting programs are typically used to determine the values of C_{DL}, C_{AD}, and R_{CT}. Fitting programs are typically supplied with the potentiostat software. Once these parameters are known, k_{ET} can be determined using Equation 2.38 [77].

$$k_{ET} = \frac{1}{R_{CT} C_{AD}} \tag{2.38}$$

For example, EIS has been used to determine k_{ET} for electron transfer between ferrocene and a gold electrode through a mixed monolayer of N-(mercaptopentadecyl)ferrocenecarboxamide and 16-mercaptohexadecanol was found to be 9 s^{-1} [77]. In another example, k_{ET} for proton-coupled electron transfer between a 1-aminoanthraquinone derivative and a gold electrode through a monolayer with a 10-carbon alkyl spacer in 0.1 M H_2SO_4 was found to be 7.4 s^{-1} [98]. From this, it was determined that there was a large reorganization energy of 2.7 eV for the 1-aminoanthraquinone ET.

EIS experiments can be quite useful as they allow several different parameters to be measured in one experiment. However, problems may arise due to the non-ideal behavior of the system under study. Nonideal behavior can dramatically alter the values obtained from analysis based

on the Randles circuit model. For accurate data to be obtained these nonidealities must be addressed. One way to treat these nonidealities is through the use of additional circuit elements. A common method is to incorporate a constant phase element (CPE) into the circuit in place of one or more of the elements in the Randles circuit. These types of procedures have been described elsewhere [77,99–101].

2.7. Scanning electrochemical microscopy (SECM)

Scanning electrochemical microscopy is similar to other scanning microscopic techniques such as STM [102,103]. SECM operates by scanning or "rastering" a surface immersed in an electrolyte solution with a metallic tip that acts as an electrode. The tip is typically micrometer-nanometer in size, or is an ultramicroelectrode (UME). SECM allows the UME probe to be positioned very close to the surface of interest, and therefore surface reactivity can be mapped by scanning (Figure 2.11) [102,103]. The observed signal is a faradaic current from electroactive solution species.

SECM experiments can incorporate a redox molecule attached to the monolayer or simply use the monolayer as a barrier to electron transfer between a redox species in solution and the electrode. Measurement of the rate constants is done by plotting current as a function of distance from the tip to the SAM-coated electrode and fitting the data to theoretical curves. One benefit of SECM experiments is that double layer charging current and resistive potential drop are minimized because all measurements are made under steady-state conditions (i.e. the tip is held at a constant electric bias). Another benefit is the ability to perform multiple measurements of rate constants at different points across the electrode surface, allowing the spatial heterogeneity in the SAM to be determined.

SECM often uses mediators, redox species in solution that act as electron shuttles between the SECM tip and the electrode. Electrochemical mediators are typically small redox active species such as methyl viologen, $Ru(NH_3)_6^{3+}$, or $Fe(CN)_6^{3-}$. Mediators have been used in many cases of protein electrochemistry where direct measurement is not possible [11,105].

SECM has been used to measure the rates of electron transfer through a monolayer using mediators in solution (Figure 2.10) [104,105]. With no redox species attached to the monolayer, SECM allows the measurement of k_{ET} between a solution mediator species to the electrode through the monolayer. However, when a redox species is attached to the monolayer, SECM allows the measurement of the rate of electron tunneling from the attached redox species through the monolayer to the electrode. Further, the bimolecular rate of electron transfer between the attached redox species and the mediator in solution can be determined.

In one of the first reports of this technique, electron transfer rate constants were measured from monolayer-bound ferrocenium to both the electrode (through the monolayer) and to a [Ru $(NH_3)_6$2+ mediator in solution [104]. The standard rate constant for ET between the electrode and $[FcCONH(CH_2)_{15}SH]^+$ with hexadecanethiol as the diluent was 7.0 s^{-1}. When $[FcCONH(CH_2)_7SH]^+$ was used with nonanethiol as the diluent, the standard ET rate constant was 1.2×10^5 s^{-1}. As expected for a tunneling mechanism, the k_{ET} decreased exponentially as the number of methylene units increased [30,38,41,106]. The tunneling decay constant for this process was found to be 1.0 per methylene unit, consistent with other values reported for this type of monolayer. The bimolecular electron transfer rate between the mediator, $[Ru(NH_3)_6]^{3+}$, and the ferrocene bound to the monolayer was found to be greater than 4.5×10^{10} $cm^3mol^{-1}s^{-1}$. In addition, the k_{ET} for electron transfer from the $[Ru(NH_3)_6]^{2+}$ mediator through a nonelectroactive monolayer was measured. In this case, the mediator was regenerated by electron tunneling through the monolayer.

SECM has been used by Holt et al. to measure the ET kinetics of cytochrome c attached to 11-mercaptoundecanoic acid monolayers using $[Fe(CN)_6]^{3-}$ as the mediator [105]. Notably, slower tunneling rates were observed for cytochrome c covalently attached to the SAM via amide linkages formed between protein lysines and the acids of the monolayer, as opposed to proteins that were electrostatically bound. When cyt c was covalently attached to the SAM, the k_{ET} was 9 s^{-1}. However, if the protein was electrostatically bound, the k_{ET} was 15 s^{-1}. An even faster tunneling rate of 65 s^{-1} was observed when a mixed monolayer of 1:1 decanethiol and 11-mercaptoundecanoic acid was used. The reason for faster tunneling is presumed to be the increased mobility of cytochrome c when electrostatically bound to surface of the monolayer, allowing for a more efficient orientation of the protein with respect to the electrode, making ET more favorable. The bimolecular ET rate between cytochrome c and the mediator was measured to be approximately 2.2×10^8 $cm^3mol^{-1}s^{-1}$, consistent with literature values for this type of process [105].

2.8 Indirect Laser Induced Temperature jump method (ILIT)

CV and CA are generally considered to be limited to measuring rates that are < 10^4 s^{-1}. An indirect laser-induced temperature jump (ILIT) technique was developed to measure rates for short bridge lengths [56]. A short (ns) laser pulse impinges onto the backside of a thin gold film electrode. The absorbed laser energy is rapidly (<1 ps) diffused as heat throughout the gold causing a small change (2–4 °C) in the temperature of the on the other side of the gold film at the SAM/electrolyte solution interface. The interfacial equilibrium is altered and the open circuit potential of the electrode changes. This method requires highly specialized equipment and is not readily available.

2.9 Summary of Electrochemical Methods

To summarize this section, four common electrochemical techniques have been described that allow the quantitative determination of electron transfer parameters such as λ, ΔG, H_{AB}, and k_{ET}. It is important to recognize the advantages and limitations of each of these techniques before performing electrochemical experiments to measure any of these parameters.

Cyclic voltammetry is the most common technique, largely because the faradaic current is readily separated from the charging current. CV allows measurement of the electron transfer parameters, λ, ΔG, H_{AB}, and k_{ET}. The Laviron method is relatively straightforward. However, it is limited, and often the Marcus density of states theory must be applied. Chronoamperometry is a facile technique that has been employed to determine λ, H_{AB}, and k_{ET}. In CA measurements, the faradaic current is temporally separated from the charging current. As with CV data, Tafel plots are fit using Marcus theory. An important aspect of chronoamperometry is that it is very sensitive to kinetic heterogeneity. Finally, the solution resistance should always be considered in CV and CA measurements, as it can lead to anomalously low reorganization energies.

Alternating current voltammetry is the ideal method for identifying the subpopulations contributing to a distribution of rates. The main disadvantage of this method is that only k_{ET} can be obtained. λ, ΔG, and H_{AB} must be determined using other methods. Electrochemical impedance spectroscopy is used to determine k_{ET} as well as R_{SOL} and C_{DL}. However, as with the ACV method, λ, ΔG, and H_{AB} cannot be determined. Experiments are fairly simple to perform but because the phase must be considered, data analysis is complicated and can be difficult to interpret. Another disadvantage of EIS is that nonidealities can dramatically alter the values of the ET parameters obtained. Finally, SECM allows k_{ET} to be determined for both adsorbed and solution species in single experiments. The small size of the SECM tip allows information about SAM surface reactivity to be mapped. Another advantage of SECM is that

C_{DL} and resistive potential drop are minimized since measurements are made under steady-state conditions.

3. Redox species used for electrochemical determination of k_{ET} in monolayers

Metal complexes that are selected for electrochemical SAM studies exhibit reversible electrochemical reactions in which both oxidation states are stable. Often, these complexes have a high coordination number and small ligands that are substitutionally inert (Figure 3.1). These redox centers possess negligible inner-sphere λ values. Finally, an essential parameter is that redox potential must be energetically accessible, (i.e., it must be within the potential window that is determined by (1) the SAM stability and (2) the electrolyte and solvent.)

3.1. Ferrocene

Ferrocene was discovered in 1951 by Pauson and Kealy who were attempting to synthesize fulvalene [107]. This complex is the first widely known organometallic compound that defied definition until 1952 when the structure was determined [108,109]. Two cyclopentadienyl (Cp) anions coordinate η^5 to one Fe(II) cation resulting in an overall neutral complex. (Figure 3.1) The complex is small, measuring approximately 4.1 × 3.3 Å. The ferrocenium ion is only slightly different, measuring 4.1 × 3.5 Å, indicating that the inner-sphere reorganization energy is low. The carbon-carbon bond distances are 1.40 Å within the cyclopentadienyl rings, and the bond distances between the iron and the carbon atoms are 2.04 Å. This “sandwich” structure has been duplicated using a variety of transition metals including ruthenium, cobalt and nickel but these complexes have not been used in electrochemical SAM studies.

The most stable, electrochemically addressable oxidation states of iron in ferrocene are Fe(II) and Fe(III) [110]. The Fe(II) state is orange whereas Fe(III) (the ferrocenium ion) has a characteristic blue color. The electronic properties of ferrocene are acutely sensitive to functional groups attached to the Cp ring (Figure 3.1) [111–114].

Ferrocene is highly soluble in organic solvents, insoluble in aqueous media and undergoes reactions characteristic of aromatic compounds, enabling the preparation of a wide variety of substituted derivatives [114–124]. A wide variety of symmetric and asymmetric derivatives are commercially available, such as ferrocene carboxylic acid, ferrocene dicarboxylic acid, and dimethylaminomethyl ferrocene. A common synthetic approach is the Friedel-Crafts reaction. Ferrocene reacts readily with butyl lithium to give 1,1'-dilithioferrocene, which is a versatile synthetic precursor to symmetric compounds [125,126]. With the emergence of click chemistry, azide and alkyne derivatives have been utilized [127,128]. The covalent incorporation of ferrocene into peptides [129–134], peptide nucleic acids [135–137], and DNA [6,138,139] has been accomplished due to the ease of functionalization. A selection of orthogonally functionalized asymmetric ferrocenes has recently been reported [140].

3.2. Ruthenium ammine complexes

The ruthenium center in ruthenium(III) hexaammine trichloride is octahedral and symmetric with six NH_3 ligands (Figure 3.1). The Ru-N bonds are 2.104 Å, which changes only very slightly to 2.144 Å upon reduction to Ru(II) [141]. Unlike the anionic Cp ligands of ferrocene, however, the neutral ammine ligands do not neutralize the charge. This pale yellow complex is highly soluble in aqueous media, and in 1965 the reduction of $[Ru(NH_3)_6]^{3+}$ was shown to result in the stable $[Ru(NH_3)_6]^{2+}$ species [142]. The solubility and stability of this complex has led to its wide use as an electrochemical standard.

Ruthenium ammine complexes have a rich history in inorganic chemistry [143]. The $[Ru(NH_3)_5Cl]^{2+}$ intermediate is synthetically versatile and a wide range of ligands have been explored. One of the most well known examples is the first complex of dinitrogen, $[Ru(NH_3)_5N_2]^{2+}$ reported by Allen and Senoff in 1965 [144,145]. Taube won the Nobel Prize in 1983 for his studies of electron transfer using the mixed valence pyrazine-bridged dinuclear complex $[Ru(NH_3)_5pzRu(NH_3)_5]^{5+}$ otherwise known as the Creutz-Taube complex [146].

Ruthenium(II) pentaammine complexes are synthesized by the reduction of $[Ru(NH_3)_5Cl]Cl_2$ to give $[Ru(NH_3)_5(H_2O)]^{2+}$ that has a labile inner sphere water ligand (Figure 3.2). The water ligand can be replaced by a wide variety of N donor ligands (L) such as nitriles and N-heterocycles and the redox potential of these complexes is highly sensitive to functionalization of these N-heterocycle rings [147,148]. The relevant parameters for calculating λ_i have been reported for $[Ru(NH_3)_5(py)]^{2+/3+}$ [149]. The Ru(II)-N_{py} bond distance in $[Ru(NH_3)_5(py)]^{2+}$ changes only from 2.058 to 2.077 Å upon oxidation to Ru(III), indicating a small λ_i. A wide variety of stable ruthenium (II) tetraammine complexes $[Ru(NH_3)_4L_2]^{2+}$ have been isolated and characterized (Figure 3.1) [150,151].

3.3. Osmium

Osmium has rich inorganic chemistry that closely parallels that of ruthenium [152,153]. Os (II), Os(III), and Os(IV) complexes of N-heterocycles such as bipyridine and phenanthroline are the most widely used for electrochemical studies due to the synthetic accessibility from K_2OsCl_6. The stability, redox potential accessibility, and photochemical properties have been widely reported [154–157]. Examples of osmium complexes most commonly used in SAM studies are shown in Figure 3.3.

3.4. Buckminsterfullerene (C_{60})

C_{60} possesses eight accessible oxidation states [158–161] and has small inner-sphere reorganization energy (~0.06 eV) [162,163]. This low λ_i is most often cited as the attribute of C_{60} that leads to efficient photoinduction of a long-lived charge-separated state. C_{60} has been incorporated into numerous porphyrin constructs as models for photosynthesis [164–172].

C_{60} has been functionalized and covalently immobilized on SAMs [173–178]. Although Au and Hg have been used as the SAM substrate electrode, these molecules are typically immobilized on ITO. This transparent conducting material allows for photoinduced processes to be examined by measuring photovoltage or photocurrent. For applications in artificial photosynthesis, porphyrin-fullerene dyads and triads have been covalently incorporated onto SAMs [164–172].

C_{60} has been noncovalently attached to SAMs [158,179]. In one instance, a crown ether-functionalized C_{60} was incorporated into a SAM by the interactions between the crown ether and ammonium groups on a modified electrode [158]. The resorcinarene molecule has been used as a recognition element to incorporate unsubstituted C_{60} molecules to SAMs [179]. The majority of the electron transfer studies involving C_{60} have used spectroscopic techniques [15,164,180–182]. Electrochemical methods have not been reported to study ET kinetics for C_{60} for comparison with ferrocene or other metal complexes.

3.5. Redox species in solution

To measure ET parameters using electrochemistry, it is often necessary to use a large η (Equation 2.4, up to 1 V or greater). This measurement requires slow rates of ET in order to avoid mass transfer limitations [41,46,53]. The simplest way to achieve these slow rates for redox species in solution is to passivate the electrode with a SAM. (Figure 3.5) The SAM acts as a barrier to electron transfer, slowing the rate between the redox species in solution and the

electrode. The thickness of the monolayer can be changed to tune the rate of ET to ranges applicable for the desired ET studies.

In work by Miller et al., different monolayer thicknesses were prepared by using hydroxyalkane thiols of varying chain lengths (from 2 to 16 methylene units) on a gold electrode [38]. CVs were obtained with $[Fe(CN)_6]^{3-}$ and $[Fe(H_2O)_6]^{3+}$ in solution. Capacitance measurements confirmed the monolayers were free from pinhole defects. As expected for a tunneling mechanism, a logarithmic relationship was found between k_{APP} and the thickness of the monolayer for both complexes. Tafel plots showed curvature at large overpotentials in agreement with predictions made from Marcus theory [24,38,53,61,183]. The tunneling constant (β, Equation 6.1) for this ET process was measured to be 0.9 per methylene unit. In this experiment it was shown that SAMs act as an effective barrier to ET from a redox species in solution to the electrode, allowing large overpotentials to be used without mass transfer limitations.

3.6. Metal clusters

Metal clusters provide a versatile platform for monolayer modification that would otherwise be difficult to achieve using more conventional complexes. Metal clusters have multiple coordination sites that allow formation of multilayers on the surface of SAMs [184–186]. Layered structures have been shown to have enhanced properties in a variety of applications such as molecular electronics and sensors [184]. Trinuclear ruthenium clusters of the form $[Ru_3(\mu_3\text{-}O)(\mu\text{-}CH_3COO)_6(bpy)_2(CO)]$ (bpy = 4,4'-bipyridine) are one example of clusters that can be used for controlled layer-by-layer deposition of electroactive multilayer formation [184–186]. (Figure 3.6) These complexes have two Ru(III) centers and one Ru(II) center and a CO is bound to the Ru(II) center of the cluster. Attachment to the monolayer has been accomplished via peptide coupling between a terminal acid on the monolayer and the amine of 4-aminomethylpyridine (4-AMP) of $[Ru_3(\mu_3\text{-}O)(\mu\text{-}CH_3COO)_6(4\text{-}AMP)(4\text{-}MePy)(CO)]$. Upon electrochemical oxidation to Ru(III), the CO dissociates forming an aquo species. This results in a free reactive site for attachment of the next layer. The next layer is formed by the addition of a $[Ru_3(\mu_3\text{-}O)(\mu\text{-}CH_3COO)_6(bpy)_2(CO)]$ molecule that forms a dative bond from one of the bpy nitrogens to the ruthenium of the cluster and repeating this process forms the multilayer [184,185]. It was observed that $E_{1/2}$ for the $Ru^{III/II}$ couple shifts +45 mV for loosely packed multilayers, but up to +90 mV for more compact, densely packed multilayers. This result has been attributed to the decreased access of anions into the multilayer in the latter [185]. A similar approach has been used to construct a layer of dinuclear $[Ru_2(\mu\text{-}O)(\mu\text{-}CH_3COO)_2(2,2'\text{-}bpy)_2(4,4'\text{-}bpy)_2](PF_6)_2$ on top of a SAM of $[Ru_3(\mu_3\text{-}O)(\mu\text{-}CH_3COO)_6(4\text{-}AMP)(4\text{-}MePy)(CO)]$ (Figure 3.7) [186].

$[Ni_3(\mu_3\text{-}I)(\mu\text{-}CNR)(\mu_2\text{-}dppm)_3]^+$ has been studied using SAM electrochemistry (dppm is 1,1-bis(diphenylphosphino)methane and the R group is phenylthiolate) (Figure 3.8) [187]. This nickel cluster has been shown to form monolayers on gold having a coverage of 3.74×10^{-10} mol/cm^2 signifying a single, well-defined monolayer. It has been shown that these electroactive SAMs show rectification behavior. Specifically, electron transfer from the electrode to a redox acceptor in solution is permitted only at potentials negative of E^0 of the trinuclear nickel cluster. Thus, the nickel cluster must be reduced from Ni_3^+ to Ni_3^0 before reduction of a solution species can occur. Therefore, the Ni_3^+ species acts as a barrier to electron transfer to an acceptor in solution at potentials more positive than E^0 of the trinuclear nickel cluster, and obviously, more negative than E^0 of the acceptor in solution. No effect was seen on the electron transfer from the species in solution (donor) to the electrode (the anodic peak in a CV is unaffected).

In addition to trinuclear ruthenium and nickel clusters, gold nanoparticle clusters attached to SAMs have been studied (Figure 3.9) [17,188]. These gold clusters have been used to improve

electronic coupling between metalloproteins and electrodes [17]. Recently a construct incorporating gold clusters was used to form an electrical contact between Cu^{II} of the redox metalloenzyme galactose oxidase [17]. A monolayer of biphenyl dithiols was formed on the electrode and this SAM was incubated in a solution of thioctic acid-capped gold clusters to assemble the gold clusters on the SAM.

The galactose oxidase is immobilized on the cluster-SAM assembly by substitution of a labile water of the Cu(II) site of the enzyme with the terminal acid of thioctic acid. Fast electron transfer occurs between a stable tyrosyl radical of the galactose oxidase and the electrode, mediated by the gold cluster. Slow electron transfer was observed between the copper of galactose oxidase and the electrode. The immobilized galactose oxidase maintains its ability to catalytically reduce oxygen.

4. Outer-sphere effects on electron transfer kinetics

Noncovalent interactions such as ion pairing, van der Waals forces, hydrogen bonds, and solvent polarizability affect γ_o and can have a significant impact on k_{ET} [24]. γ_o is difficult to measure and the error is typically on the order of ±0.1 eV, and few reports have focused on determining this parameter [1,76,157,189–195]. Values of γ_o obtained from independent variable temperature and variable driving force experiments do not always agree. Ion-pairing effects [154,191], double-layer effects [196], uncompensated solution resistance effects [74], and the presence of a heterogeneous distribution of rate constants [75] are all possible contributors to the discrepancies.

The reorganization energy and preexponential factor can be obtained from an Arrhenius analysis [45]. k_{ET} is determined for a range of temperatures and $\ln(k_{ET})$ is plotted vs. 1/T. The activation energy E_A is calculated as k_B times the slope of the Arrhenius plot and the apparent reorganization energy is calculated using Equation 4.1. The Arrhenius preexponential factor A and activation energy E_A are given by Equation 4.2.

$$E_A = \frac{\lambda}{4} \tag{4.1}$$

$$A = 2\pi^{3/2} H_{AB}{}^2 \rho / h \tag{4.2}$$

4.1. Solvent and counterion effects

SAMs of $[Os(bpy)_2Cl(pNp)]^-$ (N = 2, 1,2-bis(4-pyridyl)ethane; N = 3, 4,4'-trimethylenedipyridine) were studied using CA [154]. The influence of solvent on the kinetics and thermodynamics of electron transfer was explored using acetonitrile, acetone, dimethylformamide, dichloroethane, tetrahydrofuran, and chloroform. For the p2p monolayers, the k_{ET} ranges from 7.4×10^3 s^{-1} ($CHCl_3$) to 1.1×10^5 s^{-1} (MeCN). For the same solvents, the p3p monolayer k_{ET} values are 1.6×10^3 and 1.8×10^4 s^{-1}, respectively. For both these monolayers, a linear correlation was observed between the rate and the longitudinal relaxation rate of the solvent, suggesting that electron transfer is strongly influenced by solvent reorganization dynamics.

Although γ is routinely determined as part of fitting Tafel plots, only one study has been undertaken to specifically probe changes in γ_o [74]. SAMs of $[Ru(NH_3)_5pyCH_2NHCO(CH_2)_nSH]^{2+}$ (n=10 or 15) diluted with $HO_2C(CH_2)_nSH$ alkane thiols were studied using 10 solvents: acetonitrile, acetone, methanol, ethanol, n-propanol, n-butanol, N,N-

dimethylformamide, dimethylsulfoxide, propylene carbonate and tetrahydrofuran. Values of γ were determined by generating a Tafel plot from CA data and fitting using the Marcus density of states model. The measured γ for water (0.8 – 0.9 eV) is consistent with the value of 0.9–1.0 eV predicted by Marcus' equation for γ (Equation 2.10). The anodic γ is greater than or equal to the cathodic γ in nonaqueous solvents which the authors attribute to strong ion-pairing.

Using Equation 2.10, γ_o varies from 0.92–0.75 eV. It is proposed that there may be a high local water concentration at the surface of the monolayer that solvates the redox centers [74]. No effort was made to dry the organic solvents and it seems likely that this scenario would lead to values similar to those measured for aqueous conditions. The nonpolar solvents propanol, butanol, and THF show low γ_o values as predicted by Equation 2.10. The authors recognize the difficulty in determining γ accurately and do not indicate a breakdown of the assumptions behind Eq. 2.10 and suggest that it may be used for estimating γ_o of redox centers on a monolayer.

The effect of the counterion (BF_4^-, ClO_4^-, and PF_6^-) on k_{ET} of a ferrocenyl peptide SAM was examined [191]. Twelve noncyclic and cyclic ferrocene-containing peptides were immobilized on gold microelectrodes via a cystamine disulfide bond. The k_{ET} and γ were determined using variable temperature CV. The k_{ET} ranged from 4.4–12 $\times 10^3$ s^{-1}. The highest reorganization energy was observed for the BF_4^- counterion, which has the weakest association with the ferrocenium cation. The more rigid cyclic peptides were found to have smaller reorganization energies ranging from 0.3 to 0.5 eV compared to the more flexible noncyclic ferrocenyl peptides (0.5–1.0 eV).

4.2. Proton-coupled electron transfer (PCET)

Besides being of fundamental scientific interest, the details of how protons and electrons are transferred remain an area of intense theoretical and experimental interest [67,197,198]. Proton-coupled electron transfer (PCET) has been implicated in numerous biological processes, including enzyme reactions, photosynthesis, and respiration [199–203]. Technological applications include alternative energy sources (fuel and solar cells), sensors, and molecular electronics. Further, organic radicals are of interest in nanostructured magnetic materials. The study of surface-bound radicals is directed towards the development of organic ferromagnets that show long range magnetic order in the crystalline phase. TEMPO and galvinoxyl are highly stable radicals that persist at room temperature and have been studied using SAMs [190,204–206]. A number of excellent reviews cover the area of PCET in greater detail [66,67]. In this section we highlight examples for comparison of k_{ET} with the alkane thiol electron transfer systems described in this review.

Possible mechanisms of PCET are stepwise and concerted mechanisms for proton and electron transfer. In the stepwise mechanism, ET and PT occur separately [67]. The pH dependence of ET can be studied to elucidate this mechanism. In the concerted mechanism, ET and PT occur in the same rate-determining step. This mechanism is most often investigated by taking advantage of the kinetic isotope effect [207].

For PCET studies, it is desirable to investigate a system that electrochemically accessible over the full range of pH-dependent behavior. Reports from Takeuchi et al. [208,209]. regarding the promising behavior of [Os(II/III)(terpy)(bpy)(H_2O)] led Finklea and coworkers to develop [Os(II)$(bpy)_2$(4-AMP)(H_2O)], which has a suitable potential and pH dependence PCET studies [205]. Os(II)$(bpy)_2$(H_2O)(4-AMP) was attached to a HO_2C-terminated alkane thiol monolayer via peptide coupling. (Figure 5.4) Thermodynamically, the attached Os(II) aquo species exhibits the expected behavior for a 1 electron, 1 proton system. The formal potential varies with pH, reaching constant values at pH < 2 (0.3 V vs. SCE) and pH > 9 (−0.11 V vs. SCE). These potentials and pK_a values are in agreement with those found for the solution species

[208,209]. Kinetically, however, this system deviates considerably from predictions of the stepwise model. At low and high pH values, the cathodic λ is substantially less than the anodic λ (0.6 and 1.4 eV respectively). The plot of log(k_{ET}) vs. pH does not have the shape predicted by the stepwise model [205]. Finally, α is consistently ~0.5 at all pH values. This behavior is attributed to a concerted PCET mechanism.

For comparison $Os(bpy)_2Cl(4\text{-}AMP)$ was attached to a HO_2C-terminated alkane thiol monolayer to investigate the effects of the HO_2C SAM functionality. The formal potential did not vary with pH, indicating that any double layer effects are negligible. λ was found to be slightly different for the anodic (0.64 eV) and cathodic (0.57 eV) peaks and the average k_{ET} was found to be 11±1 s^{-1}.

The Os(II) aquo system was studied further by Finklea et al. using D_2O to investigate any kinetic isotope effect on the PT/ET mechanism [192]. Asymmetric Tafel plots for this system showed different λ for the Os(II) and Os(III) species. The λ for Os(III) had no pH dependence (0.6–0.7 eV over the pH range). On the other hand, λ for Os(II) showed a pH dependence (0.70–1.0 eV over the pH range with smaller λ found close to the pK_a of the complex). The pH dependence of λ accounts for most of the dependence of electron transfer rate on pH. The authors concluded that a concerted mechanism was appropriate to describe PCET for this system.

In recent reports by Costentin et al, the solution PCET behavior of $[Os(bpy)_2(py)(H_2O)]^{2+/3+}$ was studied [210,211]. In this work, it was demonstrated that the rate constants of this species follow the stepwise model. These results are in contrast to Finklea's analogous SAM-bound osmium complex, suggesting that the carboxylic acids at the SAM-solution interface are the proton source and sink for the concerted proton-coupled electron transfer observed for Finklea's complex (shown in Figure 5.6).

One of the most widely recognized redox-active organic molecules is hydroquinone that undergoes a 2 electron oxidation and corresponding loss of 2 protons. The pH dependence of k_{ET} of hydroquinone attached to the electrode via a saturated alkane (**HQ-C11**) or conjugated OPV (**HQ-OPV**) bridge has been examined (pH 8 – 12.6) (Figure 4.1) [16,212]. These hydroquinone SAMs were diluted with octane-1-thiol. The electrochemistry for both **HQ-C11** and **HQ-OPV** is near-ideal and reversible at basic pH values. The value of α is 0.48 for **HQ-OPV** at pH 12.6 and 0.55 for **HQ-C11** [16,212]. Laviron's equation was used to evaluate k_{ET}. For the protonated form of hydroquinone, the nature of the bridge has a significant effect on k_{ET}, 0.1 $^{-1}$ for **HQ-C11** and 77s^{-1} for **HQ-OPV**. For the deprotonated form of hydroquinone, the k_{ET} is less sensitive to the nature of the bridge, 120 s^{-1} for **HQ-C11** and 268 $^{-1}$ for **HQ-OPV**.

2-Methyl-1,4-naphthoquinone has been derivatized with alkane thiols consisting of 5–12 atoms in the bridge [213]. (Figure 4.2) The Laviron method was used to evaluate the k_{APP} and in acidic conditions the $-\ln(k_{APP})$ for the 12-atom bridge was 10.4. The β of 0.89 ± 0.16 per bridge atom agrees with previously reported values for pentaammine(pyridine) ruthenium-terminated (1.06 ± 0.04) SAMs [45].

Galvinol was modified with an alkane thiol and attached to a SAM on a gold electrode for electrochemical studies of PCET [204,205]. (Figure 4.3) The predicted asymmetry in the CVs was observed for pH < 11. For the deprotonated galvinol/galvinoxyl radical redox couple, the k_{ET} at pH 10–13 was determined to be 4.5×10^3 s^{-1}. The inner- and outer-sphere λs for galvinol have not been reported, but the similarity of the galvinol-SAM k_{ET} to that for a ferrocene-labeled SAM with the same alkane bridge suggests the total λ may be comparable to that of ferrocene (~0.8 eV).

Galvinoxyl layers on Au(111) have been studied by STM, EPR, and CV [206]. In the STM, two phases are observed with different molecular densities. EPR results confirm that the radical character of galvinoxyl is preserved. A one-electron oxidation with corresponding loss of a proton was determined from oxidation potential vs. pH curves and is similar to the behavior of the free radical in solution. This indicates there is no dramatic change of the electronic properties of the radical upon adsorption [206].

4-Amino-TEMPO (Figure 4.3) was coupled to a carboxylic acid-terminated SAMs of $HO_2C(CH_2)_{10}SH$ on gold electrodes and analyzed using CV [190] and analysis of the CVs gave a k_{ET} of 1.2 s^{-1}. The reorganization energies of TEMPO· and $TEMPO^+$ were found to be 1.5 and 1.3 eV respectively. These values are the first experimental measurements of λ of TEMPO in aqueous solution.

4.3.Metalloproteins

Electron transfer rates in proteins have been extensively studied by modifying the protein with transition metal chromophores and using photochemical initiation, direct photoinduced ET, and flash-quench methods [30]. Protein-bound Ru(II)bpy species are irradiated and the excited state is quenched by a reagent in solution. The resulting species undergoes ET with the protein active site via thermal electron transfer. Marcus theory describes these reactions quite well and has shown that the protein shell lowers the λ barrier to electron transfer by excluding solvent [29,30,214].

4.3.1.Cytochrome c—Cytochrome c is a small (12 kDa) electron transfer protein containing a heme redox center that has been the subject of extensive study [27,31,188,193,194,215–230]. Modification of electrodes for the immobilization of cytochrome c was first reported by Taniguchi in 1982 [231]. The first systematic study of ET using cyt c on SAM-modified electrodes was carried out by Bowden and k_{ET} was found to be 0.4 s^{-1} for $HO_2(CH_2)_{15}SH$ on gold [232]. The decay constant was 1.0 $Å^{-1}$ and λ was found to be 0.35 eV [232]. Differences in horse heart cyt c and yeast cyt c were probed using mixed monolayers of $HO(CH_2)_nSH$/$HO_2C(CH_2)_nSH$ [233]. It was found that the mixed monolayers increase the rate for both while pure HO_2C-terminated monolayers gave most efficient ET for the horse heart cyt c. This finding correlates with what is known about the native biological ET partners of these metalloproteins. For horse heart cyt c, the ET pathway contains ionic interactions where as for yeast the pathway is nonionic.

Cyt c was adsorbed on Ag electrodes and investigated using electrochemistry and SERRS in 1980 [229]. More recently, the protein was electrostatically bound to Ag using a carboxylic acid-terminated ($HO_2C(CH_2)_nSH$) SAM [222,234–236]. Structural changes were observed at short lengths ($n < 6$) and the k_{ET} was determined to be 0.073 s^{-1} for n = 16 and 43 s^{-1} for n = 11. For $n \leq 6$, k_{ET} was 134 s^{-1}. A kinetic isotope effect was observed, indicating a rearrangement of hydrogen bonds and that proton transfer (PT) is rate limiting for these cases. PT dynamics slow with increasing bridge length.

This result indicates that the high electric field (experienced when the bridge lengths are short) raises the energy barrier. In a related study, λ was determined to be 0.26 eV, which is low compared with 0.6 eV found in solution, and is attributed to poor solvent access to the protein redox center once it is bound to the SAM [235]. From this work, it appears that a short SAM results in conformational gating as the high electric field raises the activation barrier for protein structure reorganization [222,234,235].

SERRS was employed to study cyt c on SAMs on Ag and Au using a pyridine-terminated ($pyCH_2NHCO(CH_2)_nSH$) SAM that provides a binding ligand for the cyt c heme [236]. A potential-dependent coordination equilibrium was observed. The reduced form is a five-

coordinate high-spin state and the oxidized form is a six-coordinate low-spin state. The k_{ET} is 760 s^{-1} that is in good agreement with 780 ± 40 s^{-1} measured previously [221,237].

In another study using the same pyridine-terminated SAMs, λ was found to be 0.5±0.1 eV [238]. As expected for weak coupling, the rate was nonadiabatic for long bridge lengths ($n \geq 12$). For short bridge lengths, the data are best fit by a model that includes friction between the solvent and the protein that slows the polarization relaxation [238]. This finding is in contrast to HO_2C-terminated SAMs that are conformationally gated due to the high electric field at short bridge lengths [222,234,235].

Variations appear in the reported E^0 (ranging from 0.0 to −0.06 V vs. SCE) and k_{ET} (20–100 s^{-1}) of cyt c on MUA [222,223,232–234,239]. The source of these variations was addressed by Millo et al. [240]. The authors propose that the source of the error lies in the requirement of different surfaces for different types of measurements. SERRs requires a rough Ag surface whereas SEIRA uses a rough Au surface and CV uses smooth Au. Cyt c was electrostatically bound to SAMs adsorbed on all four types of surface (Au-rough, smooth; Ag-rough, smooth) and studied by CV. It was determined that E^0 (−0.068V vs. SCE) is not dependent on the metal or the morphology. However the k_{ET} is dependent on the metal (16 s^{-1} on Ag and 33 s^{-1} on Au), for reasons outlined in the Electrode Materials section.

4.3.2. Azurin—Azurin is found in the electron transport chains of bacteria and has been thoroughly characterized [13,29,32,203,[214],[218],224,230,241–248]. The active site consists of a mononuclear copper ion that lies in the plane of three ligands (two His and a Cys) with one axial ligand (Met) and a weak interaction with a peptide carbonyl oxygen. The coordination geometry is highly restricted by the protein shell and changes little between oxidation states, resulting in a λ of 0.7–1.0 eV [30].

A number of studies have adsorbed azurin on gold electrodes, modified with long ($n_{CH2} = 10$) and short (n_{CH2} 6) alkane thiol SAMs for electrochemical studies [249,250]. Ideal behavior was observed resulting in k_{ET}(long) = 470 ± 50 s^{-1} and k_{ET}(short) = 3200 ± 300 s^{-1} [249]. In another study, hydrophobic interactions between the hydrophobic area around the copper center in azurin and methyl headgroups of alkane thiol are proposed to stabilize the adsorption of the protein on the SAM [250]. Azurin is most likely oriented with the redox center facing the electrode surface. The length of the alkane thiol was varied and an exponential distance decay with β = 1.03 ±0.02 per CH_2 unit was observed for alkane thiols of lengths >9 CH_2 units. Apparent rate constants (k_{APP}) were determined using Laviron's method and EIS. The results for these two methods are in close agreement. (70 s^{-1}, n=11; 0.1 s^{-1}, n=17) However, λ was reported to be 0.3 eV, significantly lower than small molecule redox species such as ferrocene on a SAM, and was ascribed to the hydrophobic nature of the environment imposed by the SAM.

Squarewave voltammetry has been used to examine the electrochemical properties of azurin adsorbed onto alkane thiol SAMs on gold [251]. No kinetic isotope effect was observed and the pH showed no effect on k_{ET}. The viscosity of the solution was increased and found to have no effect on k_{ET}. The data indicate that the electron-transfer reaction is gated by a preceding process and fit well for k_{ET} of 1×10^3 s^{-1} and λ = 0.7 eV.

A mixed monolayer using a 1:1 mixture of $H_3C(CH_2)_nSH$ and $HO(CH_2)_nSH$ (n = 11, 15) on gold was used to study azurin [220]. Site-directed mutagenesis was used to identify amino acid residues crucial to electron transfer. Only wild-type azurin, and mutants containing Trp48, exhibited voltammetric responses. Using Laviron's method, k_{ET} was determined to be 63 s^{-1} with a long alkane thiol ($n_{CH2} = 11$) SAM. A linear relationship between log(k_{ET}) and chain length was found for longer chains ($n_{CH2} > 6$), with a slope of 1.0/CH_2. It is proposed that

electronic coupling between the SAM headgroup (H_3C- and/or HO-) and specific amino acid residues is important to electron transfer.

In a related study, it was found that the ionic strength does not have an effect on the k_{ET} of azurin adsorbed onto HO/CH_3 terminated SAMs, indicating that hydrophobic interactions are more important than ionic interactions [252]. The k_{ET} plateaus at 1×10^3 s^{-1} ($n_{CH2} < 9$) due to protein-SAM interfacial dynamics.

Azurin electron transfer was compared using SAMs of a stilbene-based thiol (a conjugated bridge) and an alkane thiol (saturated bridge) [253]. The stilbene-based wire gave a k_{ET} of 1600 s^{-1} (15.8Å) while the aliphatic comparisons were 481 s^{-1}(14.5Å) and 600 s^{-1} (17Å). Interestingly, the conjugated bridge does not increase k_{ET} by orders of magnitude as observed for ferrocene-based studies [44,45,57,254].

The effect of urea on the azurin protein structure was probed electrochemically [255]. Urea is known to denature proteins and it was presumed that if the protein denatured while adsorbed to the SAM, changes in the reorganization energy would be observed. Surprisingly, λ is not sensitive to high concentrations of urea indicating the active site is not perturbed. Longer alkane chain lengths yielded larger λ values indicating that longer chain lengths result in larger structural fluctuations. The shorter chain lengths correspond to higher electric field strengths which may inhibit these fluctuations.

Azurin was recently studied using nanoparticle films on electrodes [256]. The nanoparticle film was formed by linking gold nanoparticles using alkane dithiols. Azurin was adsorbed onto the resulting surface and studied electrochemically. The k_{ET} for the nanoparticle film was very fast (where $\beta \sim 0.01/CH_2$) indicating a hopping rather than a tunneling mechanism. In contrast, the k_{ET} of azurin on a SAM directly on the electrode showed a k_{ET} of 12–20 s^{-1} and $\beta = 0.9/CH_2$ [256].

4.3.3. Superoxide dismutases (SODs)—The pH dependence of k_{ET} has been studied for three kinds of superoxide dismutases (SODs), bovine erythrocyte copper-zinc superoxide dismutase (Cu/Zn-SOD), iron superoxide dismutase from *Escherichia coli* (Fe-SOD), and manganese superoxide dismutase from *E. coli* (Mn-SOD) [257]. These enzymes were investigated using a SAM of 3-mercaptopropionic acid on a gold electrode. The electrochemical properties (formal potential, reversibility of electrode reactions, kinetic parameters, and pH dependence) are different for each SOD, suggesting the mechanisms of ET are not the same. k_{ET} was calculated using Laviron's method and showed the fastest electron transfer for all three SODs occurred at a neutral pH.

5. Monolayer formation

The homogeneity of the SAM is of the utmost importance for accurate measurements of k_{ET}, λ, and H_{AB}. The SAM structure is significantly influenced by the method of SAM formation, choice of the electrode material, terminal groups on the diluent, and attachment of the redox center. The electrochemical techniques described in Section 2 are highly sensitive to the integrity of the SAM. Here, we describe SAM formation, types of SAM defects, SAM modification, and electrochemical characterization of SAM structures.

5.1. SAM structure

The spontaneous adsorption of thiols and disulfides on gold to form well-ordered SAMs was first reported in the 1980's [258–268]. The formation of a SAM is often depicted in schemes as uniformly aligned molecules on a flat surface. However, it has been recognized that *a wide variety* of defects are possible such as pinholes, collapsed sites, islands and domains (Figure

5.1) [269]. Typically, the first assumption is that the metallic surface upon which the SAM is formed is uniformly flat. Scanning techniques show a variety of features such as terraces, steps, and crystalline boundaries [270–277]. The choice of electrode metal is an important factor in determining the SAM integrity. While mercury is a liquid, forming featureless, defect free surfaces [278], the polycrystalline surfaces of gold, silver, and other metals are prone to atomic scale defects that can complicate SAM formation and ET measurements. A second assumption is that the organic molecules of the SAM align uniformly. The tilt angle of alkane thiols can cause significant variation in the monolayer packing [279]. At early stages of SAM formation, alkane thiols lay flat across the surface [270,280,281]. Over time, the majority of the monolayer molecules equilibrate, and align with the molecular axis normal to the surface. However, some of the chains remain flat on the surface. Molecular vacancies in the monolayer are known as pinholes [270].

5.2. Electrochemical assays for SAM defects

Electrochemical techniques are highly sensitive to nanometer scale monolayer defects that are difficult to discern using scanning techniques (e.g., STM, AFM) [282,283]. Pinhole defects have been identified electrochemically and modeled as an array of ultramicroelectrodes [103, 273,284–286]. Ferrocene alkane thiols have been used to electrochemically label fast exchange defect sites [283]. Lennox et al. have shown that cyclic voltammetry can be used to electrochemically distinguish collapsed sites from pinhole defects using a ferrocene label [287,288].

Cyclic voltammetry is most often used to interrogate the structure and dynamics of SAMs. A disordered SAM allows electrolyte to approach the electrode surface, increasing the capacitive current [37,43,289]. In one of the first SAM ET studies, the capacitance of hydroxyalkane thiol SAMs of varying chain lengths (from 2 to 16 methylene units) was examined [38]. Using cyclic voltammetry, it was shown that the capacitance decreased as the number of methylene units increased, with capacitances ranging from 12.6 $\mu F/cm^2$ for 2 methylene units to 1.36 $\mu F/cm^2$ for 16 methylene units [38]. This result suggested that the monolayers were free from pinhole defects (Figure 5.2) [38].

A unique example of controlling SAM porosity takes advantage of the reversible photoisomerization of azobenzene. The ferrocenylazobenzene functionality has been attached to an ITO electrode in a variety of ways [290–293]. Upon UV irradiation, the interfacial barrier between the solution and the ITO surface becomes more compact. For a loosely packed SAM with a terminal ferrocene and an azobenzene group on ITO, the Laviron approach was used to determined the k_{ET} before($0.24\ s^{-1}$ and after ($0.11\ s^{-1}$) UV irradiation (Figure 5.3) [292]. The decrease in k_{ET} is attributed to the change in the microenvironment around the ferrocene moiety in the SAM corresponding to the *trans*-to-*cis* photoisomerization of the azobenzene N-N bond. The porosity of the monolayer film decreases as well, as determined by the ability of the SAM to block counterions [290,292].

5.3. Effects of SAM defects on electron transfer measurements

Monolayer defects give rise to a range of local environments in which ET can occur, resulting in a distribution of observed rates, also know as kinetic dispersion or kinetic heterogeneity. The effect of this distribution of rates on electrochemical response has been computationally modeled [75,294]. Murray and coworkers have reported a model of the effects of kinetic dispersion arising from either a Gaussian distribution in the formal potentials $E^{0'}$ of surface ferrocene sites, a distribution in the value of λ, or a distribution in the tunneling distance [75]. Fitting Tafel plots derived from calculations incorporating a Gaussian distribution of $E^{0'}$ gives erroneously low values of λ and high values for k_{ET} as compared to the values expected for a

homogeneous population of kinetic sites. According to this model, a Gaussian distribution of λ*s*' has a similar effect on the appearance and analysis of the data.

If the distance between the redox sites and the electrode can be described by a distribution of values, the observed CV peak shape will not be ideal [295]. A mathematical model of this spatial inhomogeneity has been developed and indicates that broad, asymmetric CV peak shapes will result [295]. Distributions of $E^{0'}$ and λ can arise from ion pairing, Fc—Fc interactions, or a distribution of monolayer structures corresponding to various solvation shells. If these types of kinetic dispersion are present, k_{ET}, H_{AB} and λ cannot be determined accurately.

Pinhole defects can be quantified using electrochemical techniques that estimate the effective fractional surface coverage of a monolayer, θ [296]. This value represents the area that is blocked by the SAM and is therefore unavailable for electron transfer. A fraction of the electrode surface area (1 - θ) is accessible to a redox species in solution. Using Equation 5.1 where $R_{CT}°$ is the charge transfer resistance of bare gold and R_{CT} is the measured charge transfer resistance, θ can be determined.

$$\theta = \frac{\left(R_{CT} - R_{CT}^{\circ}\right)}{R_{CT}} \tag{5.1}$$

5.4 Formation of SAMs

In many cases, the alkane thiol (or other bridge) is attached to the redox species before the monolayer is formed [1,297]. This attachment is frequently a synthetically accessible reaction such as C-C bond, amide, or ester formation [45,195,298,299]. Defects are typically avoided by using low concentrations (~1 mM thiol), long bridge lengths [1,266], long adsorption times [45,299,300], thermal annealing procedures [76,83], annealing by multiple immersions or extended immersion in a second diluent-only solution [3,70,83].

Typically, ferrocene-labeled SAMs are formed by exposing electrodes to dilute solutions of ferrocenyl alkane thiols (0.1 mM) and diluent alkane thiols (1.0 mM thiol) [1,76,297,301]. The k_{ET} has been measured for bridge lengths of 7–17 CH_2 groups, various diluents, and three different linkages between the ferrocene and the bridge (C-C, ester, amide). The results are summarized in Table 1.1. The utility of this approach is due to the solubility of ferrocene in organic solvents, making it compatible with the alkane bridge.

The complex $[Ru(NH_3)_5(4\text{-AMP})]^{2+}$ has been peptide-coupled to a carboxylic acid-terminated alkane thiol and used to form a SAM [297]. While reproducible, this approach yielded monolayers that showed multiple signals in the CV. A second peak was removed by annealing procedures, and was attributed to the presence of $[Ru(II)(NH_3)_4(py)_2]$ based on the redox potential. The electron transfer parameters were evaluated, however this approach was ultimately abandoned in favor of coupling the metal center to the SAM after SAM formation (See Table 1.1, and section 5.6)

The earliest report of incorporation of Os(II) into a SAM uses $[Os(bpy)_2(dipy)C1]^{+}$(dipy = 4,4'-trimethylenedipyridine) CV of these Os(II) SAMs on Pt electrodes indicates that ion-pair formation between perchlorate anions and the cationic head groups strongly influences the energetics of the system. The Laviron method was used to estimate the k_{ET} with a lower limit on the order of 10^5 s^{-1} [302].

CV and the Laviron method was used to probe three different attachments of Os(II)(bpy) complexes to gold electrodes [303]. Alkane thiols of differing lengths (3,11, and 16 CH_2 groups) were attached by an amide group to the Os(II) complex. Either a thiol or an

aryldiazonium group was used to bind to the gold surface. The best fit using the Laviron treatment for C11 and C16 (α=0.5) gave k_{ET} values of 1,870 and 8 s^{-1} respectively.

Direct comparison of a conjugated and saturated bridge has been reported using [Os $(bpy)_2(bpe)Cl]^+$ [304]. Despite the conjugated bridge and short electron-transfer distance, the voltammetric response is best modeled as a through-space tunneling process. The k_{ET} for the conjugated bridge is 9.4×10^4 s^{-1} and is approximately a factor of 30 *smaller* than that observed for the saturated bridge, 1,2-bis-(4-pyridinyl)ethane. The proposed reason for this difference was attributed to the flexibility of the saturated bridge which allows the redox center in this system to move closer to the electrode. In contrast, the conjugated bridge attaching the redox center to the bridge is rigid, preventing close approach to the electrode. This results in a larger coupling and shorter distance for the saturated system, leading to faster k_{ET} vs. the conjugated system for the through-space ET reaction.

5.5 Attachment after SAM formation

Due to the synthetic challenge of attaching a redox center to a monomer chain, or the limited availability of redox-active species (i.e., metalloproteins), it may be desirable in some cases to covalently attach a redox molecule to a monolayer that has already formed [14,17,45,127, [128],[157],192,236,305–320]. If the terminal group is bulky, coadsorption with a diluent has been shown to improve packing (Figure 5.4) [321–323]. There are two ways SAM attachment can be accomplished: (1) incorporating a coordinating ligand into the monolayer that binds to the metal center or (2) forming a bond between a functional group on the monolayer surface and a functional group on a ligand of the metal center. Both approaches have been used to immobilize metalloproteins and small molecule redox centers on SAMs [17,45,127,128,[157], [192],236,305,312,314].

Several groups have reported using a terminal group of the SAM as a metal binding ligand [221,312,314]. Van Ryswyk et al. utilized the lability of H_2O in $[Ru(NH_3)_5(H_2O)]^{2+}$ [314]. The aquo ligand was replaced by terminal pyridine functionalities in a monolayer of 11-mercaptoundecyl isonicotinamide [314]. The reaction was carried out by soaking the monolayer-coated electrodes in a solution of $[Ru(NH_3)_5(H_2O)](PF_6)_2$ in THF under argon. Little or no substitution of the aquo ligand was observed if the soaking was done in H_2O, however substantial substitution occurred in THF. A dissociative mechanism of substitution is suggested to explain this result. After the loss of water, either reaquation or reaction with a pyridine group can occur. The use of a non-coordinating solvent such as THF slows the reaquation process. Another explanation is that the monolayer is more fluid in THF than water, increasing the degrees of freedom of the terminal pyridine groups to compete with the reaquation process [312,314].

Ligand substitution of terminal pyridine or imidazole groups with *trans*-$[Ru(II)(NH_3)_4(SO_3)(H_2O)]$ has been used to attach the ruthenium complex to a pre-formed SAM with a terminal pyridine L_1 (Figure 5.5) [312]. This reaction can be carried out in a similar manner as described, except it can be performed in aqueous solutions and is complete in 10–15 minutes. This step was followed by exposure to H_2O_2 to convert the SO_3 ligand to SO_4 and to oxidize the Ru(II) center to Ru(III). Electrochemical reduction of this complex results in the formation of *trans*-$[Ru(II)(NH_3)_4(H_2O)(L_1)]$-SAMs. The labile aquo ligand of these redox-modified SAMs can be substituted with a variety of N-heterocyclic ligands L_2.

One explanation for the high yield of formation of *trans*-$[Ru(II)(NH_3)_4(SO_3)(L_1)]$ in aqueous solutions is that since the *trans*-$[Ru(II)(NH_3)_4(SO_3)(H_2O)]$ is a neutral complex, it can more easily associate with the hydrophobic monolayer interface than can the charged complex $[Ru(NH_3)_5(H_2O)]^{2+}$. Electron transfer kinetic experiments for redox-modified monolayers formed

using these types of substitution reactions show rates of electron transfer that are comparable to monolayers formed using a mixture of redox-modified and diluent alkane thiols.

A SAM was modified with *trans*-[Ru(III)$(NH_3)_4(SO_4)$(L)] (where L=histidine) by the reaction of a carboxylic acid terminated monolayer with the histidine amine and EDC [312]. Experiments showed electron transfer rates similar to monolayers formed using redox-modified alkane thiols, but a rate for electron transfer was not reported.

Covalently attaching a redox molecule to a monolayer post-formation has been successfully applied in a number of cases [45,157,192]. A popular approach is to use peptide coupling procedures, in which a carboxylic acid is conjugated to a primary amine using a peptide coupling reagent such as EDC. An example of this approach was used in the formation of monolayers of differing lengths of mercaptocarboxylic acids modified with $[Ru(NH_3)_5$(4-AMP)$]^{2+}$ [45]. The peptide coupling reaction was performed by soaking the mercaptocarboxylic acid monolayer-coated electrode in a solution of EDC and $[Ru(NH_3)_5$(4-AMP)$]^{2+}$.

A comparison of the k_{ET} between Fc-terminated SAMs directly attached to the alkyl chain and attached via an amide linkage has been compared [84]. It was found that the k_{ET} through an identical number of bonds for the two systems was nearly identical, thus, ET through an amide linkage is similar to ET through an alkane linkage [82,84].

Covalent attachment of $[Os(II)(bpy)_2$(4-AMP)$(H_2O)]^{2+}$2 to mixed monolayers of 16-mercaptohexadecanoic acid and either 12-mercaptododecanol or 16-mercaptohexadecanol has been reported [157,192]. (Figure 5.6) The peptide coupling was performed by placing the preformed mixed monolayer in a solution of the osmium complex and EDC in either pH 7 phosphate buffer or acetonitrile with a few drops of water. These Os(II) complexes were used to study the pH dependence of ET (Section 4.2). At pH 7.2, the k_{ET} was found to be 9.9 s^{-1}.

Besides peptide coupling, another method for attaching redox species to a preformed monolayer which has been explored is “click” chemistry [127]. (Figure 5.7) After forming mixed monolayers consisting of azidoundecanethiol and decanethiol as diluent, the modified electrodes were placed in solutions of alkynyl ferrocene, copper(II) sulfate and sodium ascorbate. The reaction time was found to be on the order of minutes [128]. In addition, by varying the lengths of the functionalized and diluent alkane thiols, the authors showed that k_{ET} could be tuned from 1 to 60,000 s^{-1}. The triazole linkage provides good electronic coupling between the ferrocene and the alkane thiol, similar to that for ester linkages [305]. A fast reaction time and well-behaved redox chemistry make these “clicked” ferrocene SAMs useful for a wide variety of electron transfer studies.

6 Bridge and diluent

The bridge is a key component of SAMs, controlling the distance between the electrode and the redox center, and thereby controlling the H_{AB} and k_{ET}.(Figure 1.1) Long length bridges are typically used in order to slow the electron transfer rate to a measurable value. The structure of the bridge is key to controlling the electronic coupling and this factor is evaluated in terms of the decay constant β given by Equation 6.1, where *A* is a preexponential factor, and d is the bridge length. Saturated and conjugated bridges have been investigated as well as functional bridges such as peptides [1,3,78, 353]

$$k_{ET} = Ae^{-\beta d} \tag{6.1}$$

6.1 Alkane bridges

Alkane thiols on gold are the most common type of monolayer that has been studied due to their stability and ease of preparation [21,269,324]. Not surprisingly, long chain alkane thiols have been shown to form well-packed, highly ordered monolayers superior to those formed from short alkane thiols. The van der Waals interactions within the monolayer are stronger for the more hydrophobic long chain alkane thiols and weaker for short chain alkane thiols [324]. Another factor is solubility; long chain alkane thiols are less soluble in the solvents generally used for monolayer depositions, and it is energetically more favorable for them to pack closely together to form a well-ordered monolayer [260,301].

As predicted by theory, k_{ET} decreases as the length of alkane thiols increases [301]. For example, k_{ET} between a ferrocene bound to a monolayer with a series of alkyl bridges (5–13 methylene units) and a gold electrode was found to vary from 10^2 s^{-1} for the longest alkyl chain, to 3×10^7 s^{-1} for the shortest alkyl chain [300].

In general, the decay constant, β, for electron transfer through alkane thiols on gold has been measured to be approximately 1.1 per methylene unit (Equation 6.1) [42,81,299,300]. The tunneling constant varies, however, with respect to the position of the redox species in relation to the diluent. This was demonstrated for monolayers with series of $[Ru(NH_3)_5Py\text{-}CH_2NHCO(CH_2)_nSH]^{2+/3+}$ complexes with diluent $HS(CH_2)_mCOOH$ in which n = m, n > m (the ruthenium was exposed to the bulk solution), and n < m (the ruthenium was buried in the monolayer) [76]. For the n = m case, β is 0.97. For the n > m case, β is 0.83. For the n<m case, β is 0.16 per methylene. This variation in tunneling constants is indicative of different electron tunneling paths through the monolayer depending upon the position of the redox species relative to the diluent species of the monolayer.

In another study it was found that if one of the internal bonds of an alkane thiol monolayer is an alkene or alkyne, the rate of electron transfer through the monolayer decreases. This result is attributed to a decrease in H_{AB} [325]. H_{AB} between the redox species and the electrode is dependent upon the overlap of the σ and σ* orbitals of the individual atoms in the hydrocarbon chain of the bridge with the orbitals of the nearest neighboring 2–3 atoms [40,326–329]. Interrupting this σ and σ* orbital overlap within the bridge by an alkene or alkyne results in two, long, through space interactions. The result is a less effective electronic coupling pathway as compared to unmodified alkane thiol bridges [325].

One important, and subtle aspect of alkane thiols SAMs is whether there is an odd or even number of methylene units in the alkyl chain. (Figure 6.1) Alkane thiols on gold exhibit a tilt angle of ~30° defined with respect to the surface normal, regardless of the chain length [266]. Due to this tilt angle, the terminal CH_3-CH_2 bond is perpendicular to the electrode surface for $CH_3(CH_2)_nS$-Au where n is *odd*. The surface for these SAMs consists of methyl groups. For $CH_3(CH_2)_nS$-Au where n is *even*, the terminal CH_3-CH_2 bond is tilted with respect to the normal of the electrode surface, thus the surface consists of both the methyl and methylene groups [279].

For alkane thiol monolayers on electrodes other than gold, the tilt angle tends to decrease as the chain length increases. The decay constant for superexchange (tunneling) is affected by the tilt angle of the alkyl chains in the monolayer, and is not a constant 1.2 per methylene unit [330]. As a result of the difference in structures, SAMs with an *odd* number of methylene units show slightly slower electron transfer rates than SAMs an *even* number of methylene units [73,84]. The odd-even effect in SAMs has been widely investigated and a review focusing on this topic has recently appeared [279].

6.2 Functional groups

The most common terminal functional groups employed in SAMs on gold include: -CH_3, -OH, and -COOH. (Figure 6.2a) Methyl terminated SAMs were discussed in the previous section. Hydroxyl terminated SAMs have been found to have a tilt angle of 28°, similar to alkane thiols [331]. Compared to alkane thiol SAMs, it has been found that hydroxyl terminated SAMs are slightly more defective and permeable, despite the fact that the terminal –OH provides a more favorable interface with water [37]. The decay constant β has been determined to be 0.9 per methylene unit for hydroxyl terminated SAMs, similar to the value for alkane thiols [37]. In addition, introducing a polar group to the surface of a monolayer affects the apparent formal potential and apparent k_{ET}. Determination of k_{ET} by CV of these monolayers causes k_{ET} to appear slightly slower than they actually are, due to an increased double layer capacitance [73].

Acid terminated monolayers have been shown to be more permeable to water and aqueous ions and have more defects than hydroxyl terminated monolayers [37]. This behavior is due to hydrogen bond formation between the terminal COOH moieties before the monolayer forms well-ordered close-packed SAMs (due to the hydrophobic interactions of the alkyl chains) [324]. The tilt angle was found to be 32°, similar to –CH_3 and –OH terminated SAMs [331]. Despite their disorder and permeability, acid terminated SAMs can be easily modified chemically after the monolayer has been formed, an attractive property of this class of SAM [45,157,192].

In addition to amides, acids can be converted to esters. It has been shown that there is some degree of disorder in monolayers with ester functionality [314]. The tilt angle for these monolayers was measured to be 35° [314]. Ester hydrolysis measurements have been performed, and the rate for the reaction on monolayers was found to occur, but was significantly slower for monolayer esters than for esters in solution.

6.3 Conjugated bridges

Molecules that are highly conjugated and conduct large currents via fast electron transfer between contacts are referred to as molecular wires [332]. The most studied molecular wires are oligo(phenyleneethynylenes) (OPEs) and oligo(phenylenevinylenes) (OPVs) (Figure 6.2b) [21,324]. Monolayers incorporating these moieties were found to have similar ordering as alkane thiols with slightly smaller tilt angles, due to the rigidity of the system and the bulkiness of the phenyl rings [269].

As the number of phenyl rings increases in OPEs, the overall order of the monolayer structure increases [333]. The β for OPE SAMs was found to be between 0.36–0.57 $Å^{-1}$ [3,254]. This value is intermediate between saturated systems and conjugated systems (β = 0.2 for polyenes) [334,335]. For a monolayer consisting of six phenylethynyl units, k_{ET} was found to be 350 s^{-1} using the ACV method [3].

For OPE systems, k_{ET} was measured using ILIT and the ACV method and found to be independent of the diluent [57]. Conversely, when OPE is the diluent, it has no effect on k_{ET} through alkane thiol bridges [57]. The k_{ET} between ferrocene and a gold electrode through an OPE monolayer is dependent upon the conformation of the molecule [57]. This conformational dependence has been attributed to the fact that there is a low barrier to for phenylene rotation about the ethynyl bonds, reducing the conjugation of the system [45,57]. This dependence explains why the tunneling decay constant is an intermediate value between the decay constants for saturated monolayers and conjugated systems.

For similar molecules, the rates measured using ILIT are significantly different from the rates measured using the ACV method.[3] It was suggested that the AC signals may be inaccurate

due to the cell time constant R_uC_{film} where R_u is the uncompensated solution resistance. Further, the surface coverage used in the ACV measurements is much lower than in the ILIT measurements.

OPVs are expected to be more conjugated than OPEs because phenyl rotation is less likely in these types of systems [336,337]. In general OPVs have fast k_{ET}s, greater than 10^4 s^{-1}, for molecules longer than 35 Å due to their highly conjugated nature [336]. These fast electron transfer rates show that coupling between the redox center and the electrode is not a limiting factor for ET through OPVs up to 28 Å in length [44]. The large coupling prevents the measurement of changes in k_{ET} with increasing monolayer thicknesses (longer OPVs), making the mechanism for ET (hopping vs. tunneling) through OPVs ambiguous [44,338].

To determine the appropriate mechanism, measurement of the energy levels of the HOMO of the donor and the LUMO of the OPV were performed [20,338]. For an electron to be injected into the OPV (a hopping mechanism), the energy of the HOMO of the donor must overlap with the energy of the LUMO of the OPV. For a system in which Fc was covalently attached to an OPV, energy level measurements showed a large energy gap between the HOMO of Fc and the HOMO and LUMO of OPV. This allowed the authors to rule out a hopping mechanism and determine that ET for this system occurred by a tunneling mechanism [338]. For a system in solution in which a tetracene donor was connected to a pyromellitimide acceptor by an OPV bridge, the energy of the HOMO of the donor was found to be similar to the LUMO of the OPV. In this case, ET was determined to occur by a hopping mechanism [20,338]. As both tunneling and hopping mechanisms have been shown to occur, knowing the relative energy levels of the donor/acceptor and the bridge is important in these types of conjugated systems [20].

For long OPVs in solution, a temperature dependence on the k_{ET} has been observed due to torsional motions of the molecule [339]. These torsional motions decrease overlap between the π orbitals of the OPV. Decreased overlap slows k_{ET}, and the result is conformational gating of ET for OPV systems in solution. Although conformational gating is significant for OPVs in solution, there is little conformational change in OPV monolayers and k_{ET} is not significantly slowed for these systems.

Recently, a series of norbornane-based monolayers has been studied (Figure 6.2c) [86,102, 340–342]. For a norbornylogous bridge 21.3 Å long (Figure 6.2c), the k_{ET} from a ferrocene attached by 18 bonds to the electrode was found to be faster than expected: three times faster than for an alkane thiol of the same length [102,341]. Despite this faster rate, the mechanism of electron transfer through the norbornylogous SAM was found to occur by nonresonant tunneling [342].

Early versions of the norbornylogous bridges were found to have a high amount of curvature [341,342]. The curvature depends on the length or how many norbornyl units are used. Shorter versions have been synthesized such that the curvature is negligible. These monolayers have been found to have a tilt angle of approximately 30° with a β value of 0.80 $Å^{-1}$ [340].

6.4 Peptide bridges

Long range ET through proteins has received significant attention due to the importance of ET in biological processes [27,28,30–33,106,214,246,343]. The majority of this work has utilized flash photolysis approach to determining ET [30,65,106,344–352]. These studies have shown that the efficiency of the coupling between redox centers is determined by the 3D structure of the intervening peptide matrix. The protein structure is the fundamental regulator of ET, controlling ΔG, λ, and the H_{AB} [247]. Only recently have electrochemical methods been used to study ET through (relatively) short peptides on SAMs [78–80,353–358].

A number of leucine-rich ferrocene-terminated helical peptide SAMs on gold have been examined. [78–80,355,357,358]. In general, vertical orientation and tighter packing of the monolayer appears to suppress the electron transfer rates. The observed electron transfer appears to occur intermolecularly and may be associated with molecular motion [79,80]. Three mechanisms are proposed: (1) electron tunneling gated by a helix contraction, (2) electron tunneling coupled with helix conversion from R-helix to 3_{10}-helix, and (3) electron hopping along the backbone via the amide groups. (Figure 6.4)

Mandal et al. have studied the effects of the peptide helix dipole moment on ET using leucine-rich ferrocenyl peptides [354]. SAMs were formed in which either the dipole moments of the peptides were aligned or were in opposition. Reflection absorption infrared spectroscopy (RAIRS) revealed that the dipole-opposed peptides are more vertically oriented than the dipole-aligned peptides. Importantly, the ET properties are significantly different, rationalized by differences in the molecular dynamics of the two films. The k_{ET} was determined from CV data using the Butler–Volmer methodology. The dipole-opposed SAM exhibited a much slower k_{ET} than in the dipole-aligned SAM ($k_{ET} = 1.2 \times 10^{-3}\ s^{-1}$ vs. $1.5 \times 10^{-2}\ s^{-1}$).

Mixed SAMs of oligoglycine derivatives ($FcCO(Gly)_nNH(CH_2)_2SH/CH_3(CH_2)_XSH$ (n = 2–6) were assembled on gold and investigated using CV and ACV methods [356]. The rates of electron transfer through these bridges decrease rapidly with distance for short chain derivatives, with k_{ET} ranging from $9000 - 1\ s^{-1}$. A less pronounced distance dependence is observed for longer bridges ($n \geq 5$). Differences in the secondary structure of the peptide bridges or a change in the ET mechanism from tunneling to hopping are considered as possible reasons for the difference of the rate constants.

Ferrocenyl groups were attached to a cyclodecapeptide (designed for anion sensing) and immobilized on a gold electrode [359]. Using CV, the Laviron method was applied only to the cathodic branch of the E_p vs. υ plot (only for overpotentials higher than 0.1 V) as the anodic wave became indistinguishable at scan rates > 100V/s. The k_{ET} was found to be $6350 \pm 2000\ s^{-1}$ and $\alpha = 0.2 \pm .05$. The redox potential shifts dramatically in the presence of phosphate anion in acetonitrile.

A peptide sequence with alternating glutamic acid and leucine amino acids (HELELELELELC) was modified with a $Ru(NH_3)_5$ group at the histidine end and used to form SAM on gold via the cysteine at the other end [360]. The peptide was designed to have a pH dependent secondary structure, allowing the study of structure-dependent ET. At low pH the carboxylic acid groups are protonated and the peptide has a compact helical structure. At high pH, the carboxylic acid groups are deprotonated leading to an extended conformation due to the electrostatic interactions between carboxylate groups. The pH-sensitive conformation of the peptide was predicted by molecular dynamics simulations and confirmed by electrochemical measurement. The electron transfer is fast at low pH values (78, 110, and 230 s^{-1} at pH 3.0, 2.0, and 1.0 respectively). The k_{ET} decreases gradually as the pH is increased, and is completely suppressed at pH 6.9.

Short ferrocenoyl-peptide cystamines were used to form poorly packed SAMs with a uniform thickness of 7 Å [353]. 10–15% of the Au surface is exposed as determined by Cu underpotential deposition [353]. The k_{ET} values were estimated using the Butler-Volmer formalism and are in the range of $5–8 \times 10^3\ s^{-1}$. Diluting the monolayer with hexanethiol resulted in faster redox kinetics. This was attributed to a “stiffening” of the monolayer.

6.5 Nucleic acid bridges

Charge transfer in DNA has been widely investigated [361]. A number of electrochemical studies of ET in DNA using SAMs have been undertaken [6,9,362–370]. Meade and coworkers

covalently attached metal complexes into DNA [9,10,138,371] and developed a sensitive electronic detection system for point mutations based on site-specific incorporation of ferrocenyl derivatives into DNA oligonucleotides [6,362,363]. Barton and coworkers have used the intercalating organic redox species daunomycin and methylene blue either covalently or noncovalently attached to DNA in SAMs. The results are sensitive to perturbations in the DNA structure and suggest that base stacking is required for charge transfer in these systems [364–366]. Using ferrocene-terminated ds DNA (20 base pairs), Kraatz and coworkers report a charge transfer rate of 25 s^{-1} if the ferrocene is on the 3' end of the complimentary strand and 115 s^{-1} if it is on the 5' end of the DNA strand attached to the electrode via the alkane thiol bridge [368]. The authors conclude that there is either an energetic barrier to interstrand crossing or the 5' Fc is more accessible to the base pairs than the 3' Fc [368]. Anne and coworkers report a conformational gating effect using ferrocene attached to ss DNA in which the DNA bends such that the ferrocene can closely approach the electrode surface [369,370].

Peptide nucleic acid (PNA) oligomers provide an attractive alternative for examining nucleic acids in SAMs. PNA strands are based on an aminoethylglycine backbone (Figure 6.5) and form duplexes via Watson-Crick hydrogen bonding. The backbone is neutral, providing an advantage for surface studies in that the strands do not repel each other on the surface.

SAMs of single-stranded PNAs (ssPNAs) containing 3 to 7 thymine (T) nucleotides, a C-terminus cysteine, and an N-terminus ferrocene group were formed on gold electrodes[135]. The β for these SAMs was determined to be about 0.9/Å. The k_{ET} ranges from 2000 s^{-1} for 3 bases to 0.02 s^{-1} for 7 bases.

SAMs of ssPNAs with the sequence T3-X-T3 were investigated for X=C, T, A, G, CH_3. (Figure 6.5) The charge transfer rate constants for these SAMs depend on the identity of the nucleobase X ranging from 0.014 to 0.067 s^{-1} [136]. The CH_3 group gave the slowest rate of charge transfer (<0.005 s^{-1}. Computational studies were undertaken and indicate that charge transfer through the PNA SAMs occurs by hole-mediated superexchange. A correlation between the charge transfer rate constant and the oxidation potential of X was noted [136].

Recently, charge transfer in PNA SAMs consisting of either ss Cys-Tn-Fc, ss Cys-An-Fc, or ds Cys-(AT)n-Fc were studied using CV [372]. For short ssPNA SAMs, the charge transfer rate decreased rapidly with increasing PNA length according to a superexchange-mediated tunneling mechanism. For long ss and dsPNAs, the charge transfer rate had a weaker distance dependence and correlated with the oxidation potential of the nucleobases, indicating that a hopping mechanism occurs [372]. This PNA length-dependent transition between the superexchange and hopping mechanisms can be rationalized by the tight-binding model proposed by Ratner and coworkers [373].

7. Electrode materials

The choice of electrode material is important to the measurement of k_{ET} due to the implication of the density of electronic states in Marcus theory. The most widely used electrode metals for thiol-based SAMs ET measurements are gold and silver. However, the formation of SAMs on other metals such as nickel, copper, palladium, mercury and platinum has been investigated. Thiols have a high affinity for these metals and form densely packed monolayers. However, few reports exist in which ET kinetics have been directly compared for SAMs on these metal surfaces. Finally, semiconducting materials have been examined as substrates for SAM k_{ET} measurements [292,374,375].

7.1 Effects of electrode material – theory and experiment

The theoretical effect of the density of electronic states (DOS) at the Fermi level of a metal (Pt and Au) on k_{ET} has been examined by Gosavi et al. [376]. k_{ET} was calculated for the electron transfer through alkane thiol SAMs on either Pt or Au. The s electrons dominate the DOS for metals such as gold and silver. The DOS near the Fermi energy is a factor of 7.5 higher for Pt than for Au however, due to the overlap of the d band states with the Fermi energy in Pt. The electronic coupling per state is significantly weaker for the d band states as compared to the sp band states. This difference is likely because the d band states are more localized and therefore are only weakly coupled to the redox centers in the SAM.

Finklea et al. has used a $Ru(NH_3)_5$ SAM to investigate k_{ET} on Au, Pt, and Ag for comparison to Gosavi's theoretical treatment [377]. Using CA to generate Tafel plots, the k_{ET} was compared for Au (1.0 s^{-1}), Ag (0.6 s^{-1}), and Pt (1.7 s^{-1}). The ratio of kPt/kAu (1.7) was found to be significantly lower than the predicted 7.5 predicted by the ratio of DOS near the Fermi energy. The difference between Ag and Au is in agreement with the electronic heat constants, which are proportional to the density of states near the Fermi energy (0.65 for Ag and 0.73 for Au) [71]. The results are in good agreement with the theoretical prediction that the d band states are only weakly coupled to the $Ru(NH_3)_5$ centers.

SAMs of $[Os(OMe\text{-}bpy)_2(p3p)Cl]+$ were formed on carbon-fiber, Hg, Pt, Au, Cu, and Ag microelectrodes (OMe-bpy = 4,4'-dimethoxy-2,2'-bipyridine; p3p = 4,4'-trimethylenedipyridine) and studied electrochemically to investigate how the DOS influences k_{ET} [378]. CA was used to generate Tafel plots for each electrode material. Figure 7.1 shows the best fits using Marcus DOS theory. The reorganization energy is 0.27 eV and the k_{ET} is 4.0×10^4, 1.8×10^4, and $3\times10^{\beta}$ s^{-1} for Pt, Au, and carbon, respectively.

The experimental preexponential factors are consistent with weak electronic coupling between the delocalized metallic states on the electrode and the localized redox states of the osmium complex. The ratio of the prefactors for platinum and gold is 2.9±0.7 compared with the DOS ratio of 7.5. This ratio is higher than the ratio of the k_{ET} values for the $Ru(NH_3)_5$ case, and confirms that the relationship of the electron transfer with the electrode DOS is not a simple linear relationship.

7.2 Mercury

Mercury is liquid at room temperature which offers the advantage of providing a featureless defect-free surface. Mercury has a higher affinity toward thiols than the other metals and form tightly packed SAMs that block both hydrophilic and hydrophobic redox probes [278]. A number of studies have investigated the heterogeneous k_{ET} through a SAM to a redox species in solution [278,294,379,380]. Few studies have been undertaken to measure k_{ET} of a redox active SAM on mercury. In one case, attempts to form SAMs of $HO_2C(CH_2)_{15}SH$ on Hg followed by coupling to $[Ru(NH_3)_5(4\text{-}AMP)]^{2+}$ were unsuccessful [377]. The authors observed formation of multilayers of $HO_2C(CH_2)_{15}SH$ rather than SAMs, a peak attributed to desorption of the thiol at −0.6V vs. SCE, and nonideal behavior of the Ru(II/III) couple.

Defects in alkane thiol SAMs on Hg have been studied using a variety of methods. Using hexadecanethiol, Demox et al. report high density SAMs that are impermeable to $Ru(NH_3)_6^{3+}$ [278]. Potential-induced ion gating attributed to SAM defects are reported [294]. A C_{60}-alkane thiol monolayer on a Hg film electrode showed electrochemical blocking of redox species in solution and a high degree of hydrophobicity [175]. SECM was used to evaluate pinholes in a SAM of alkane thiols of different chain lengths ($CH_3(CH_2)_nSH$; n = 8, 10, 11, 15) on Au and Hg surfaces using $FcCH_2NHCO(CH_2)_{12}SH$ and ferrocene-terminated polynorbornyl (FcNB) thiols [102]. Pinholes were identified by the growth of Pd nanoparticles.

A model was developed for the correction of k_{ET} for the presence of pinholes [102]. The FcNB species gave a k_{ET} of 189 s^{-1} similar to $FcCH_2NHCO(CH_2)_{12}SH$ of the same length.

7.3 Silver and copper

In the case of Ag and Cu, well-ordered SAMs can be formed on freshly evaporated films that are handled in an inert atmosphere [381]. The tilt angle of alkane thiols on Ag and Cu surfaces is smaller than the tilt angle for SAMs on gold, and no odd-even effects have been observed.

In contrast to gold, an oxide layer forms on these metals upon exposure to air. Alkane thiol SAMs form on these oxidized surfaces, however they differ in structure and properties from SAMs formed on less oxidized surfaces. It has been shown that a redox reaction takes place between the metal oxide and the alkane thiol molecules [382,383]. The alkane thiols are oxidized to sulfonates accompanying reduction of silver and copper oxides [382,383]. These reduced surfaces react with a second equivalent of alkane thiol to form the SAM. Copper has not been reported for ET SAM studies. Silver is widely used for SERRS and numerous examples of metalloprotein k_{ET} measurements using SAMs on silver are given in Section 4.3.

7.4 Nickel

Thiols on Ni form homogeneous monolayers as ascertained by XPS, Auger electron spectroscopy, and electrochemical surface coverage [384,385]. At ambient pressure and temperature, Ni forms an oxide layer that must be removed prior to SAM formation. Mekhalif et al. reported a two-step procedure involving electroreduction of the oxide layer immediately followed by immersion in an alkane thiol solution. However, exposure to atmosphere between steps allows some oxide to form [386]. In a more recent report, electroreduction concurrent with SAM formation on Ni surfaces was demonstrated using basic solutions saturated with alkane thiol [387]. The optimal applied potential for electroreduction of NiO was determined by measuring the surface coverage of $Fc(CH_2)_{11}SH$ on electroreduced samples [388].

7.5 Palladium

For SAMs on crystalline Pd, the alkane chains are conformationally disordered for short chain lengths and are dense and crystalline at long chain lengths, similar to monolayer ordering on Ag and Au [389]. Alkane thiol SAMs provide Pd with a resistance to corrosion that is independent of the alkane chain length [390]. XPS data reveal a complex palladium sulfide interphase that appears to enhance the SAM stability against corrosion [389,391]. The potential of reductive desorption of alkane thiols on Pd does not change significantly with the hydrocarbon chain length, unlike Au, Ag, Pt, and Ni which do not have an analogous metal-sulfide interphase [392].

OEG-terminated SAMs on palladium are resistant to nonspecific adsorption of proteins and the adhesion of mammalian cells [393]. Patterned OEG-SAMs resisted the invasion of cells for over four weeks while SAMs on gold remained patterned for only two weeks under the same conditions [393]. SAMs on palladium may be better for microcontact printing [394].

Palladium surfaces of high roughness have been deposited on glassy carbon electrodes from a variety of electrolytes (alkaline, neutral, and acidic) using two palladium chloride complexes ($PdCl_2$ and Na_2PdCl_4) [395]. Decanethiol and butanethiol SAMs on these Pd surfaces block the redox reaction of species in solution. Importantly, the hydrogen evolution reaction is suppressed.

7.6 Semiconductors

High stability monolayers on silicon may be formed through hydrosilation chemistry due to the strength of the Si-C bond, which affords much greater stability that the analogous

monolayers formed with gold-sulfur linkages [396]. Electronically passivating a silicon surface using the native oxide layer that typically forms is useful, but cannot be readily modified for specific applications. However, organic monolayers have the potential to serve as passivators that may be specifically tailored. As of 1999, the surface chemistry of silicon material has remained largely unexplored [2]. However, understanding the surface chemistry of silicon is crucial to the rapid development of microdevices [397].

The electronic structure of the electrode influences the properties of the electrochemical interface and affects electrochemical reactions. Semiconductors possess current-carrying bands that do not overlap (as is the case for metals) and are separated by a band gap [71]. Semiconductor band gaps are typically on the order of 0.5–2 eV, rendering the conductivity quite low [71]. Enhancement of the conductivity of semiconductors can be achieved through doping. A potential difference occurs at the interface between a semiconductor surface and an electrolyte due to a difference in conductivity between the semiconductor (low conductivity), and the electrolyte solution (relatively high conductivity). A consequence of this difference in conductivity is that the potential drop primarily occurs at the boundary layer of the electrode and not at the solution side of the interface [68].

Potential drop characteristics at semiconductor interfaces are opposite to that observed on metal electrodes [68]. A variation in the electrostatic potential of a semiconductor results in band bending. A fundamental difference between ET reactions on metals compared to semiconductors is that for a metal the variation of the electrode potential varies with the molar Gibbs energy of the reaction. As the electrode potential is varied for a semiconductor the positions of the band edges at the semiconductor surface do not change with respect to the solution due to intrinsic low conductivity of the semiconductor [68].

Hybrid molecule/silicon assemblies offer two predominant advantages over analogous assemblies on gold surfaces. First, electronic properties of silicon are easily modified by selecting an appropriate dopant and dopant concentration or via generation of electron-hole pairs under illumination. Second, superior stability is afforded by interfacial Si-C and Si-O bonds as compared to Au-S bond between gold and alkane thiol adsorbates [398–400]. Si(111) surfaces can be formed with atomically flat monohydride-terminated reactive surfaces that can be further modified [401–403].

There is intense interest in controlling interface properties for applications such as sensors and biologically active surfaces [21,269]. Probing biomolecular interactions at conductive and semiconductive surfaces by impedance spectroscopy has been reviewed [91]. Through immobilization of biomaterials such as enzymes, antigens/antibodies, or DNA on electrodes or semiconductor surfaces the capacitance and interfacial electron transfer resistance can be modulated. Impedance spectroscopy is used to investigate interfacial changes as a result of biorecognition event occurring at the surface of an electrode[91].

Ferrocene and zinc (II) trimesitylporphyrins have been tethered to a Si(100) surface via a benzyl alcohol linker [374]. For the Zn porphyrin monolayer, ET rates for oxidation were found to be similar analogous thiol-derivatized Zn porphyrin on Au surfaces. However, ferrocene monolayers on Si(100) surfaces exhibited a slower k_{ET} than the corresponding alkane thiol on gold. These observations were attributed to changes in distance of the redox-centers from the surface, modulated by orientation of the linking chains [374].

The effects of varying anchor (O, S, Se) and linker on electron transfer characteristics of two classes of Zn porphyrin tethered monolayers on Si(100) surface were investigated [375]. To examine these monolayers XPS, FTIR, and electrochemical methods were used. Surface binding to Si(100) can be achieved with short (benzyl) and very short (methylene) linkers independent of anchoring atom. The orientations of these porphyrins were controlled by the

choice of linker molecule. A benzyl tether affords the porphyrin a more "upright" geometry with respect to the surface as compared to a methylene tether. k_{ET} was found to be significantly faster for the methylene linker and dependent on surface coverage (10^4–10^5 s^{-1} for Γ=0.25–3×10^{-11} mol/cm^2). The identity of the anchor did not change k_{ET} appreciably.

Vinylferrocene was anchored to monocrystalline Si(100) surface via a Si-C bond [404]. XPS and capacitance-voltage studies were described, but k_{ET} was not determined. Si(111) surfaces have been modified with ferrocene-terminated alkane monolayers [87]. Ferrocene was coupled to a carboxylic acid-terminated C11 chain. The surface coverage of the ferrocene species was controlled by diluting with inert n-decyl chains. The k_{ET} was found to be independent of surface coverage of the ferrocene redox centers at 50 s^{-1}.

7.7 ITO

Indium tin oxide (ITO) is a transparent conducting material, making it attractive as a substrate to study photoreactive electrochemical processes such as artificial photosynthesis systems [182,405]. However, few studies have been undertaken to electrochemically determine k_{ET} of an ITO-bound redox center.

A ferrocenyl trichlorosilane has been synthesized and attached to semiconductor electrodes consisting of indium tin oxide (ITO), zinc indium tin oxide (ZITO), cadmium oxide (CdO), and ITO derived from ion-beam deposition (IAD ITO) [406]. The ITO was chemically pretreated in different ways to examine the effects on the electrochemistry. The greatest ferrocene surface coverage (7.9×10^{-10} mol/cm^2) coincides with the greatest observed electron transfer rate (9.23 s^{-1}) for O_2 plasma-treated ITO. CV showed the largest ΔE_p and FWHM for IAD-In_2O_3 suggesting that the SAM on this surface is more disordered than the others.

Laviron's method was used to calculate the k_{ET} (s^{-1}): 7.12 (ZITO)>6.6 (as-received ITO) > 5.07 (IAD-ITO) > 0.42 (CdO) > 0.03 (IAD-In_2O_3). The electron-transfer rate of IAD-In_2O_3 is nearly 2 orders of magnitude less than the k_{ET} of the as-received ITO, which may be due the relatively low conductivity of 1000 S/cm. The carrier mobility is lower in semiconducting electrodes versus that in commonly used metal electrodes. Therefore, a significant lag in the potential is expected to occur between the voltage source and the electrode surface. All surface sites experience this lag, shifting the CV peaks to more extreme potentials, giving the CV a stretched appearance compared to electroactive SAMs on noble metal electrodes.

8 Modeling of SAM structure

Experimental preparation of monolayers on a metal surface by self-assembly was first reported by Zisman in 1946 [407]. As early as 1966, theoretical studies were carried out on mono- and bilayers using Monte Carlo (MC) methods motivated largely by interest in the structure and properties of biological membranes [408–414]. Current computational studies of SAMs are directed towards understanding the fundamental process of self-organization, interfacial phenomena and structure-function relationships, and charge transport in SAMs as related to molecular electronics [360,415–419].

SAM structure has been shown to have an impact on electrochemical measurements. Engineering nanoscale features of surfaces requires intimate knowledge of structure. This section focuses on modeling the structure of SAMs. These model systems focus on mechanisms of annealing, tilt angle, odd-even, and head group effects.

8.1 Early work – Molecular Dynamics

Due to growth of large supercomputers in the late 1970s and early 1980s, the application of computer methods such as MC and molecular dynamics (MD) to large multiparticle systems

has grown rapidly. The first reports of using MD to study the dynamics of monolayers were carried out in the late 1970s [420,421]. Full structural and dynamic details on the basis of simple interactions are produced from MD methods and are generally considered more powerful than MC methods. However, these MD simulations were primitive.

Toxvaerd's study of the equation of state of dense monolayers used a pairwise potential to describe the interaction between close-packed carbon chains [421]. These numerical dynamical calculations were carried out using models of rough monolayers where individual molecules were treated as purely 2-D objects (i.e., the molecules are only allowed to move in the plane of the monolayer). This treatment neglects the influence of steric interactions of the chains and the large number of possible conformations. The simulations yield a description of the crystalline state of the monolayer and the melting behavior of the molecules is not predicted.

A more sophisticated MD simulation of SAM formation was reported by Weigel et al. in 1980 of a lipid monolayer that displayed a first order phase transition from an ordered fluid state to a disordered gas state [422]. Shortly after this report appeared van der Ploeg and Berdensen presented a representation of a lipid bilayer serving as a model for a biological membrane that includes Lennard-Jones, dihedral, and bond angle interaction potentials while constraining bond lengths [423].

In 1988 Harris and Rice carried out an MD study of the thermodynamics of a monomolecular film of pentadecanoic acid on water [424]. In this simulation, water is treated as a polarizable continuum and the pentadecanoic acid molecules are treated as chains of 15 pseudoatoms with internal bond constraints, angle bending and torsional intramolecular interactions, and Lennard-Jones atom-atom intermolecular interactions. The results from these simulations exhibit low pressure phases in temp range of 300–400 K, low density vapor phase and well ordered condensed phase in sharp contrast with experimental studies which show existence of a stable liquid-expanded phase. At the time of this study, an understanding of the relationships between molecular conformation, intermolecular interaction, and the structures of the monolayer or multilayer systems was incomplete.

8.2 Models of SAMs on surfaces

The first attempt at a molecular description of the structure and dynamics of a SAM formed from alkane thiols on a metal surface was carried out by Hautman and Klien in 1989 [425]. Adsorption processes of long-chain alkyl thiol molecules on gold surfaces were not well understood at the time. MD simulations were used to investigate the structure and dynamics of monolayers of long-chain molecules on a metallic substrate. Two models were explored as alternative representations of the admolecule-surface interaction in layers formed by self-assembly of $HS(CH_2)_{15}CH_3$ molecules onto a gold substrate [425]. One model required that the S-C bond lies nearly parallel to the substrate surface. After long MD simulation equilibration at room temperature both models yielded monolayers with chains aligned with one another and tilted with respect to the surface normal. The two models resulted in different tilt angles. Despite this difference in tilt angle, the thickness of the two modeled monolayers is the same and the influence of the modified head-group on the detailed structure of the film is confined to the region closest to the metal surface. Notably the two models showed remarkable differences in the chain rotational dynamics.

In 1993, new force field parameters were derived to model the binding of alkane thiolates on gold and silver surfaces from ab initio calculations [426]. The first molecular mechanics (MM) energy minimization using these new force field parameters were presented. Ab initio geometry optimizations of HS and CH_3S on cluster models of Au(111), Au(100), Ag(111), and Ag(100) surfaces were performed at the RECP Hartree-Fock (HF) + electron correlation (MBPT2) level. Using these calculations, MD force field parameters were determined. The results of these

calculations show that there are two chemisorption modes that are very close in energy for thiolates on Au(111) surfaces. In the first chemisorption mode, the surface-S-C angle is ~180° due to sp hybridization. The second mode shows a surface-S-C angle of ~104° due to sp3 hybridization). These modes reveal a possible mechanism for the annealing of alkane thiol monolayers.

8.3 Terminal group effects

In the late 1980's n-alkane thiol SAMs began to be more widely examined experimentally as model systems to explore relationships between molecular structures, surfaces and surface properties [261–268,427–430]. Despite several studies of n-alkane thiols on Au(111) using a variety of techniques such as atomic force microscopy, scanning tunneling microscopy, FTIR, SERS, X-ray, diffraction of electrons and helium atoms, the packing structures and the chemisorption mode of alkane thiols remained ambiguous [331,431–443].

To address questions regarding the experimentally observed odd-even effect, computational studies including geometry optimizations and MD simulations were performed for self-assembled monolayers of n-alkane thiols (RSH) and 4′-alkoxybiphenyl-4-thiols ($ROC_{12}H_8SH$), where R=$C_{16}H_{33}$,$C_{17}H_{35}$ on a Au(111) surface using a full atomic representation force field by Li and Tao in 1998 [444]. These MD simulations explain origins of different odd-even effects observed by IR for long chain n-alkane thiols and 4′-alkoxybiphenyl-4-thiols and established a relationship between chemical structures of the head groups and packing structures of thiols on Au(111).

Modeling the properties of carboxylic acid terminated-SAMs was performed in 2005 by Harding et al. [415]. The motivation for this study was to address experimental work that showed that the length of a chain (odd or even number of carbon atoms) of long-chain carboxylic acid monolayers determined whether oriented growth is observed [324,331,445, 446]. MD simulations were used to investigate the confirmation of head groups of both odd and even number of carbon atoms of the chains. From the simulations it was determined that there were differences in the head group packing structure for odd and even length chains at 300 K in the presence of water.

In 2005 Goddard et al. performed a computational study on charge transport characteristics of biphenyldithiol (BPDT) SAMs in molecular electronic devices [447]. They identified an energetically favorable herringbone-type SAM packing configuration of the BPDT monolayer from force-field MD and annealing simulations. Three molecular electronic device models differing in packing orientation and tilt angle were developed for comparison. The coherent charge transport properties were calculated using a Green's function approach. Current – voltage curves were generated using a Landauer-Büttiker formula.

From these curves it was found that at low-bias voltages the i-V characteristics of a herringbone SAM with a 30° tilt angle and a parallel-oriented SAM with a 30° tilt are similar. The current for the herringbone SAM model with a 15° tilt angle is smaller than for either the herringbone model with a 30° tilt angle or the parallel structure model with 30° tilt angle. For the high-bias region i-V characteristics of all three models show noticeable differences due to phenyl band structures. They conclude that i-V characteristics of the BPDT SAM in the low-bias voltage region are mostly determined by the molecular junction properties, or the Si-Au interaction with the individual molecule-electrode contacts. At the high-bias region both intermolecular conformation and interactions can affect the BPDT SAM i-V characteristics.

Experimentally, it has been shown that OEG (oligo(ethylene glycol))-terminated alkane thiol monolayers resist protein adsorption [448]. However, a detailed study of the OEG structure

shows that only the helical conformation resists protein adsorption, whereas the more densely packed planar phases are less resistant to protein adsorption [449].

To understand how structural modifications of the SAM effect resistance to protein absorption, Grunze et al. performed ab initio HF calculations to explain the difference in protein absorption properties between the OEG groups in a 7/2 helical conformation (helical-SAM) and planar all-trans conformation on Ag (trans-SAM) [450]. For this study, the water near the SAM surface was modeled with small clusters comprising 20 water molecules and up to 12 rigid OEG strands packed hexagonally. The calculations showed that a single helical OEG strand was capable of forming strong hydrogen bonds with a water molecule bridging two successive oxygen atoms of the OEG strand. The planar all-trans conformation allowed only the formation of a single hydrogen bond involving one OEG oxygen atom and one water hydrogen atom.

The trans-SAM model was unable to form hydrogen bonds with water, except for weak C-H···O bonds with terminal methyl hydrogens. The densely packed rigid trans-SAM structure did not allow water molecules to penetrate into the SAM to reach the oxygen atoms of the ethylene glycol unit second from the surface, thus sacrificing the ability to form bridging hydrogen bonds with water as observed in the helical-SAM model. The authors speculate that bridging hydrogen bonds may be formed in less dense regions of the helical-SAM near defect sites.

In contrast to the ab initio HF calculations that used a rigid model, a MC simulation of water near the surface of flexible OEG-terminated SAMs was undertaken [418]. The simulation was carried out using a TIP4P model of water near the surface of an OEG-terminated alkane thiol SAM. The simulation of the behavior of water near the helical- and trans- OEG-terminated alkane thiol SAM has revealed a short-range effect of the SAM on the structure of the adjacent water layers.

Water molecules were able to penetrate deeper into the helical-SAM than the trans-SAM and formed more hydrogen bonds. Further, in agreement with experimental results, the presence of water has a disordering affect on the OEG groups. The adsorption of a protein molecule onto an OEG-SAM surface is presumed to involve displacement of water molecules from the surface, therefore, the SAM with a higher surface density of water molecules and hydrogen bonds should be more resistant to protein adsorption.

MD and electrochemical investigations of a pH responsive peptide monolayer have been reported [360]. The secondary structure of the peptide sequence HELELELELELC was studied using MD at 2 different pH values, 2 and 7. The results of the MD show that at pH = 2 the alpha helix conformation is stable for over 200 ns. At pH 7, a random coil is irreversibly obtained after 70 ns due to electrostatic repulsions between negatively charged carboxylate groups of the glutamic acid residues. The authors used this information to guide experiments in which the effect of pH on the ET properties of the peptide monolayers was examined (Section 6.4).

8.4 Ferrocene

Molecular dynamics simulations of mixed monolayers consisting of $Fc(CH_2)_{12}S$-/$C_{10}S$-Au SAMs have been carried out [451]. Simulations were performed to calculate both structural and energetic properties in order to explore the possible inhomogeneity of the neutral ferrocene moieties within the monolayer. Structural inhomogeneity has been implicated as the cause of non-ideal electrochemical responses [288].

Five systems were studied using different grafting densities for the ferrocenyl alkane thiols. The angular distributions were described in terms of the relative contributions from isolated

and clustered ferrocene moieties in the binary SAMs. The ferrocene groups prefer hydrophobic interactions with the alkane chains rather than hydrophilic interactions in the interfacial region. It was shown that the energetic contributions from each interaction (Fc-Fc, Fc-alkane, Fc-H_2O) strongly depend on whether the ferrocene is in an isolated or clustered state.

8.5 Silicon surfaces

SAMs on silicon have recently attracted interest for application of these layers in semiconductor technology. A molecular modeling study of covalently attached monolayers on a hydrogen terminated Si(111) surface was performed by Sudhölter et al. in 2001 [419]. Octadecyl monolayers on the H-terminated Si(111) surface were investigated using MD simulations with substitution percentages of the Si-H moieties by Si- alkyl groups ranging from 33 – 100%. The potential application of employing covalently bound organic monolayers on silicon surfaces in semiconductor technology was the motivation for this research.

In modeling monolayer-modified surfaces, periodic boundary conditions may or may not be included. The latter approach that does not include periodic boundary conditions and edge effects may be significant when using small surfaces. However, these effects may disappear upon an increase in surface size. Calculations on finite surfaces without periodic boundary conditions showed that all surfaces display edge effects where molecules on one edge of the surface are slightly tilted, whereas the other edge has molecules with a tilt angle that is much larger (both edges are in reference to molecules in the middle of the structure). The edge effects decrease with an increase in surface size. The average energy per alkyl chain in these structures has a dependence on the finite surface size and the energy values are considerably higher than that of analogous periodic box simulations.

The difference is attributed to a much smaller contribution from mutual van der Waal forces that are not properly accounted for on finite surfaces. Similar simulations with periodic boundary conditions did not show these edge effect complications and the optimal number of alkyl chains per simulation box is ~ 30. Simulations with fewer alkyl chains per simulation box showed that the results depend strongly on the size of the box. Calculations exploring substitution percentages of the Si-H for Si-alkyl groups on the monolayer structure show that only a substitution percentage of 50% gives satisfactory agreement with available experimental data.

9 Conclusions

Current work in long range biological electron transfer, artificial photosynthesis, and molecular electronics continues to draw on electrochemical studies of redox-modified SAMs. Molecular components such as switches, rectifiers, and transistors for nanomanufacturing of electronic devices incorporating SAMs are characterized by their ET properties.

The nature of the bridge between donor and acceptor is an active area of study. Electrochemical SAM studies continue to provide information regarding the effects of the bridge and the molecular environment on electron transfer [73,86]. A significant amount of work is directed towards developing new molecular junctions such as peptides [452–454]. Electrochemical SAM studies have allowed the direct comparison of photoinduced electron transfer (transient emission spectroscopy) to ground state electron transfer [155,455].

The electrochemical methods and surface chemistry described in this review allow researchers to determine specific electron transfer parameters. However, the myriad of electrochemical variables and sensitivity of the techniques, along with the mathematical analysis can be overwhelming. We have attempted to assemble descriptions of each of the electrochemical methods and the corresponding data analysis in order to make these methods more accessible

to the general readership. The literature illustrates that the nature of the redox active species and the SAM structure are critical to the accurate determination of k_{ET}. We have described how electrochemical methods can be used to evaluate these aspects. The history of computational modeling of SAMs closely parallels experimental work. It is our hope that this review will assist researchers in deciding which electrochemical technique best suits their purposes. Future work will undoubtedly explore the correlation of structural features of redox active SAMs, both covalent and noncovalent, to electron transfer parameters.

Table of Abbreviations

4-AMP	4-aminomethylpyridine
A	preintegral factor
A	ampere
A	adenine
AC	alternating current
AFM	atomic force microscopy
A_{SUR}	surface area
BPDT	biphenyldithiol
bpe	bipyridyl ethylene
bpy	bipyridine
C	capacitance
C	cytosine
C	coulomb
C_{60}	Buckminster fullerene
C_{AD}	adsorption pseudocapacitance
C_{DL}	double layer capacitance
Cp	cyclopentadienyl
CPE	constant phase element
CV	cyclic voltammetry
Cys	cysteine
cyt	cytochrome
d	distance
ds	double-stranded
dipy	4,4'-trimethylenedipyridine
DNA	deoxyribonucleic acid
DOS	density of states
$D_{ox}(\varepsilon)$	distribution of electron acceptor levels of the redox center
DPN	dip-pen nanolithography
dppm	1,1-bis(diphenylphosphino)methane
e	amount of charge transferred electron

E	redox potential
E_{pa}	anodic peak potential
E_{pc}	cathodic peak potential
E^0	redox potential at standard conditions
$E^{0'}$	formal potential
ΔE_p	potential separation of anodic and cathodic peaks
$\dot{E}$	potential (voltage) phasor
e_0	charge on an electron
EIS	electrochemical impedance spectroscopy
eSAM	electroactive self assembled monolayer
ET	electron transfer
F	Faraday constant
F	farad
f(ε)	Fermi function of metal
Fc	ferrocene
FcNB	ferrocene-terminated polynorbornyl
FTIR	Fourier transform infrared spectroscopy
FWHM	full width at half maximum
G	guanine
ΔG	Gibbs free energy
$\Delta G^{\ddagger}$	Gibbs energy of activation
Gly	glycine
h	Planck's constant
H_{AB}	electronic coupling
HF	Hartree-Fock
His	histidine
i	current
i_b	Background current
i_{ch}	charging current
i_f	faradaic current
i_p	peak current
i_T	total current
IAD	ITO ion-assisted deposition indium tin oxide
ITO	indium tin oxide
j	imaginary number, $(-1)^{1/2}$
K	equilibrium constant

k_{APP}	apparent rate constant
k_B	Boltzmann's constant
k_{ET}	standard, heterogeneous rate constant for electron transfer
k_{ox}	rate constant for oxidative electron transfer (ET from the electrode)
k_{red}	rate constant for reductive electron transfer (ET to the electrode)
k_s	rate constant for electron transfer at a particular overpotential
MC	Monte Carlo
MD	molecular dynamics
Me	methyl
MeNQ	2-methyl-1,4-naphthoquinone
Met	methionine
MM	molecular mechanics
MUA	mercaptoundecanoic acid
n	number of moles
N_A	Avogadro's number
OEG	oligo(ethylene glycol)
OMe	methoxy
OMe-bpy	4,4'-dimethoxy-2,2'-bipyridine
OPE	oligo(phenyleneethynylene)
OPV	oligo(phenylenevinylene)
P	proton
PBC	periodic boundary conditions
PCET	proton-coupled electron transfer
PGE	pyrolytic graphite “edge” electrode
PM-IRRAS	polarization modulation-infrared reflection-adsorption spectroscopy
PNA	peptide nucleic acid
p2p	1,2-bis(4-pyridyl)ethane
p3p	4,4'-trimethylenepyridine
PT	proton transfer
Py	pyridine
Q	charge
Q_T	total charge
R	ideal gas constant
r_0	electrode radius
r_A	radius of redox center A
r_B	radius of redox center B

RAIRS	reflection absorption infrared spectroscopy
R_{CT}	charge transfer resistance
R_{CT}^0	charge transfer resistance of a bare electrode
RSH	n-alkane thiol
R_{SOL}	uncompensated solution resistance
S	siemen
SAM	self assembled monolayer
SECM	scanning electrochemical microscopy
SEIRA	surface enhanced infrared absorption spectroscopy
SERRS	surface enhanced resonance Raman scattering
SOD	superoxide dismutase
ss	single-stranded
STM	scanning tunneling microscopy
t	time
T	temperature
T	thymine
TBTA	tris(benzyltriazolylmethyl)amine
TEMPO	2,2,6,6-tetramethylpiperidine-1-oxyl
terpy	terpyridine
Trp	tryptophan
V	volt
XPS	X-ray photoelectron spectroscopy
Z	impedance
Z_{Im}	imaginary component of impedance
Z_{Re}	real component of impedance
ZITO	zinc indium tin oxide
α	transfer coefficient
β	exponential tunneling decay factor
Γ	surface coverage
Γ_T	total surface coverage
ε	energy level relative to metal Fermi level
ε_{op}	optical dielectric constant
ε_F	Fermi level
ε_s	static dielectric constant
η	overpotential
θ	effective fractional surface coverage

κ	solution conductivity
λ	reorganization energy
λ_i	inner sphere reorganization energy
λ_o	outer sphere reorganization energy
ν	scan rate
$\rho(\varepsilon)$	density of states of metal
φ	phase angle
ω	angular frequency
ω_0	characteristic frequency
Ω	ohm

REFERENCES

[1]. Chidsey CED. Science 1991;251:919. [PubMed: 17847385]

[2]. Buriak JM. Chem. Commun 1999:1051.

[3]. Creager S, Yu CJ, Bamdad C, O'Connor S, MacLean T, Lam E, Chong Y, Olsen GT, Luo J, Gozin M, Kayyem JF. J. Am. Chem. Soc 1999;121:1059.

[4]. Diederich F, Gomez-Lopez M. Chem. Soc. Rev 1999;28:263.

[5]. Willner I, Katz E. Angew. Chem., Int. Ed. Engl 2000;39:1181.

[6]. Yu CJ, Wan Y, Yowanto H, Li J, Tao C, James MD, Tan CL, Blackburn GF, Meade TJ. J. Am. Chem. Soc 2001;123:11155. [PubMed: 11697958]

[7]. Bowler BE, Meade TJ, Mayo SL, Richards JH, Gray HB. J. Am. Chem. Soc 1989;111:8757.

[8]. Meade TJ, Gray HB, Winkler JR. J. Am. Chem. Soc 1989;111:4353.

[9]. Meade TJ, Kayyem JF. Angew. Chem., Int. Ed. Engl 1995;34:352.

[10]. Risser SM, Beratan DN, Meade TJ. J. Am. Chem. Soc 1993;115:2508.

[11]. Eckermann AL, Barker KD, Hartings MR, Ratner MA, Meade TJ. J. Am. Chem. Soc 2005;127:11880. [PubMed: 16117493]

[12]. Ye S, Zhou W, Abe M, Nishida T, Cui L, Uosaki K, Osawa M, Sasaki Y. J. Am. Chem. Soc 2004;126:7434. [PubMed: 15198578]

[13]. Shleev S, Tkac J, Christenson A, Ruzgas T, Yaropolov AI, Whittaker JW, Gorton L. Biosens. Bioelectron 2005;20:2517. [PubMed: 15854824]

[14]. Collier JH, Mrksich M. Proc. Natl. Acad. Sci. U. S. A 2006;103:2021. [PubMed: 16461913]

[15]. Bonifazi D, Enger O, Diederich F. Chem. Soc. Rev 2007;36:390. [PubMed: 17264939]

[16]. Trammell SA, Seferos DS, Moore M, Lowy DA, Bazan GC, Kushmerick JG, Lebedev N. Langmuir 2007;23:942. [PubMed: 17209656]

[17]. Abad JM, Gass M, Bleloch A, Schiffrin DJ. J. Am. Chem. Soc 2009;131:10229. [PubMed: 19583179]

[18]. Husken N, Gasser G, Koster SD, Metzler-Nolte N. Bioconj. Chem 2009;20:1578.

[19]. Barbara PF, Meyer TJ, Ratner MA. J. Phys. Chem 1996;100:13148.

[20]. Davis WB, Svec WA, Ratner MA, Wasielewski MR. Nature 1998;396:60.

[21]. DiBenedetto SA, Facchetti A, Ratner MA, Marks TJ. Adv. Mater. (Weinheim, Ger.) 2009;21:1407.

[22]. Mirkin CA, Ratner MA. Annu. Rev. Phys. Chem 1992;43:719.

[23]. Tsoi S, Griva I, Trammell SA, Blum AS, Schnur JM, Lebedev N. ACS Nano 2008;2:1289. [PubMed: 19206347]

[24]. Marcus RA. Advances in Chemistry Series 1965;50:138.

[25]. D'Alessandro DM, Keene FR. Chem. Soc. Rev 2006;35:424. [PubMed: 16636726]

[26]. D'Alessandro DM, Topley AC, Davies MS, Keene FR. Chem. Eur. J 2006;12:4873.
[27]. Beratan DN, Onuchic JN, Winkler JR, Gray HB. Science 1992;258:1740. [PubMed: 1334572]
[28]. Gray HB. Chem. Soc. Rev 1986;15:17.
[29]. Gray HB, Winkler JR. Annu. Rev. Biochem 1996;65:537. [PubMed: 8811189]
[30]. Gray HB, Winkler JR. Proc. Natl. Acad. Sci. U. S. A 2005;102:3534. [PubMed: 15738403]
[31]. Mayo SL, Ellis WR Jr. Crutchley RJ, Gray HB. Science 1986;233:948. [PubMed: 3016897]
[32]. Winkler JR, Di Bilio AJ, Farrow NA, Richards JH, Gray HB. Pure Appl. Chem 1999;71:1753.
[33]. Winkler JR, Gray HB, Prytkova TR, Kurnikov IV, Beratan DN. Bioelectronics 2005:15.
[34]. Imahori H, Kashiwagi Y, Hasobe T, Kimura M, Hanada T, Nishimura Y, Yamazaki I, Araki Y, Ito O, Fukuzumi S. Thin Solid Films 2004;451–452:580.
[35]. Bertin PA, Georganopoulou D, Liang T, Eckermann AL, Wunder M, Ahrens MJ, Blackburn GF, Meade TJ. Langmuir 2008;24:9096. [PubMed: 18627193]
[36]. Trammell SA, Moore M, Lowy D, Lebedev N. J. Am. Chem. Soc 2008;130:5579. [PubMed: 18373346]
[37]. Chidsey CED, Loiacono DN. Langmuir 1990;6:682.
[38]. Miller C, Cuendet P, Graetzel M. J. Phys. Chem 1991;95:877.
[39]. Miller C, Graetzel M. J. Phys. Chem 1991;95:5225.
[40]. Naleway CA, Curtiss LA, Miller JR. J. Phys. Chem 1991;95:8434.
[41]. Becka AM, Miller CJ. J. Phys. Chem 1992;96:2657.
[42]. Finklea HO, Hanshew DD. J. Am. Chem. Soc 1992;114:3173.
[43]. Becka AM, Miller CJ. J. Phys. Chem 1993;97:6233.
[44]. Sikes HD, Smalley JF, Dudek SP, Cook AR, Newton MD, Chidsey CED, Feldberg SW. Science 2001;291:1519. [PubMed: 11222852]
[45]. Smalley JF, Finklea HO, Chidsey CED, Linford MR, Creager SE, Ferraris JP, Chalfant K, Zawodzinsk T, Feldberg SW, Newton MD. J. Am. Chem. Soc 2003;125:2004. [PubMed: 12580629]
[46]. Bard, AJ.; Faulkner, Larry R. Electrochemical Methods: Fundamentals and Applications. 2nd ed.. John Wiley & Sons, Inc.; New York: 2001.
[47]. Queiroz SL, De Araujo MP, Batista AA, MacFarlane KS, James BR. J. Chem. Ed 2001;78:89.
[48]. Evans DH, O'Connell KM, Petersen RA, Kelly MJ. J. Chem. Ed 1983;60:290.
[49]. Kissinger PT, Heineman WR. J. Chem. Ed 1983;60:702.
[50]. Van Benschoten JJ, Lewis JY, Heineman WR, Roston DA, Kissinger PT. J. Chem. Ed 1983;60:772.
[51]. Brown AP, Anson FC. Anal. Chem 1977;49:1589.
[52]. Laviron E. J. Electroanal. Chem. Interfacial Electrochem 1979;100:263.
[53]. Finklea HO. Electroanalytical Chemistry 1996;19:109.
[54]. Laviron E. J. Electroanal. Chem. Interfacial Electrochem 1979;101:19.
[55]. Hartnig C, Koper MTM. J Chem Phys 2001;115:8540.
[56]. Smalley JF, Feldberg SW, Chidsey CED, Linford MR, Newton MD, Liu Y-P. J. Phys. Chem 1995;99:13141.
[57]. Smalley JF, Sachs SB, Chidsey CED, Dudek SP, Sikes HD, Creager SE, Yu CJ, Feldberg SW, Newton MD. J. Am. Chem. Soc 2004;126:14620. [PubMed: 15521782]
[58]. Marcus RA. J. Chem. Phys 1956;24:979.
[59]. Marcus RA. J. Chem. Phys 1956;24:966.
[60]. Marcus RA. Annual Review Physical Chemistry 1964;15:155.
[61]. Marcus RA, Sutin N. Biochimica et Biophysica Acta 1985;811:265.
[62]. Closs GL, Miller JR. Science 1988;240:440. [PubMed: 17784065]
[63]. Sutin N, Brunschwig BS, Creutz C, Winkler JR. Pure App. Chem 1988;60:1817.
[64]. Marcus RA. J.Phys. Chem. A 1989;93:3078.
[65]. Chen P, Duesing R, Graff DK, Meyer TJ. J. Phys. Chem 1991;95:5850.
[66]. Chen P, Meyer TJ. Chem. Rev 1998;98:1439. [PubMed: 11848939]
[67]. Huynh MHV, Meyer TJ. Chem. Rev 2007;107:5004. [PubMed: 17999556]

[68]. Schmickler, W. Interfacial Electrochemistry. Oxford University Press; 1996.
[69]. Tender L, Carter MT, Murray RW. Anal. Chem 1994;66:3173.
[70]. Weber K, Creager SE. Anal. Chem 1994;66:3164.
[71]. Kittel, C. Introduction to Solid State Physics. 4th Edition ed.. John Wiley & Sons; 1971.
[72]. Smalley JF. J. Phys. Chem. B 2007;111:6798. [PubMed: 17391021]
[73]. Eggers PK, Hibbert DB, Paddon-Row MN, Gooding JJ. J. Phys. Chem. C 2009;113:8964.
[74]. Ravenscroft MS, Finklea HO. J. Phys. Chem 1994;98:3843.
[75]. Rowe GK, Carter MT, Richardson JN, Murray RW. Langmuir 1995;11:1797.
[76]. Finklea HO, Liu L, Ravenscroft MS, Punturi S. Journal of Physical Chemistry 1996;100:18852.
[77]. Creager SE, Wooster TT. Analytical Chemistry 1998;70:4257.
[78]. Arikuma Y, Takeda K, Morita T, Ohmae M, Kimura S. J. Phys. Chem. B 2009;113:6256. [PubMed: 19361180]
[79]. Okamoto S, Morita T, Kimura S. Langmuir 2009;25:3297. [PubMed: 19437730]
[80]. Takeda K, Morita T, Kimura S. J. Phys. Chem. B 2008;112:12840. [PubMed: 18793017]
[81]. Brevnov DA, Finklea HO, Van Ryswyk H. J. Electroanal. Chem 2001;500:100.
[82]. Sumner JJ, Creager SE. J. Am. Chem. Soc 2000;122:11914.
[83]. Sumner JJ, Creager SE. J. Phys. Chem. B 2001;105:8739.
[84]. Sumner JJ, Weber KS, Hockett LA, Creager SE. J. Phys. Chem. B 2000;104:7449.
[85]. Eckermann AL, Shaw JA, Meade TJ. Langmuir. 2009 ACS ASAP.
[86]. Eggers PK, Zareie HM, Paddon-Row MN, Gooding JJ. Langmuir 2009;25:11090. [PubMed: 19459588]
[87]. Fabre B, Hauquier F. J. Phys. Chem. B 2006;110:6848. [PubMed: 16570994]
[88]. Hortholary C, Minc F, Coudret C, Bonvoisin J, Launay J-P. Chem. Commun 2002:1932.
[89]. Nahir TM, Bowden EF. Langmuir 2002;18:5283.
[90]. Li J, Schuler K, Creager SE. J. Electrochem. Soc 2000;147:4584.
[91]. Katz E, Willner I. Electroanalysis (New York) 2003;15:913.
[92]. Garcia-Jareno JJ, Benito D, Sanmatias A, Vicente F. J. Chem. Ed 2000;77:738.
[93]. Park S-M, Yoo J-S. Anal. Chem 2003;75:455A.
[94]. Macdonald DD. Electrochimica Acta 2006;51:1376.
[95]. Laviron E. J. Electroanal. Chem. Interfacial Electrochem 1979;97:135.
[96]. Laviron E. J. Electroanal. Chem. Interfacial Electrochem 1979;105:25.
[97]. Laviron E. J. Electroanal. Chem. Interfacial Electrochem 1979;105:35.
[98]. Abhayawardhana AD, Sutherland TC. J. Phys. Chem. C 2009;113:4915.
[99]. Brug GJ, Van den Eeden ALG, Sluyters-Rehbach M, Sluyters JH. J. Electroanal. Chem. Interfacial Electrochem 1984;176:275.
[100]. Nahir TM, Bowden EF. J. Electroanal. Chem 1996;410:9.
[101]. Jorcin J-B, Orazem ME, Pebere N, Tribollet B. Electrochimica Acta 2006;51:1473.
[102]. Kiani A, Alpuche-Aviles MA, Eggers PK, Jones M, Gooding JJ, Paddon-Row MN, Bard AJ. Langmuir 2008;24:2841. [PubMed: 18237208]
[103]. Yamada H, Ogata M, Koike T. Langmuir 2006;22:7923. [PubMed: 16922585]
[104]. Liu B, Bard AJ, Mirkin MV, Creager SE. J. Am. Chem. Soc 2004;126:1485. [PubMed: 14759206]
[105]. Holt KB. Langmuir 2006;22:4298. [PubMed: 16618178]
[106]. Edwards PP, Gray HB, Lodge MTJ, Williams RJP. Angew. Chem., Int. Ed. Engl 2008;47:6758. [PubMed: 18651676]
[107]. Kealy TJ, Pauson PL. Nature 1951;168:1039.
[108]. Wilkinson G, Rosenblum M, Whiting MC, Woodward RB. J. Am. Chem. Soc 1952;74:2125.
[109]. Pfab W, Fischer EO. Z. Anorg. Allg. Chem 1953;274:316.
[110]. Page JA, Wilkinson G. J. Am. Chem. Soc 1952;74:6149.
[111]. Zanello P. Ferrocenes 1995:317.

[112]. Nguyen P, Gomez-Elipe P, Manners I. Chem. Rev 1999;99:1515. [PubMed: 11849001]
[113]. Colacot TJ. Chem. Rev 2003;103:3101. [PubMed: 12914493]
[114]. Osakada K, Sakano T, Horie M, Suzaki Y. Coord. Chem. Rev 2006;250:1012.
[115]. Hirao T. J. Organomet. Chem 2009;694:806.
[116]. Nijhuis CA, Ravoo BJ, Huskens J, Reinhoudt DN. Coord. Chem. Rev 2007;251:1761.
[117]. Bonini BF, Fochi M, Ricci A. Synlett 2007:360.
[118]. Wagner M. Angew. Chem., Int. Ed. Engl 2006;45:5916. [PubMed: 16906602]
[119]. Siemeling U. Z. Anorg. Allg. Chem 2005;631:2957.
[120]. Nakamura E. J. Organomet. Chem 2004;689:4630.
[121]. Beer PD, Hayes EJ. Coord. Chem. Rev 2003;240:167.
[122]. Mathey F. J. Organomet. Chem 2002;646:15.
[123]. Hudson RDA. J. Organomet. Chem 2001;637–639:47. [PubMed: 19594449]
[124]. Balavoine GGA, Daran JC, Iftime G, Manoury E, Moreau-Bossuet C. J. Organomet. Chem 1998;567:191.
[125]. Herrmann R, Huebener G, Ugi I. Tetrahedron 1985;41:941.
[126]. Marquarding D, Klusacek H, Gokel G, Hoffmann P, Ugi I. J. Amer. Chem. Soc 1970;92:5389.
[127]. Collman JP, Devaraj NK, Chidsey CED. Langmuir 2004;20:1051. [PubMed: 15803676]
[128]. Collman JP, Devaraj NK, Eberspacher TPA, Chidsey CED. Langmuir 2006;22:2457. [PubMed: 16519441]
[129]. Plumb K, Kraatz H-B. Bioconjugate Chem 2003;14:601.
[130]. Nomoto A, Moriuchi T, Yamazaki S, Ogawa A, Hirao T. Chem. Commun 1998:1963.
[131]. Maricic S, Frejd T. J. Org. Chem 2002;67:7600. [PubMed: 12398478]
[132]. Hess A, Brosch O, Weyhermuller T, Metzler-Nolte N. J. Organomet. Chem 1999;589:75.
[133]. Eckert H, Koller M. Z. Naturforsch., B: Chem. Sci 1990;45:1709.
[134]. Brosch O, Weyhermueller T, Metzler-Nolte N. Inorg. Chem 1999;38:5308.
[135]. Paul A, Watson RM, Lund P, Xing Y, Burke K, He Y, Borguet E, Achim C, Waldeck DH. J. Phys. Chem. C 2008;112:7233.
[136]. Paul A, Bezer S, Venkatramani R, Kocsis L, Wierzbinski E, Balaeff A, Keinan S, Beratan DN, Achim C, Waldeck DH. J. Am. Chem. Soc 2009;131:6498. [PubMed: 19382798]
[137]. Baldoli C, Licandro E, Maiorana S, Resemini D, Rigamonti C, Falciola L, Longhi M, Mussini PR. J. Electroanal. Chem 2005;585:197.
[138]. Yu CJ, Yowanto H, Wan Y, Meade TJ, Chong Y, Strong M, Donilon LH, Kayyem JF, Gozin M, Blackburn GF. J. Am. Chem. Soc 2000;122:6767.
[139]. Pike AR, Ryder LC, Horrocks BR, Clegg W, Connolly BA, Houlton A. Chem.--Eur. J 2005;11:344.
[140]. Bertin PA, Meade TJ. Tetrahedron Lett 2009;50:5409.
[141]. Stynes HC, Ibers JA. Inorg. Chem 1971;10:2304.
[142]. Endicott JF, Taube H. Inorg. Chem 1965;4:437.
[143]. Ghosh BK, Chakravorty A. Coord. Chem. Rev 1989;95:239.
[144]. Allen AD, Senoff CW. Chem. Commun 1965:621.
[145]. Harrison DE, Taube H. J. Am. Chem. Soc 1967;89:5706.
[146]. Creutz C, Taube H. J. Am. Chem. Soc 1973;95:1086.
[147]. Ford PC, Rudd DP, Gaunder R, Taube H. J. Am. Chem. Soc 1968;90:1187.
[148]. Matsubara T, Ford PC. Inorg. Chem 1976;15:1107.
[149]. Shin, Y.-g. K.; Szalda, DJ.; Brunschwig, BS.; Creutz, C.; Sutin, N. Inorg. Chem 1997;36:3190. [PubMed: 11669976]
[150]. Isied SS, Taube H. Inorg. Chem 1976;15:3070.
[151]. Marchant JA, Matsubara T, Ford PC. Inorg. Chem 1977;16:2160.
[152]. Che CM, Yam VWW. Advances in Inorganic Chemistry 1992;39:233.
[153]. Lay PA, Harman WD. Advances in Inorganic Chemistry 1991;37:219.
[154]. Forster RJ, Faulkner LR. J. Am. Chem. Soc 1994;116:5453.

[155]. Forster RJ, Keyes TE. J. Phys. Chem. B 2001;105:8829.

[156]. Forster RJ, O'Kelly JP. J. Phys. Chem 1996;100:3695.

[157]. Haddox RM, Finklea HO. J. Phys. Chem. B 2004;108:1694.

[158]. Echegoyen L, Echegoyen LE. Acc. Chem. Res 1998;31:593.

[159]. Yang Y, Arias F, Echegoyen L, Chibante LPF, Flanagan S, Robertson A, Wilson LJ. J. Am. Chem. Soc 1995;117:7801.

[160]. Suzuki T, Maruyama Y, Akasaka T, Ando W, Kobayashi K, Nagase S. J. Am. Chem. Soc 1994;116:359.

[161]. Xie Q, Perez-Cordero E, Echegoyen L. J. Am. Chem. Soc 1992;114:3978.

[162]. Fukuzumi S, Nakanishi I, Suenobu T, Kadish KM. J. Am. Chem. Soc 1999;121:3468.

[163]. Larsson S, Klimkans A, Rodriguez-Monge L, Duskesas G. Theochem 1998;425:155.

[164]. Imahori H, Sakata Y. Adv. Mater. (Weinheim, Ger.) 1997;9:537.

[165]. Imahori H, Yamada H, Nishimura Y, Yamazaki I, Sakata Y. J. Phys. Chem. B 2000;104:2099.

[166]. Guldi DM. Chemical Society Reviews 2002;31:22. [PubMed: 12108980]

[167]. Yamada H, Imahori H, Fukuzumi S. J. Mater. Chem 2002;12:2034.

[168]. Yamada H, Imahori H, Nishimura Y, Yamazaki I, Fukuzumi S. Adv. Mater. (Weinheim, Ger.) 2002;14:892.

[169]. Yamada H, Imahori H, Nishimura Y, Yamazaki I, Ahn TK, Kim SK, Kim D, Fukuzumi S. J. Am. Chem. Soc 2003;125:9129. [PubMed: 15369370]

[170]. Cho Y-J, Ahn TK, Song H, Kim KS, Lee CY, Seo WS, Lee K, Kim SK, Kim D, Park JT. J. Am. Chem. Soc 2005;127:2380. [PubMed: 15724978]

[171]. Chukharev V, Vuorinen T, Efimov A, Tkachenko NV, Kimura M, Fukuzumi S, Imahori H, Lemmetyinen H. Langmuir 2005;21:6385. [PubMed: 15982045]

[172]. Isosomppi M, Tkachenko NV, Efimov A, Kaunisto K, Hosomizu K, Imahori H, Lemmetyinen H. J. Mater. Chem 2005;15:4546.

[173]. Caldwell WB, Chen K, Mirkin CA, Babinec SJ. Langmuir 1993;9:1945.

[174]. Chen K, Caldwell WB, Mirkin CA. J. Am. Chem. Soc 1993;115:1193.

[175]. Song F, Zhang S, Bonifazi D, Enger O, Diederich F, Echegoyen L. Langmuir 2005;21:9246. [PubMed: 16171358]

[176]. Arias F, Godinez LA, Wilson SR, Kaifer AE, Echegoyen L. J. Am. Chem. Soc 1996;118:6086.

[177]. Dominguez O, Echegoyen L, Cunha F, Tao N. Langmuir 1998;14:821.

[178]. Shi X, Caldwell WB, Chen K, Mirkin CA. J. Am. Chem. Soc 1994;116:11598.

[179]. Vuorimaa E, Vuorinen T, Tkachenko N, Cramariuc O, Hukka T, Nummelin S, Shivanyuk A, Rissanen K, Lemmetyinen H. Langmuir 2001;17:7327.

[180]. Fukuzumi S, Honda T, Ohkubo K, Kojima T. Dalton Trans 2009:3880. [PubMed: 19440585]

[181]. Guldi DM, Illescas BM, Atienza CM, Wielopolski M, Martin N. Chemical Society Reviews 2009;38:1587. [PubMed: 19587954]

[182]. Sakata Y, Imahori H, Tsue H, Higashida S, Akiyama T, Yoshizawa E, Aoki M, Yamada K, Hagiwara K, Taniguchi S, Okada T. Pure Appl. Chem 1997;69:1951.

[183]. Marcus RA. Angew. Chem., Int. Ed. Engl 1993;32:1111.

[184]. Abe M, Michi T, Sato A, Kondo T, Zhou W, Ye S, Uosaki K, Sasaki Y. Angew. Chem., Int. Ed. Engl 2003;42:2912. [PubMed: 12833357]

[185]. Michi T, Abe M, Takakusagi S, Kato M, Uosaki K, Sasaki Y. Chemistry Letters 2008;37:576.

[186]. Uehara H, Inomata T, Abe M, Uosaki K, Sasaki Y. Chemistry Letters 2008;37:684.

[187]. Henderson JI, Feng S, Ferrence GM, Bein T, Kubiak CP. Inorg. Chim. Acta 1996;242:115.

[188]. Jensen PS, Chi Q, Grumsen FB, Abad JM, Horsewell A, Schiffrin DJ, Ulstrup J. J. Phys. Chem. C 2007;111:6124.

[189]. Shafiey H, Ghourchian H, Mogharrab N. Biophysical Chemistry 2008;134:225. [PubMed: 18325656]

[190]. Finklea HO, Madhiri N. J. Electroanal. Chem 2008;621:129.

[191]. Orlowski GA, Chowdhury S, Kraatz H-B. Langmuir 2007;23:12765. [PubMed: 17975937]

[192]. Madhiri N, Finklea HO. Langmuir 2006;22:10643. [PubMed: 17129042]
[193]. Blankman JI, Shahzad N, Miller CJ, Guiles RD. Biochemistry 2000;39:14806. [PubMed: 11101296]
[194]. Blankman JI, Shahzad N, Dangi B, Miller CJ, Guiles RD. Biochemistry 2000;39:14799. [PubMed: 11101295]
[195]. Weber KS, Creager SE. J. Electroanal. Chem 1998;458:17.
[196]. Creager SE, Weber K. Langmuir 1993;9:844.
[197]. Hammes-Schiffer S, Soudackov AV. J. Phys. Chem. B 2008;112:14108. [PubMed: 18842015]
[198]. Costentin C. Chem. Rev 2008;108:2145. [PubMed: 18620365]
[199]. Hammes-Schiffer S, Hatcher E, Ishikita H, Skone JH, Soudackov AV. Coordination Chemistry Reviews 2008;252:384.
[200]. Jones MR. Biochem. Soc. Trans 2009;37:400. [PubMed: 19290870]
[201]. Meyer TJ, Huynh MHV, Thorp HH. Angew. Chem., Int. Ed. Engl 2007;46:5284. [PubMed: 17604381]
[202]. Miller A-F. Acc. Chem. Res 2008;41:501. [PubMed: 18376853]
[203]. Reece SY, Nocera DG. Annu. Rev. Biochem 2009;78:673. [PubMed: 19344235]
[204]. Finklea HO, Haddox RM. Phys. Chem. Chem. Phys 2001;3:3431.
[205]. Haddox RM, Finklea HO. J. Electroanal. Chem 2003;550–551:351.
[206]. Niermann N, Degefa TH, Walder L, Zielke V, Steinhoff H-J, Onsgaard J, Speller S. Phys. Rev. B: Condens. Matter Mater. Phys 2006;74:235424/1.
[207]. Hammes-Schiffer S. Isot. Eff. Chem. Biol 2006:499.
[208]. Takeuchi KJ, Samuels GJ, Gersten SW, Gilbert JA, Meyer TJ. Inorg. Chem 1983;22:1407.
[209]. Takeuchi KJ, Thompson MS, Pipes DW, Meyer TJ. Inorg. Chem 1984;23:1845.
[210]. Costentin C, Robert M, Saveant J-M. J. Am. Chem. Soc 2007;129:5870. [PubMed: 17428051]
[211]. Costentin C, Robert M, Saveant J-M, Teillout A-L. ChemPhysChem 2009;10:191. [PubMed: 18816536]
[212]. Trammell SA, Lowy DA, Seferos DS, Moore M, Bazan GC, Lebedev N. J. Electroanal. Chem 2007;606:33.
[213]. Kazemekaite M, Bulovas A, Talaikyte Z, Butkus E, Railaite V, Niaura G, Palaima A, Razumas V. Tetrahedron Lett 2004;45:3551.
[214]. Gray HB, Winkler JR. Quarterly Reviews of Biophysics 2003;36:341. [PubMed: 15029828]
[215]. Nowak C, Luening C, Schach D, Baurecht D, Knoll W, Naumann RLC. J. Phys. Chem. C 2009;113:2256.
[216]. Collman JP, Decreau RA, Lin H, Hosseini A, Yang Y, Dey A, Eberspacher TA. Proc. Natl. Acad. Sci. U. S. A 2009;106:7320. [PubMed: 19380725]
[217]. Grochol J, Dronov R, Lisdat F, Hildebrandt P, Murgida DH. Langmuir 2007;23:11289. [PubMed: 17902715]
[218]. Alessandrini A, Facci P. Nano Mol. Electron. Handb 2007:14/1.
[219]. Millo D, Ranieri A, Koot W, Gooijer C, van der Zwan G. Anal. Chem 2006;78:5622. [PubMed: 16878907]
[220]. Fujita K, Nakamura N, Ohno H, Leigh BS, Niki K, Gray HB, Richards JH. J. Am. Chem. Soc 2004;126:13954. [PubMed: 15506756]
[221]. Wei J, Liu H, Dick AR, Yamamoto H, He Y, Waldeck DH. J. Am. Chem. Soc 2002;124:9591. [PubMed: 12167054]
[222]. Murgida DH, Hildebrandt P. J. Am. Chem. Soc 2001;123:4062. [PubMed: 11457157]
[223]. Clark RA, Bowden EF. Langmuir 1997;13:559.
[224]. Bjerrum MJ, Casimiro DR, Chang IJ, Di Bilio AJ, Gray HB, Hill MG, Langen R, Mines GA, Skov LK, Winkler JR, Wuttke DS. J. Bioenerg. Biomembr 1995;27:295. [PubMed: 8847343]
[225]. Nahir TM, Clark RA, Bowden EF. Anal. Chem 1994;66:2595.
[226]. Bowden EF, Clark RA, Willit JL, Song S. Proc. - Electrochem. Soc 1993;93–11:34.
[227]. Collinson M, Bowden EF, Tarlov MJ. Langmuir 1992;8:1247.

[228]. Bowden EF, Hawkridge FM, Chlebowski JF, Bancroft EE, Thorpe C, Blount HN. J. Am. Chem. Soc 1982;104:7641.

[229]. Cotton TM, Schultz SG, Van Duyne RP. J. Am. Chem. Soc 1980;102:7960.

[230]. Holwerda RA, Wherland S, Gray HB. Annu Rev Biophys Bioeng 1976;5:363. [PubMed: 821386]

[231]. Taniguchi I, Toyosawa K, Yamaguchi H, Yasukouchi K. J. Chem. Soc., Chem. Commun 1982:1032.

[232]. Song S, Clark RA, Bowden EF, Tarlov MJ. J. Phys. Chem 1993;97:6564.

[233]. Kasmi AE, Wallace JM, Bowden EF, Binet SM, Linderman RJ. J. Am. Chem. Soc 1998;120:225.

[234]. Murgida DH, Hildebrandt P. J. Phys. Chem. B 2001;105:1578.

[235]. Murgida DH, Hildebrandt P. J. Phys. Chem. B 2002;106:12814.

[236]. Murgida DH, Hildebrandt P, Wei J, He YF, Liu H, Waldeck DH. J. Phys. Chem. B 2004;108:2261.

[237]. Wei J, Liu H, Khoshtariya DE, Yamamoto H, Dick A, Waldeck DH. Angew. Chem., Int. Ed. Engl 2002;41:4700. [PubMed: 12481331]

[238]. Yue H, Khoshtariya D, Waldeck DH, Grochol J, Hildebrandt P, Murgida DH. J. Phys. Chem. B 2006;110:19906. [PubMed: 17020376]

[239]. Millo D, Bonifacio A, Ranieri A, Borsari M, Gooijer C, Van der Zwan G. Langmuir 2007;23:9898. [PubMed: 17685564]

[240]. Millo D, Ranieri A, Gross P, Ly HK, Borsari M, Hildebrandt P, Wuite GJL, Gooijer C, van der Zwan G. J. Phys. Chem. C 2009;113:2861.

[241]. Wittung-Stafshede P. Inorg. Chem 2004;43:7926. [PubMed: 15578826]

[242]. Bonanni B, Alliata D, Andolfi L, Bizzarri AR, Cannistraro S. Surf. Sci. Res. Dev 2005:1.

[243]. Bollinger JM Jr. Science 2008;320:1730. [PubMed: 18583602]

[244]. Machczynski Michael C, Gray Harry B, Richards John H. J Inorg Biochem 2002;88:375. [PubMed: 11897353]

[245]. Gray HB, Coyle CL, Dooley DM, Grunthaner PJ, Hare JW, Holwerda RA, McArdle JV, McMillin DR, Rawlings J, et al. Adv. Chem. Ser 1977;162:145.

[246]. Winkler JR, Gray HB. J. Biol. Inorg. Chem 1997;2:399.

[247]. Gray HB, Malmstrom BG, Williams RJP. J.Biol. Inorg. Chem 2000;5:551. [PubMed: 11085645]

[248]. Miller JE, Di Bilio AJ, Wehbi WA, Green MT, Museth AK, Richards JR, Winkler JR, Gray HB. Biochim. Biophys. Acta, Bioenerg 2004;1655:59.

[249]. Jeuken LJC, Armstrong FA. J. Phys. Chem. B 2001;105:5271.

[250]. Chi Q, Zhang J, Andersen JET, Ulstrup J. J. Phys. Chem. B 2001;105:4669.

[251]. Jeuken LJC, McEvoy JP, Armstrong FA. J. Phys. Chem. B 2002;106:2304.

[252]. Yokoyama K, Leigh BS, Sheng Y, Niki K, Nakamura N, Ohno H, Winkler JR, Gray HB, Richards JH. Inorg. Chim. Acta 2008;361:1095.

[253]. Armstrong FA, Barlow NL, Burn PL, Hoke KR, Jeuken LJC, Shenton C, Webster GR. Chem. Commun 2004:316.

[254]. Sachs SB, Dudek SP, Hsung RP, Sita LR, Smalley JF, Newton MD, Feldberg SW, Chidsey CED. J. Am. Chem. Soc 1997;119:10563.

[255]. Guo Y, Zhao J, Yin X, Gao X, Tian Y. J. Phys. Chem. C 2008;112:6013.

[256]. Vargo ML, Gulka CP, Gerig JK, Manieri CM, Dattelbaum JD, Marks CB, Lawrence NT, Trawick ML, Leopold MC. Langmuir. 2009 ACS ASAP.

[257]. Tian Y, Mao L, Okajima T, Ohsaka T. Anal. Chem 2004;76:4162. [PubMed: 15253658]

[258]. Nuzzo RG, Allara DL. J. Am. Chem. Soc 1983;105:4481.

[259]. Nuzzo RG, Fusco FA, Allara DL. J. Am. Chem. Soc 1987;109:2358.

[260]. Porter MD, Bright TB, Allara DL, Chidsey CED. J. Am. Chem. Soc 1987;109:3559.

[261]. Bain CD, Whitesides GM. J. Am. Chem. Soc 1988;110:6560.

[262]. Bain CD, Whitesides GM. Science 1988;240:62. [PubMed: 17748822]

[263]. Bain CD, Whitesides GM. J. Am. Chem. Soc 1988;110:3665.

[264]. Bain CD, Biebuyck HA, Whitesides GM. Langmuir 1989;5:723.

[265]. Bain CD, Evall J, Whitesides GM. J. Am. Chem. Soc 1989;111:7155.

[266]. Bain CD, Troughton EB, Tao YT, Evall J, Whitesides GM, Nuzzo RG. J. Am. Chem. Soc 1989;111:321.

[267]. Bain CD, Whitesides GM. Langmuir 1989;5:1370.

[268]. Bain CD, Whitesides GM. J. Am. Chem. Soc 1989;111:7164.

[269]. Love JC, Estroff LA, Kriebel JK, Nuzzo RG, Whitesides GM. Chem. Rev 2005;105:1103. [PubMed: 15826011]

[270]. Poirier GE. Chem. Rev 1997;97:1117. [PubMed: 11851444]

[271]. Edinger K, Goelzhaeuser A, Demota K, Woell C, Grunze M. Langmuir 1993;9:4.

[272]. Kim YT, Bard AJ. Langmuir 1992;8:1096.

[273]. Benitez G, Vericat C, Tanco S, Lenicov FR, Castez MF, Vela ME, Salvarezza RC. Langmuir 2004;20:5030. [PubMed: 15984265]

[274]. Sondag-Huethorst JAM, Schonenberger C, Fokkink LGJ. J. Phys. Chem 1994;98:6826.

[275]. Sondag-Huethorst JAM, Fokkink LGJ. Langmuir 1994;10:4380.

[276]. Salmeron M, Neubauer G, Folch A, Tomitori M, Ogletree DF, Sautet P. Langmuir 1993;9:3600.

[277]. Hansma HG, Gould SAC, Hansma PK, Gaub HE, Longo ML, Zasadzinski JAN. Langmuir 1991;7:1051.

[278]. Demoz A, Harrison DJ. Langmuir 1993;9:1046.

[279]. Tao F, Bernasek SL. Chem. Rev 2007;107:1408. [PubMed: 17439290]

[280]. Poirier GE, Pylant ED. Science 1996;272:1145. [PubMed: 8662446]

[281]. Xu S, Cruchon-Dupeyrat SJN, Garno JC, Liu G-Y, Kane Jennings G, Yong T-H, Laibinis PE. J. Chem. Phys 1998;108:5002.

[282]. Chambers RC, Inman CE, Hutchison JE. Langmuir 2005;21:4615. [PubMed: 16032880]

[283]. Collard DM, Fox MA. Langmuir 1991;7:1192.

[284]. Zhao X-M, Wilbur JL, Whitesides GM. Langmuir 1996;12:3257.

[285]. Vericat C, Lenicov FR, Tanco S, Andreasen G, Vela ME, Salvarezza RC. J. Phys. Chem. B 2002;106:9114.

[286]. Vericat C, Vela ME, Salvarezza RC. Phys. Chem. Chem. Phys 2005;7:3258. [PubMed: 16240039]

[287]. Lee LYS, Lennox RB. Phys. Chem. Chem. Phys 2007;9:1013. [PubMed: 17301892]

[288]. Lee LYS, Sutherland TC, Rucareanu S, Lennox RB. Langmuir 2006;22:4438. [PubMed: 16618200]

[289]. Creager SE, Hockett LA, Rowe GK. Langmuir 1992;8:854.

[290]. Campbell DJ, Herr BR, Hulteen JC, Van Duyne RP, Mirkin CA. J. Am. Chem. Soc 1996;118:10211.

[291]. Herr BR, Mirkin CA. J. Am. Chem. Soc 1994;116:1157.

[292]. Li C, Ren B, Zhang Y, Cheng Z, Liu X, Tong Z. Langmuir 2008;24:12911. [PubMed: 18928307]

[293]. Namiki K, Sakamoto A, Murata M, Kume S, Nishihara H. Chem. Commun 2007:4650.

[294]. Calvente JJ, Lopez-Perez G, Ramirez P, Fernandez H, Zon MA, Mulder WH, Andreu R. J. Am. Chem. Soc 2005;127:6476. [PubMed: 15853356]

[295]. Calvente JJ, Andreu R, Molero M, Lopez-Perez G, Dominguez M. J. Phys. Chem. B 2001;105:9557.

[296]. Sabatani E, Rubinstein I. J. Phys. Chem 1987;91:6663.

[297]. Finklea HO, Hanshew DD. J. Electroanal. Chem 1993;347:327.

[298]. Hockett LA, Creager SE. Langmuir 1995;11:2318.

[299]. Weber K, Hockett L, Creager S. J. Phys. Chem. B 1997;101:8286.

[300]. Robinson DB, Chidsey CED. J. Phys. Chem. B 2002;106:10706.

[301]. Chidsey CED, Bertozzi CR, Putvinski TM, Mujsce AM. J. Am. Chem. Soc 1990;112:4301.

[302]. Acevedo D, Abruna HD. J. Phys. Chem 1991;95:9590.

[303]. Ricci A, Rolli C, Rothacher S, Baraldo L, Bonazzola C, Calvo EJ, Tognalli N, Fainstein A. J. Solid State Electrochem 2007;11:1511.

[304]. Forster RJ, Figgemeier E, Loughman P, Lees A, Hjelm J, Vos JG. Langmuir 2000;16:7871.

[305]. Devaraj NK, Decreau RA, Ebina W, Collman JP, Chidsey CED. J. Phys. Chem. B 2006;110:15955. [PubMed: 16898751]

[306]. Dillmore WS, Yousaf MN, Mrksich M. Langmuir 2004;20:7223. [PubMed: 15301509]

[307]. Gawalt ES, Mrksich M. J. Am. Chem. Soc 2004;126:15613. [PubMed: 15563191]

[308]. Hodneland CD, Mrksich M. Langmuir 1997;13:6001.

[309]. Hodneland CD, Mrksich M. J. Am. Chem. Soc 2000;122:4235.

[310]. Jiang X, Ferrigno R, Mrksich M, Whitesides GM. J. Am. Chem. Soc 2003;125:2366. [PubMed: 12603104]

[311]. Kwon Y, Mrksich M. J. Am. Chem. Soc 2002;124:806. [PubMed: 11817956]

[312]. Luo J, Isied SS. Langmuir 1998;14:3602.

[313]. Seo K, Jeon IC, Yoo DJ. Langmuir 2004;20:4147. [PubMed: 15969409]

[314]. Van Ryswyk H, Turtle ED, Watson-Clark R, Tanzer TA, Herman TK, Chong PY, Waller PJ, Taurog AL, Wagner CE. Langmuir 1996;12:6143.

[315]. Yeo W-S, Hodneland CD, Mrksich M. ChemBioChem 2001;2:590. [PubMed: 11828494]

[316]. Yeo W-S, Mrksich M. Angew. Chem., Int. Ed. Engl 2003;42:3121. [PubMed: 12866096]

[317]. Yeo W-S, Mrksich M. Langmuir 2006;22:10816. [PubMed: 17129065]

[318]. Yeo W-S, Yousaf MN, Mrksich M. J. Am. Chem. Soc 2003;125:14994. [PubMed: 14653727]

[319]. Yousaf MN, Chan EWL, Mrksich M. Angew. Chem., Int. Ed. Engl 2000;39:1943. [PubMed: 10940989]

[320]. Yousaf MN, Mrksich M. J. Am. Chem. Soc 1999;121:4286.

[321]. Atre SV, Liedberg B, Allara DL. Langmuir 1995;11:3882.

[322]. Guiomar AJ, Guthrie JT, Evans SD. Langmuir 1999;15:1198.

[323]. Lahann J, Mitragotri S, Tran T-N, Kaido H, Sundaram J, Choi IS, Hoffer S, Somorjai GA, Langer R. Science 2003;299:371. [PubMed: 12532011]

[324]. Schreiber F. Progress in Surface Science 2000;65:151.

[325]. Cheng J, Saghi-Szabo G, Tossell JA, Miller CJ. J. Am. Chem. Soc 1996;118:680.

[326]. Liang C, Newton MD. J. Phys. Chem 1992;96:2855.

[327]. Liang C, Newton MD. J. Phys. Chem 1993;97:3199.

[328]. Jordan KD, Paddon-Row MN. Journal of Physical Chemistry 1992;96:1188.

[329]. Curtiss LA, Naleway CA, Miller JR. Journal of Physical Chemistry 1993;97:4059.

[330]. Yamamoto H, Waldeck DH. Journal of Physical Chemistry B 2002;106:7469.

[331]. Nuzzo RG, Dubois LH, Allara DL. J. Am. Chem. Soc 1990;112:558.

[332]. Kim B, Beebe JM, Olivier C, Rigaut S, Touchard D, Kushmerick JG, Zhu XY, Frisbie CD. J. Phys. Chem. C 2007;111:7521.

[333]. Dhirani A-A, Zehner RW, Hsung RP, Guyot-Sionnest P, Sita LR. J. Am. Chem. Soc 1996;118:3319.

[334]. Woitellier S, Launay JP, Spangler CW. Inorg. Chem 1989;28:758.

[335]. Adams DM, Brus L, Chidsey CED, Creager S, Creutz C, Kagan CR, Kamat PV, Lieberman M, Lindsay S, Marcus RA, Metzger RM, Michel-Beyerle ME, Miller JR, Newton MD, Rolison DR, Sankey O, Schanze KS, Yardley J, Zhu X. J. Phys. Chem. B 2003;107:6668.

[336]. Dudek SP, Sikes HD, Chidsey CED. J. Am. Chem. Soc 2001;123:8033. [PubMed: 11506559]

[337]. Kushmerick JG, Holt DB, Pollack SK, Ratner MA, Yang JC, Schull TL, Naciri J, Moore MH, Shashidhar R. J. Am. Chem. Soc 2002;124:10654. [PubMed: 12207510]

[338]. Sikes HD, Sun Y, Dudek SP, Chidsey CED, Pianetta P. J. Phys. Chem. B 2003;107:1170.

[339]. Davis WB, Ratner MA, Wasielewski MR. J. Am. Chem. Soc 2001;123:7877. [PubMed: 11493061]

[340]. Yang WR, Jones MW, Li X, Eggers PK, Tao N, Gooding JJ, Paddon-Row MN. J. Phys. Chem. C 2008;112:9072.

[341]. Liu J, Gooding JJ, Paddon-Row MN. Chem. Commun 2005:631.

[342]. Beebe JM, Engelkes VB, Liu J, Gooding JJ, Eggers PK, Jun Y, Zhu X, Paddon-Row MN, Frisbie CD. J. Phys. Chem. B 2005;109:5207. [PubMed: 16863186]

[343]. Gray HB, Winkler JR. Electron Transfer in Chemistry 2001;3:3.

[344]. McGourty JL, Blough NV, Hoffman BM. J. Am. Chem. Soc 1983;105:4470.

[345]. Simolo KP, McLendon GL, Mauk MR, Mauk AG. J. Am. Chem. Soc 1984;106:5012.

[346]. Jackman MP, McGinnis J, Powls R, Salmon GA, Sykes AG. J. Am. Chem. Soc 1988;110:5880.

[347]. Qin L, Rodgers KK, Sligar SG. Mol. Cryst. Liq. Cryst 1991;194:311.

[348]. Conrad DW, Zhang H, Stewart DE, Scott RA. J. Am. Chem. Soc 1992;114:9909.

[349]. Meyer TE, Rivera M, Walker FA, Mauk MR, Mauk AG, Cusanovich MA, Tollin G. Biochemistry 1993;32:622. [PubMed: 8380703]

[350]. Pan LP, Hibdon S, Liu RQ, Durham B, Millett F. Biochemistry 1993;32:8492. [PubMed: 8395206]

[351]. Winkler JR, Malmstroem BG, Gray HB. Biophys. Chem 1995;54:199. [PubMed: 7749059]

[352]. Wang K, Zhen Y, Sadoski R, Grinnell S, Geren L, Ferguson-Miller S, Durham B, Millett F. J. Biol. Chem 1999;274:38042. [PubMed: 10608873]

[353]. Bediako-Amoa I, Sutherland TC, Li C-Z, Silerova R, Kraatz H-B. J. Phys. Chem. B 2004;108:704.

[354]. Mandal HS, Kraatz H-B. Chem. Phys 2006;326:246.

[355]. Morita T, Kimura S. J. Am. Chem. Soc 2003;125:8732. [PubMed: 12862461]

[356]. Sek S, Sepiol A, Tolak A, Misicka A, Bilewicz R. J. Phys. Chem. B 2004;108:8102.

[357]. Takeda K, Morita T, Kimura S. Pept. Sci 2006;43rd:77.

[358]. Watanabe J, Morita T, Kimura S. J. Phys. Chem. B 2005;109:14416. [PubMed: 16852814]

[359]. Devillers CH, Boturyn D, Bucher C, Dumy P, Labbe P, Moutet J-C, Royal G, Saint-Aman E. Langmuir 2006;22:8134. [PubMed: 16952253]

[360]. Doneux T, Bouffier L, Mello LV, Rigden DJ, Kejnovska I, Fernig DG, Higgins SJ, Nichols RJ. J. Phys. Chem. C 2009;113:6792.

[361]. Boussicault F, Robert M. Chem. Rev 2008;108:2622. [PubMed: 18563937]

[362]. Meade, TJ.; Kayyem, JF.; Fraser, SE. Nucleic acid mediated electron transfer. Patent. 9,515,971. Dec 5. 1994

[363]. Yu CJ, Yowanto H, Tao C, Terbrueggen B, Blackburn GF. Polym. Mater. Sci. Eng 2001;84:20.

[364]. Kelley SO, Jackson NM, Hill MG, Barton JK. Angew. Chem., Int. Ed. Engl 1999;38:941.

[365]. Drummond TG, Hill MG, Barton JK. J. Am. Chem. Soc 2004;126:15010. [PubMed: 15547981]

[366]. Liu T, Barton JK. J. Am. Chem. Soc 2005;127:10160. [PubMed: 16028914]

[367]. Li C-Z, Long Y-T, Kraatz H-B, Lee JS. J. Phys. Chem. B 2003;107:2291.

[368]. Long Y-T, Li C-Z, Sutherland TC, Chahma M. h. Lee JS, Kraatz H-B. J. Am. Chem. Soc 2003;125:8724. [PubMed: 12862457]

[369]. Anne A, Demaille C. J. Am. Chem. Soc 2006;128:542. [PubMed: 16402842]

[370]. Anne A, Demaille C. J. Am. Chem. Soc 2008;130:9812. [PubMed: 18593158]

[371]. Frank NL, Meade TJ. Inorg. Chem 2003;42:1039. [PubMed: 12588136]

[372]. Paul A, Watson RM, Wierzbinski E, Davis KL, Sha A, Achim C, Waldeck DH. J. Phys. Chem. B. 2009 ASAP.

[373]. Berlin YA, Burin AL, Ratner MA. Chem. Phys 2002;275:61.

[374]. Roth KM, Yasseri AA, Liu Z, Dabke RB, Malinovskii V, Schweikart K-H, Yu L, Tiznado H, Zaera F, Lindsey JS, Kuhr WG, Bocian DF. J. Am. Chem. Soc 2003;125:505. [PubMed: 12517164]

[375]. Yasseri AA, Syomin D, Loewe RS, Lindsey JS, Zaera F, Bocian DF. J. Am. Chem. Soc 2004;126:15603. [PubMed: 15563190]

[376]. Gosavi S, Marcus RA. J. Phys. Chem. B 2000;104:2067.

[377]. Finklea HO, Yoon K, Chamberlain E, Allen J, Haddox R. J. Phys. Chem. B 2001;105:3088.

[378]. Forster RJ, Loughman P, Keyes TE. J. Am. Chem. Soc 2000;122:11948.

[379]. Cohen-Atiya M, Mandler D. Phys. Chem. Chem. Phys 2006;8:4405. [PubMed: 17001407]

[380]. Slowinski K, Slowinska KU, Majda M. J. Phys. Chem. B 1999;103:8544.

[381]. Laibinis PE, Whitesides GM, Allara DL, Tao YT, Parikh AN, Nuzzo RG. J. Am. Chem. Soc 1991;113:7152.

[382]. Himmelhaus M, Gauss I, Buck M, Eisert F, Woll C, Grunze M. J. Electron Spectrosc. Relat. Phenom 1998;92:139.

[383]. Ziegler KJ, Doty RC, Johnston KP, Korgel BA. J. Am. Chem. Soc 2001;123:7797. [PubMed: 11493053]

[384]. Vogt AD, Han T, Beebe TP Jr. Langmuir 1997;13:3397.

[385]. Mekhalif Z, Laffineur F, Couturier N, Delhalle J. Langmuir 2003;19:637.

[386]. Mekhalif Z, Riga J, Pireaux JJ, Delhalle J. Langmuir 1997;13:2285.

[387]. Bengio S, Fonticelli M, Benitez G, Creus AH, Carro P, Ascolani H, Zampieri G, Blum B, Salvarezza RC. J. Phys. Chem. B 2005;109:23450. [PubMed: 16375318]

[388]. Hoertz PG, Niskala JR, Dai P, Black HT, You W. J. Am. Chem. Soc 2008;130:9763. [PubMed: 18597470]

[389]. Love JC, Wolfe DB, Haasch R, Chabinyc ML, Paul KE, Whitesides GM, Nuzzo RG. J. Am. Chem. Soc 2003;125:2597. [PubMed: 12603148]

[390]. Carvalho A, Geissler M, Schmid H, Michel B, Delamarche E. Langmuir 2002;18:2406.

[391]. Corthey G, Rubert AA, Benitez GA, Fonticelli MH, Salvarezza RC. J. Phys. Chem. C 2009;113:6735.

[392]. Williams JA, Gorman CB. J. Phys. Chem. C 2007;111:12804.

[393]. Jiang X, Bruzewicz DA, Thant MM, Whitesides GM. Anal. Chem 2004;76:6116. [PubMed: 15481961]

[394]. Love JC, Wolfe DB, Chabinyc ML, Paul KE, Whitesides GM. J. Am. Chem. Soc 2002;124:1576. [PubMed: 11853422]

[395]. Soreta TR, Strutwolf J, O'Sullivan CK. Langmuir 2007;23:10823. [PubMed: 17850100]

[396]. Linford MR, Chidsey CED. J. Am. Chem. Soc 1993;115:12631.

[397]. Sailor MJ, Lee EJ. Adv. Mater. (Weinheim, Ger.) 1997;9:783.

[398]. Choi CH, Liu D-J, Evans JW, Gordon MS. J. Am. Chem. Soc 2002;124:8730. [PubMed: 12121118]

[399]. Dubois LH, Nuzzo RG. Annual Review of Physical Chemistry 1992;43:437.

[400]. Grandbois M. Science 1999;283:1727. [PubMed: 10073936]

[401]. Bergman PJ. Journal of Applied Physics 1995;78:1271.

[402]. Dai M, Wang Y, Kwon J, Halls MD, Chabal YJ. Nature Materials 2009:1.

[403]. Watanabe S, Nakayama N, Ito T. Applied Physical Letters 1991;59:1458.

[404]. Dalchiele EA, Aurora A, Bernardini G, Cattaruzza F, Flamini A, Pallavicini P, Zanoni R, Decker F. J. Electroanal. Chem 2005;579:133.

[405]. Hasobe T, Imahori H, Ohkubo K, Yamada H, Sato T, Nishimura Y, Yamazaki I, Fukuzumi S. J. Porphyrins Phthalocyanines 2003;7:296.

[406]. Li J, Wang L, Liu J, Evmenenko G, Dutta P, Marks TJ. Langmuir 2008;24:5755. [PubMed: 18457433]

[407]. Bigelow WC, Pickett DL, Zisman WA. J. Colloid Sci 1946;1:513.

[408]. Whittington SG, Chapman D. Trans. Faraday Soc 1966;62:3319.

[409]. Scott HL Jr. Biochim Biophys Acta 1977;469:264. [PubMed: 901787]

[410]. Belle J, Bothorel P. Biochem. Biophys. Res. Commun 1974;58:433. [PubMed: 4407174]

[411]. Bothorel P, Belle J, Lemaire B. Chem. Phys. Lipids 1974;12:96. [PubMed: 4826919]

[412]. Marcelja S. Biochim. Biophys. Acta, Biomembr 1974;367:165.

[413]. Marcelja S. J. Chem. Phys 1974;60:3599.

[414]. Marcelja S. Biochim. Biophys. Acta, Biomembr 1976;455:1.

[415]. Duffy DM, Harding JH. Langmuir 2005;21:3850. [PubMed: 15835946]

[416]. Haran M, Goose JE, Clote NP, Clancy P. Langmuir 2007;23:4897. [PubMed: 17397195]

[417]. Jang YH, Jang SS, Goddard WA III. J. Am. Chem. Soc 2005;127:4959. [PubMed: 15796562]

[418]. Pertsin AJ, Grunze M. Langmuir 2000;16:8829.

[419]. Sieval AB, van den Hout B, Zuilhof H, Sudhoelter EJR. Langmuir 2001;17:2172.

[420]. Cotterill RMJ. Biochimica et Biophysica Acta 1976;433:264.

[421]. Toxvaerd S. J. Chem. Phys 1977;67:2056.
[422]. Kox AJ, Michels JPJ, Wiegel FW. Nature 1980;287:317.
[423]. Van der Ploeg P, Berendsen HJC. J. Chem. Phys 1982;76:3271.
[424]. Harris J, Rice SA. J. Chem. Phys 1988;89:5898.
[425]. Hautman J, Klein ML. J. Chem. Phys 1989;91:4994.
[426]. Sellers H, Ulman A, Shnidman Y, Eilers JE. J. Am. Chem. Soc 1993;115:9389.
[427]. Bain CD, Whitesides GM. Angew. Chem 1989;101:522.
[428]. Prime KL, Whitesides GM. Science 2009;252:1164.
[429]. Whitesides GM, Allara DL, Parikh AN, Nuzzo RG. J. Am. Chem. Soc 1991;113:7152.
[430]. Whitesides GM, Laibinis PE. Langmuir 1990;6:87.
[431]. Alves CA, Smith EL, Porter MD. J. Am. Chem. Soc 1992;114:1222.
[432]. Bryant MA, Pemberton JE. J. Am. Chem. Soc 1991;113:8284.
[433]. Camillone N III, Chidsey CED, Eisenberger P, Fenter P, Li J, Liang KS, Liu GY, Scoles G. J. Chem. Phys 1993;99:744.
[434]. Camillone N III, Chidsey CED, Liu GY, Scoles G. J. Chem. Phys 1993;98:3503.
[435]. Delamarche E, Michel B, Gerber C, Anselmetti D, Guentherodt HJ, Wolf H, Ringsdorf H. Langmuir 1994;10:2869.
[436]. Fenter P, Eisenberger P, Liang KS. Phys. Rev. Lett 1993;70:2447. [PubMed: 10053564]
[437]. Kang J, Rowntree PA. Langmuir 1996;12:2813.
[438]. Mar W, Klein ML. Langmuir 1994;10:188.
[439]. Nuzzo RG, Korenic EM, Dubois LH. J. Chem. Phys 1990;93:767.
[440]. Poirier GE, Tarlov MJ. J. Phys. Chem 1995;99:10966.
[441]. Poirier GE, Tarlov MJ, Rushmeier HE. Langmuir 1994;10:3383.
[442]. Rovida G, Pratesi F. Surf. Sci 1981;104:609.
[443]. Widrig CA, Alves CA, Porter MD. J. Am. Chem. Soc 1991;113:2805.
[444]. Li T-W, Chao I, Tao Y-T. J. Phys. Chem. B 1998;102:2935.
[445]. Bond AD. New J. Chem 2004;28:104.
[446]. Wenzl I, Yam CM, Barriet D, Lee TR. Langmuir 2003;19:10217.
[447]. Kim Y-H, Jang Seung S, Goddard William A. J Chem Phys 2005;122:244703. [PubMed: 16035789]
[448]. Prime KL, Whitesides GM. Science 1991;252:1164.
[449]. Harder P, Grunze M, Dahint R, Whitesides GM, Laibinis PE. J. Phys. Chem. B 1998;102:426.
[450]. Wang RLC, Kreuzer HJ, Grunze M. J. Phys. Chem. B 1997;101:9767.
[451]. Goujon F, Bonal C, Limoges B, Malfreyt P. Langmuir 2009;25:9164. [PubMed: 19449821]
[452]. Sek S, Swiatek K, Misicka A. J. Phys. Chem. B 2005;109:23121. [PubMed: 16375270]
[453]. Sek S, Misicka A, Swiatek K, Maicka E. J. Phys. Chem. B 2006;110:19671. [PubMed: 17004836]
[454]. Sakamoto S, Aoyagi H, Nakashima N, Mihara H. J. Chem. Soc., Perkin Trans 1996;2:2319.
[455]. Brennan JL, Howlett M, Forster RJ. Faraday Discuss 2002;121:391. [PubMed: 12227581]

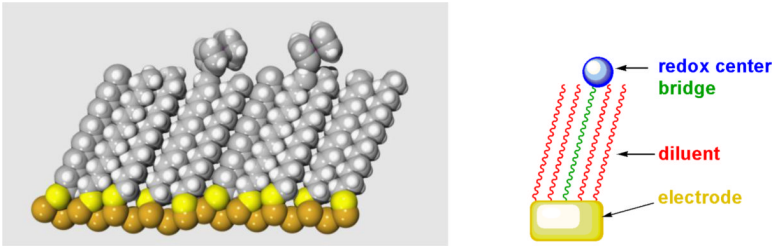

Figure 1.1.
Redox-active SAM consisting of a redox center, a bridge, and a diluent. Left: space-filled molecular view. Right: legend of the SAM components. The bridge connects the electrode and the redox center, while the diluent serves as a spacer molecule to isolate the redox centers from one another.

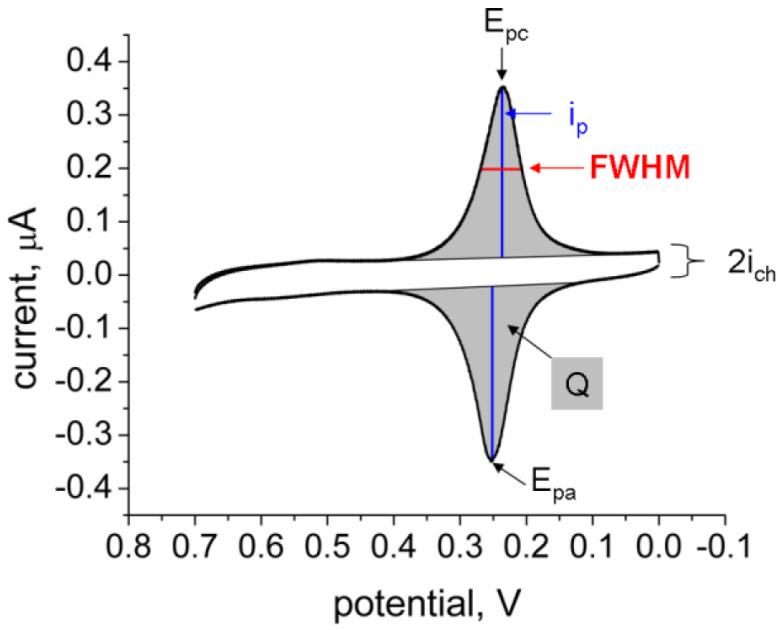

Figure 2.1.
Relevant parameters of a CV of a surface-bound redox species. Parameters include: E_{pc}, E_{pa}, i_{ch}, i_p, Q, and FWHM.

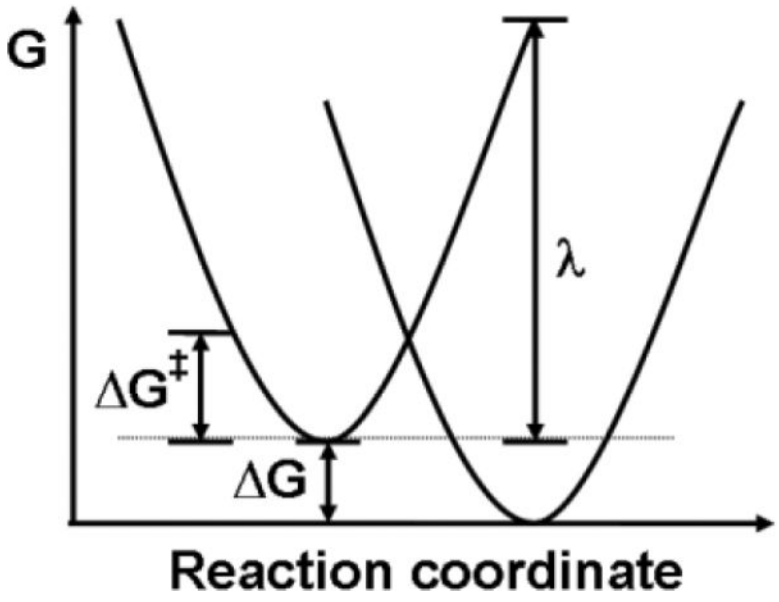

Figure 2.2.
Diabatic free energy curves for nonadiabatic electron transfer. ΔG represents the driving force for ET, $\Delta G^{\ddagger}$ is the activation energy, and λ represents the reorganization energy.

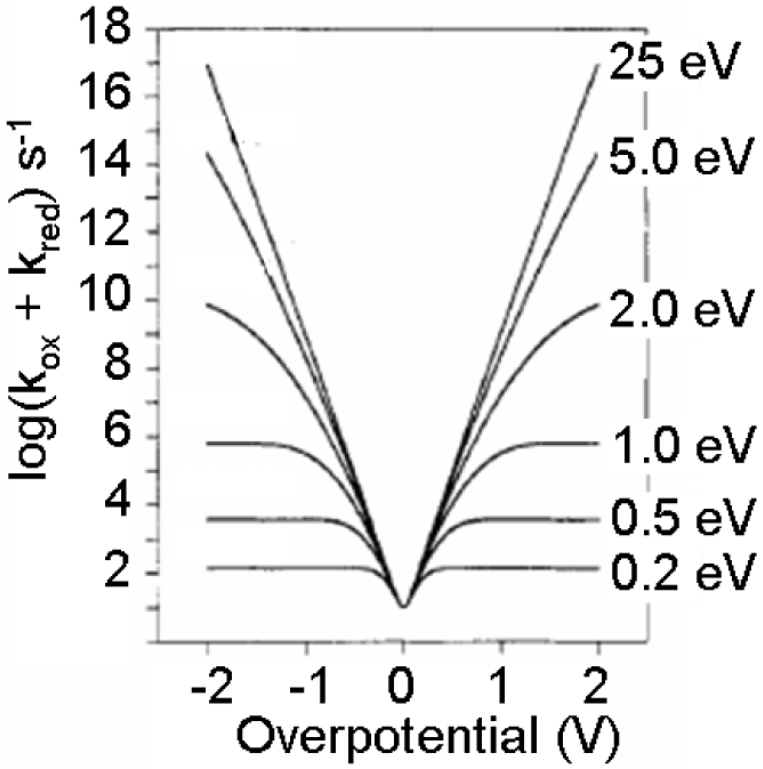

Figure 2.3.
A series of plots for values of λ ranging from 0.2 eV to 25 eV. These curves were generated using the Marcus model. Adapted with permission from reference [70].

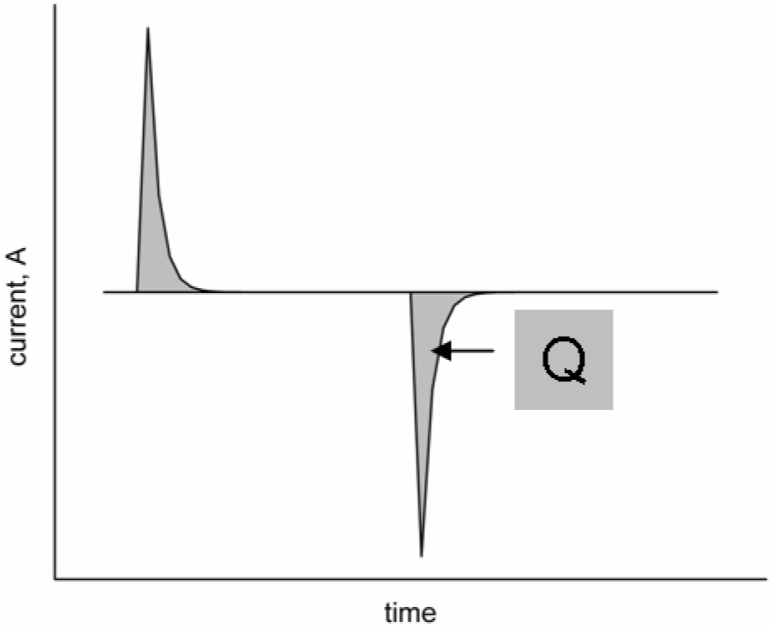

Figure 2.4.
Example of chronoamperometric data from a double step experiment. After a potential step, the current decays with time. Q represents the total charge that has passed to fully oxidize or reduce the surface species.

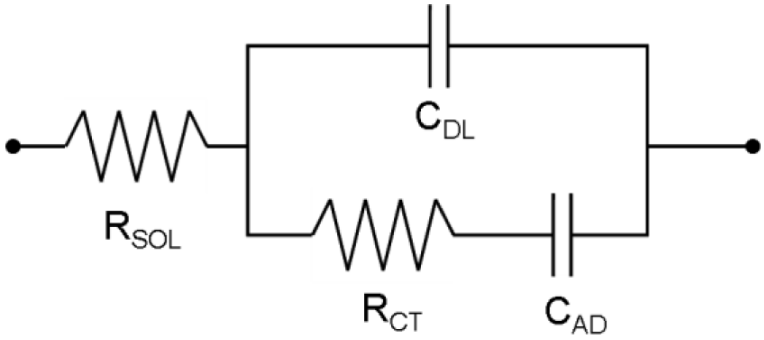

Figure 2.5.
Randles circuit for a redox species attached to a monolayer. Adapted from reference [77].

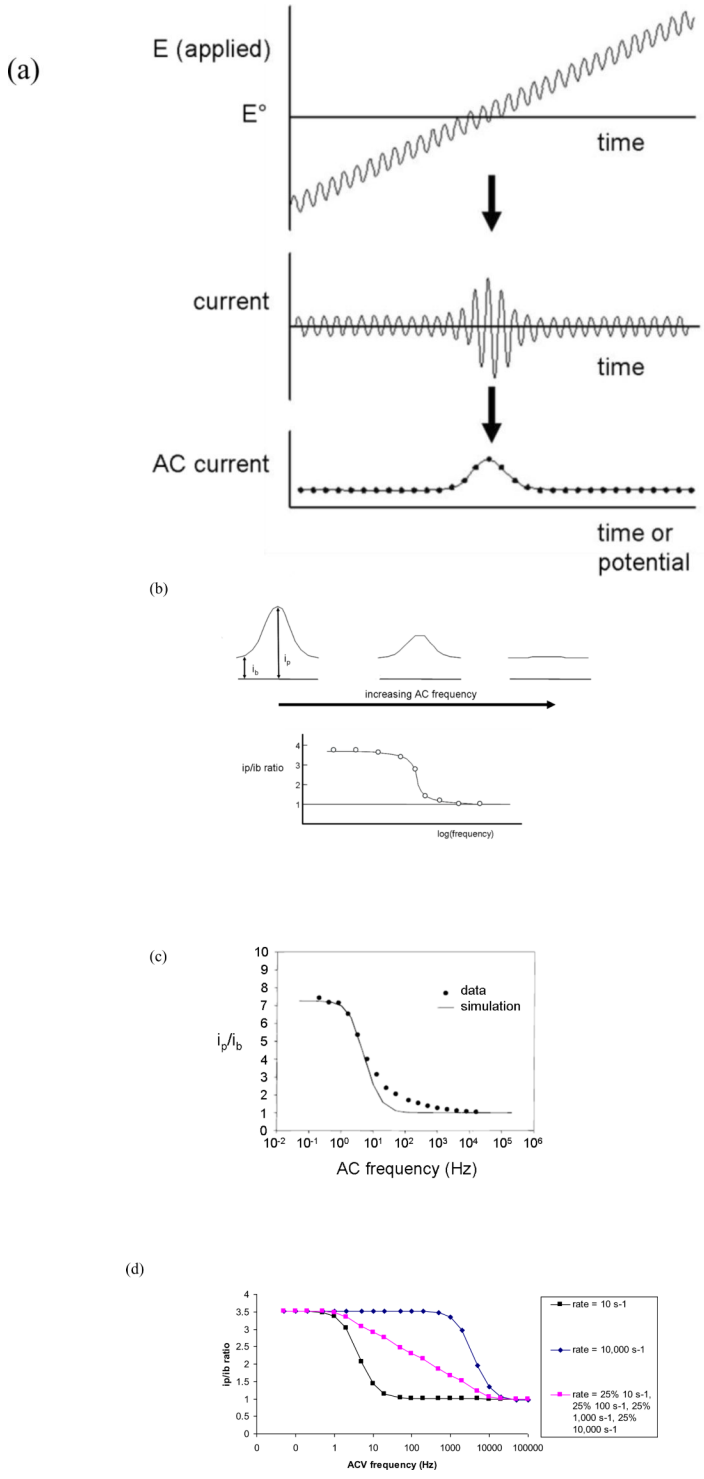

Figure 2.6.

(a) AC voltammetry wave form showing the oscillating component of the potential sweep (E vs. time), the measured current signal vs. time, and the data representation, AC current vs. potential. (b) The peak current i_p and the background current $i_b$are measured for a series of frequencies. The ratio i_p/i_b vs log frequency is plotted. (c) ACV data plot of i_p/i_b vs. frequency showing a distribution of rates. Reproduced with permission from reference [77]. (d) Examples

of simulated ACV i_p/i_b plots for single rates (black and blue) and for a distribution of rates (pink) 25% 10 s^{-1}; 25% 100 s^{-1}; 25% 1,000 s^{-1}, 25% 10,000s^{-1}.

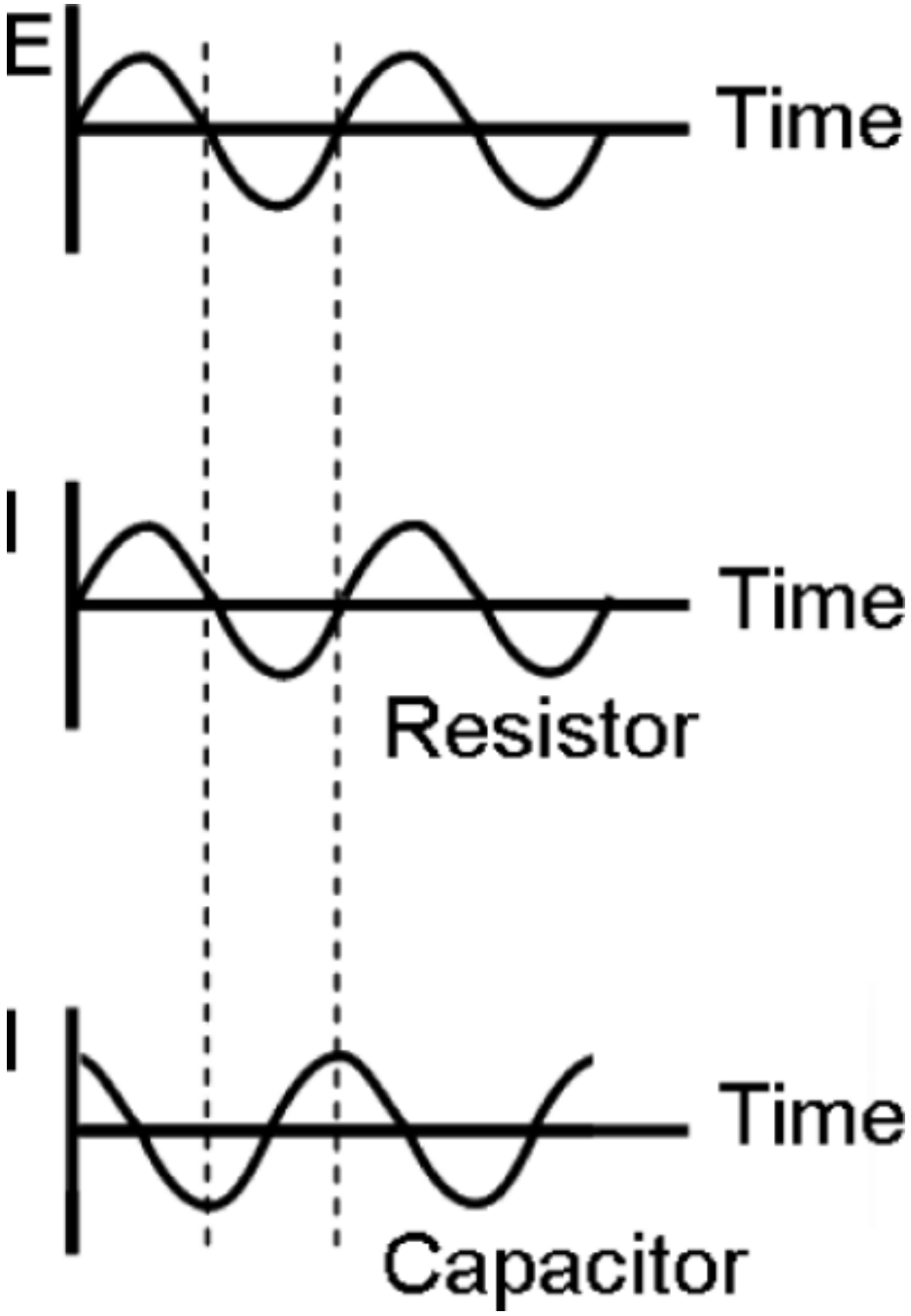

Figure 2.7.
Schematic showing the effect of a resistor and a capacitor on the phase (φ) of an alternating current (I) with respect to the voltage (E). For a resistor, current and voltage are in phase. For a capacitor, voltage lags current by 90°.

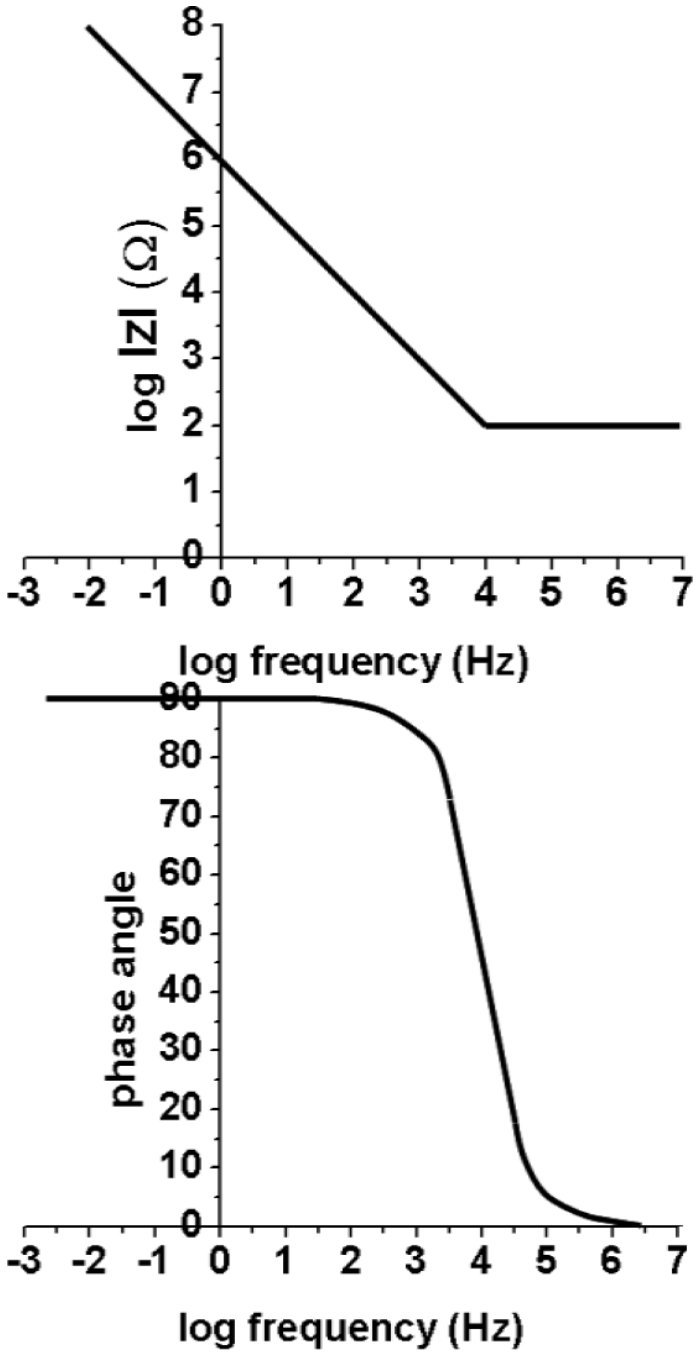

Figure 2.8.
Example of a Bode plot for a series circuit containing only R_{SOL} (100 Ω) and C_{DL} (1 μF). Adapted from reference [46].

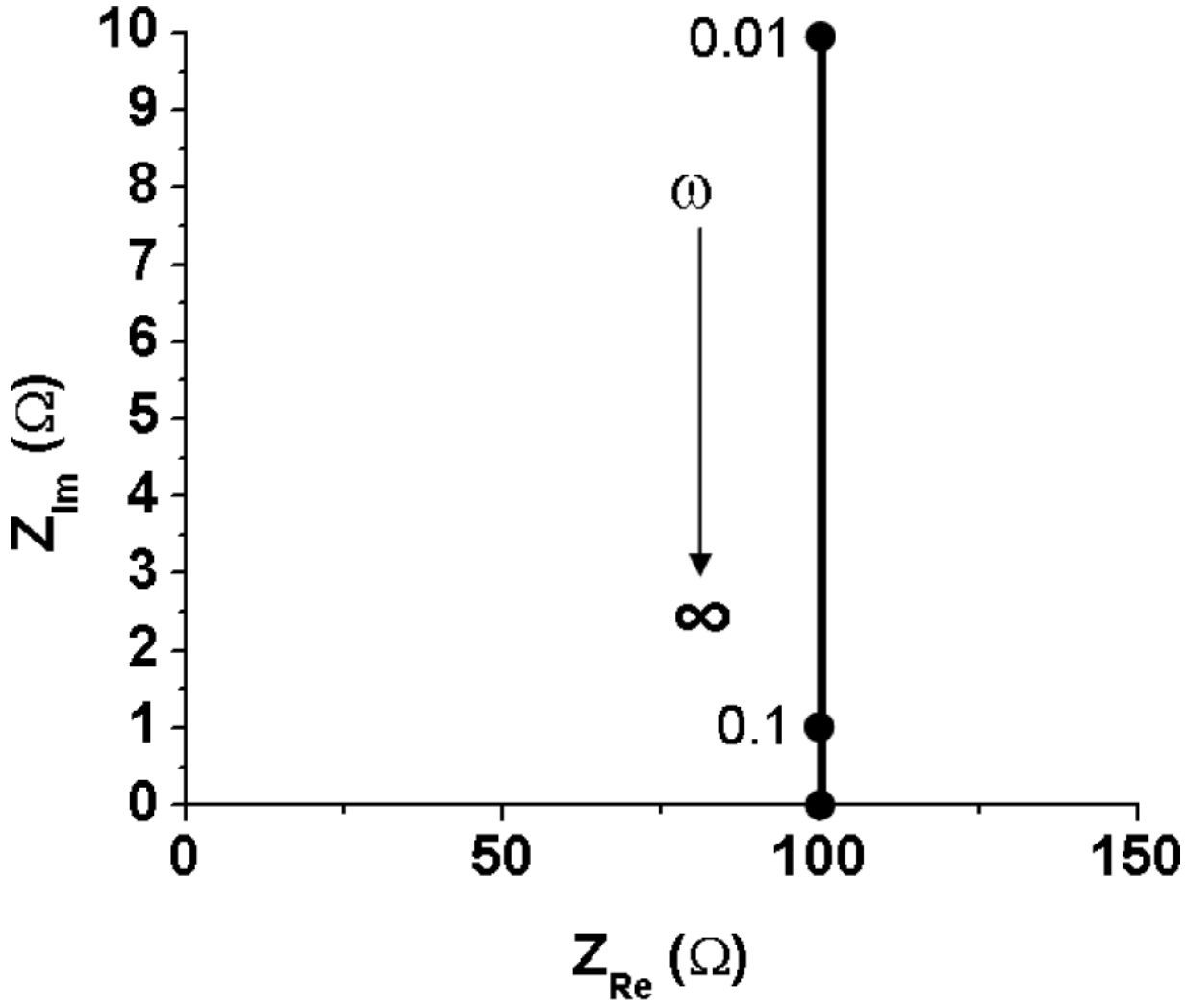

Figure 2.9.
Example of a Nyquist plot for a series circuit containing only R_{SOL} (100 Ω) and C_{DL}. The vertical line on the right approaches the Z_{Re} axis at R_{SOL} as $\omega \rightarrow \infty$ (indicated by the arrow). For reference, points are shown at ω = 0.01 and 0.1. Adapted from reference [46].

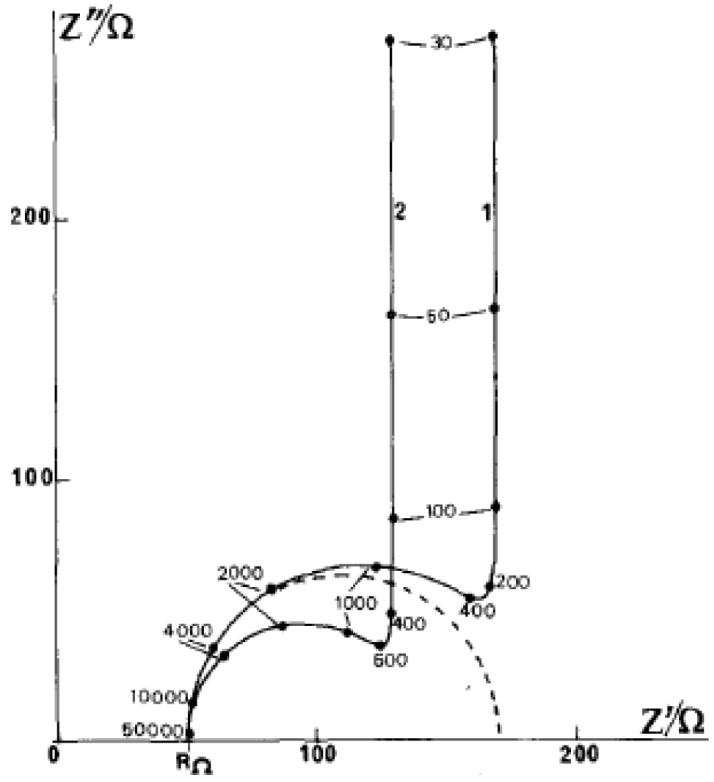

Figure 2.10.

Examples of a Nyquist plots for a Randles circuit for a redox species attached to a monolayer. $R_{\Omega} = R_{SOL}$, $Z' = Z_{Re}$, $Z'' = Z_{Im}$. R_{SOL} is 50 Ω, C_{DL} is 1 μF, C_{AD} is 18.8 μF, R_{CT} is, for (1) 133 Ω and (2) 88.8 Ω. The dashed line is the limiting ellipse for (1); this is what the plot would look like if C_{AD} were 0 μF. See the text for descriptions of the partial ellipses and the vertical portion of the plots. Reproduced with permission from reference [97].

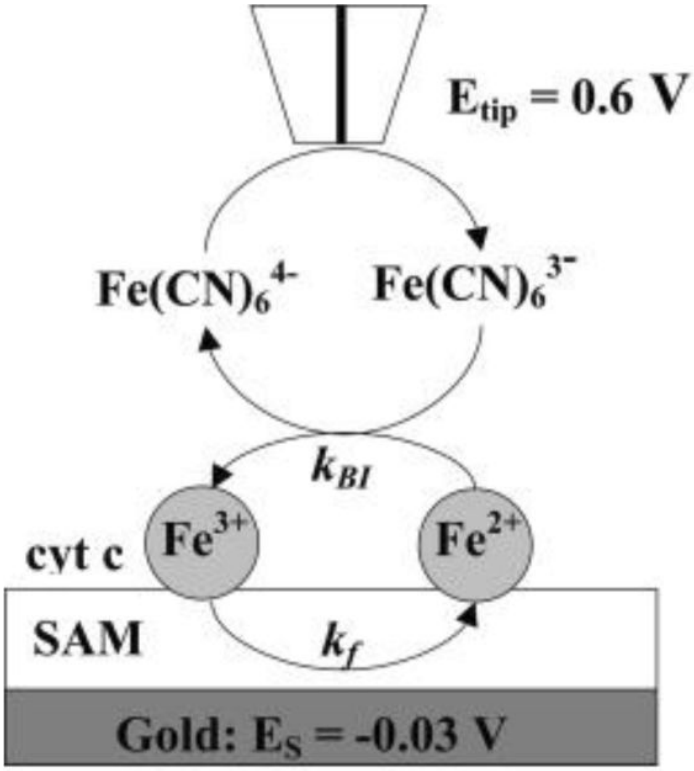

Figure 2.11.
Schematic of mediated electron transfer using SECM. k_{BI} is the rate of ET between ferricyanide (formed at the microelectrode tip) and Fe^{2+} of cytochrome c. k_f is the rate of tunneling ET between cytochrome c in the Fe^{3+} state and the gold electrode. Reproduced with permission from reference [105].

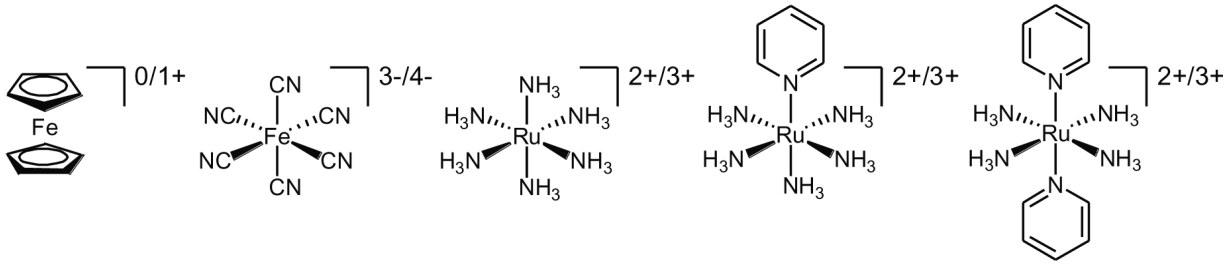

Figure 3.1.
Examples of metal complexes commonly used in SAM studies. Each complex possesses the requirements of a reversible electrochemical reaction and energetically accessible redox potential.

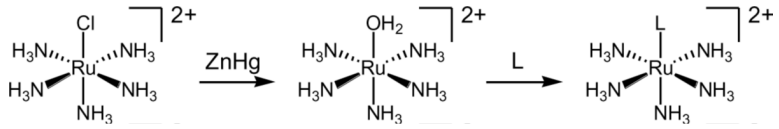

Figure 3.2.
Synthetic scheme for the preparation of Ru(II) pentaammine complexes. The ligand, L is typically a pyridine or imidazole derivative.

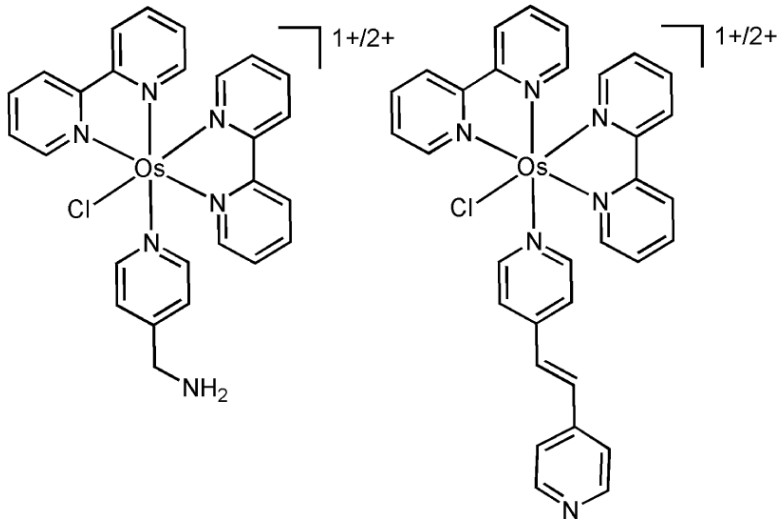

Figure 3.3.
Os(II) bipyridine complexes commonly used for SAM electrochemistry.

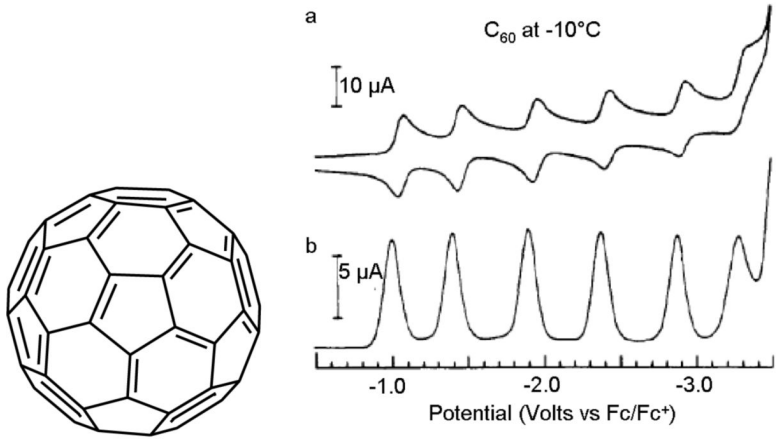

Figure 3.4.
The structure of C_{60} and the electrochemical response in (a) CV and (b) DPV. Used with permission from [161].

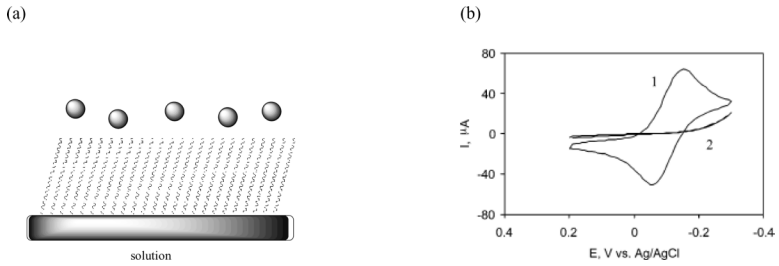

Figure 3.5.

(a) A monolayer acts as a barrier to electron transfer between the electrode and redox species in solution. (b) **1**: CV of $Ru(NH_3)_6Cl_3$ at a bare gold electrode. **2**: CV of $Ru(NH_3)_6Cl_3$ at a gold electrode passivated by a mixed monolayer of $FcCONH(CH_2)_7SH$ and $CH_3(CH)_8SH$. The redox couple for Fc is >0.2V and is not shown. Note the μA scale of the y-axis. The current for trace **2** is on the nA scale, therefore it cannot be seen when shown on the scale needed for **1** to be visualized. Reproduced with permission from [104].

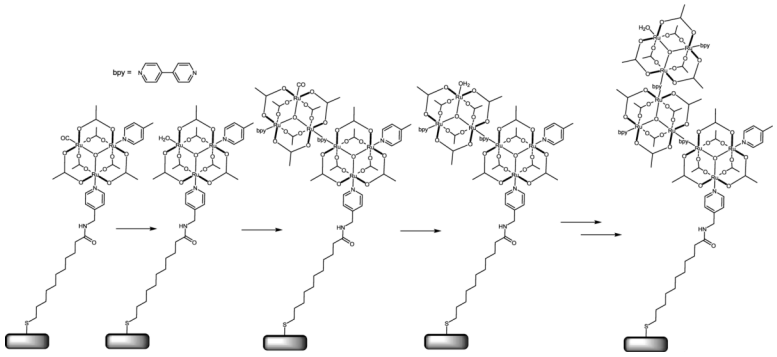

Figure 3.6.
Schematic of sequential multilayer formation using $[Ru_3(\mu_3\text{-}O)(\mu\text{-}CH_3COO)_6(4\text{-}AMP)(4\text{-}MePy)(CO)]$ and $[Ru_3(\mu_3\text{-}O)(\mu\text{-}CH_3COO)_6(bpy)_2(CO)]$. Adapted from reference [184].

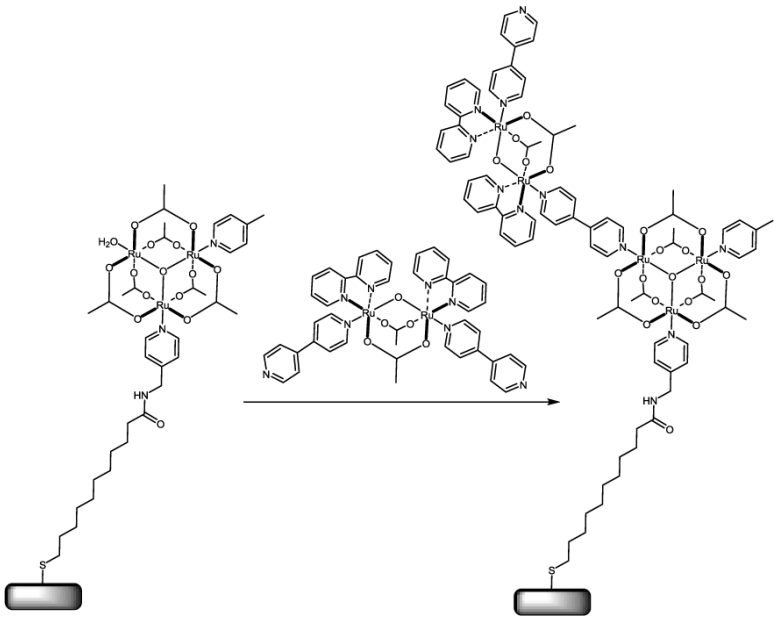

Figure 3.7.
Schematic of multilayer formation using $[Ru_3(\mu_3\text{-}O)(\mu\text{-}CH_3COO)_6(4\text{-}AMP)(4\text{-}MePy)(CO)]$ and $[Ru_2(\mu\text{-}O)(\mu\text{-}CH_3COO)_2(2,2'\text{-}bpy)_2(4,4'\text{-}bpy)_2](PF_6)_2$. Adapted from reference [186].

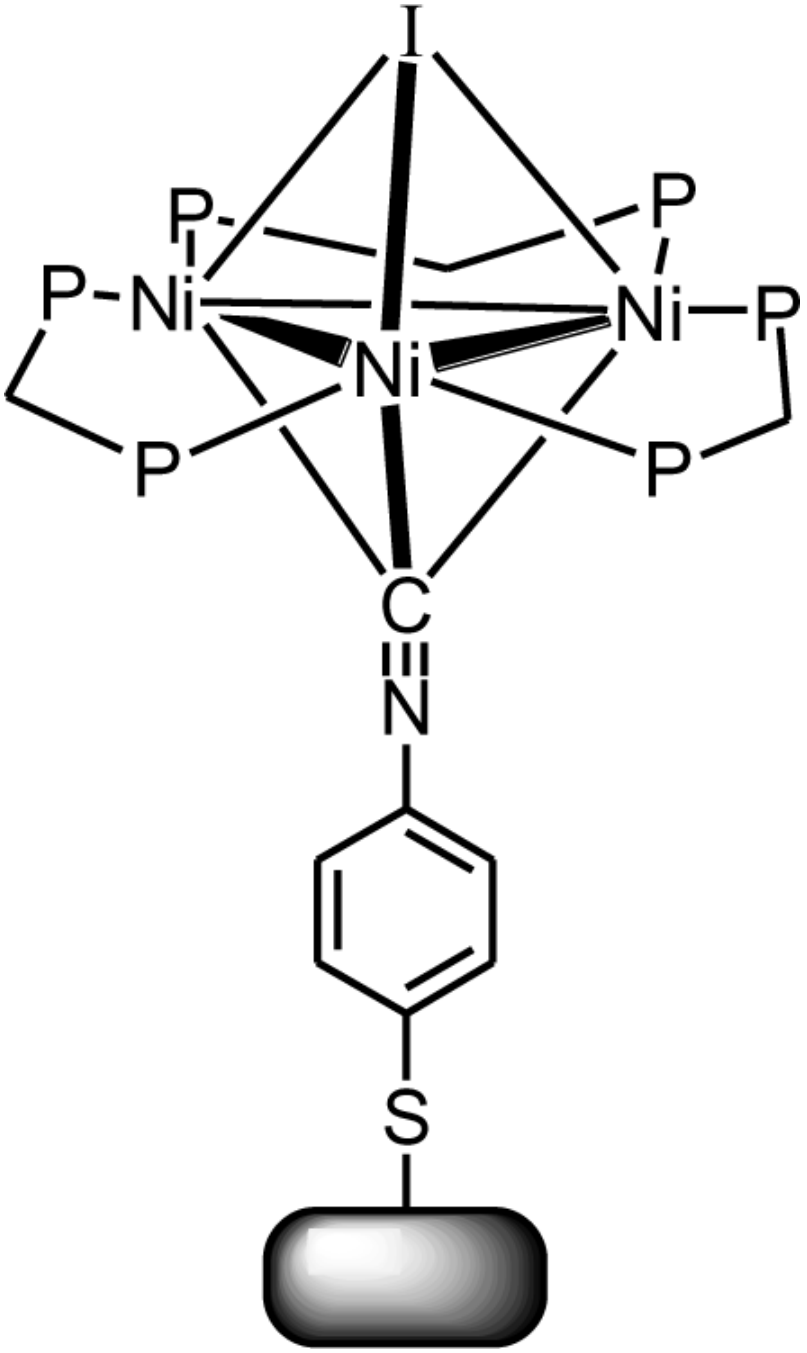

Figure 3.8.
Structure of the nickel cluster $[Ni_3(\mu_3\text{-}I)(\mu_3\text{-}CNR)(\mu_2\text{-}dppm)_3]^+$ bound to a gold surface via a gold-thiolate bond. Adapted from reference [187].

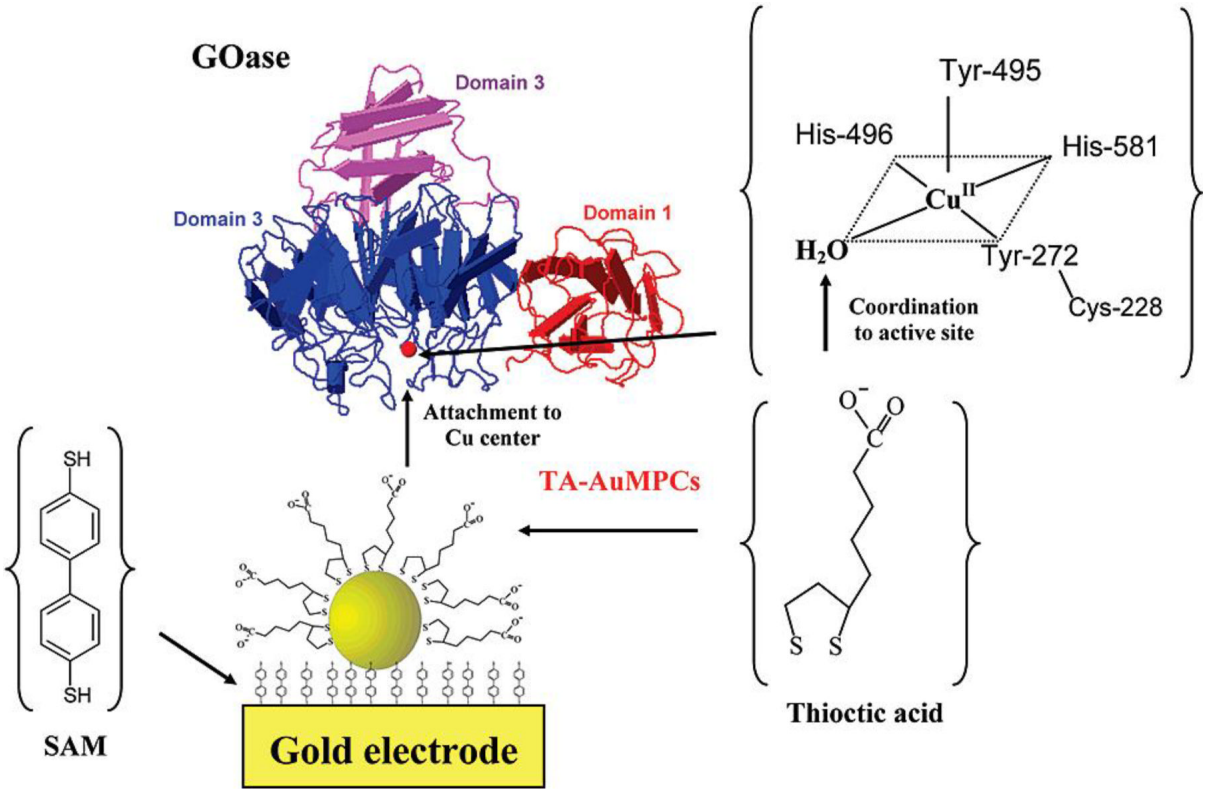

Figure 3.9.
Schematic of formation of a construct incorporating gold clusters, used to form an electrical contact between Cu(II) of galactose oxidase and a gold electrode. Reproduced with permission from reference [17].

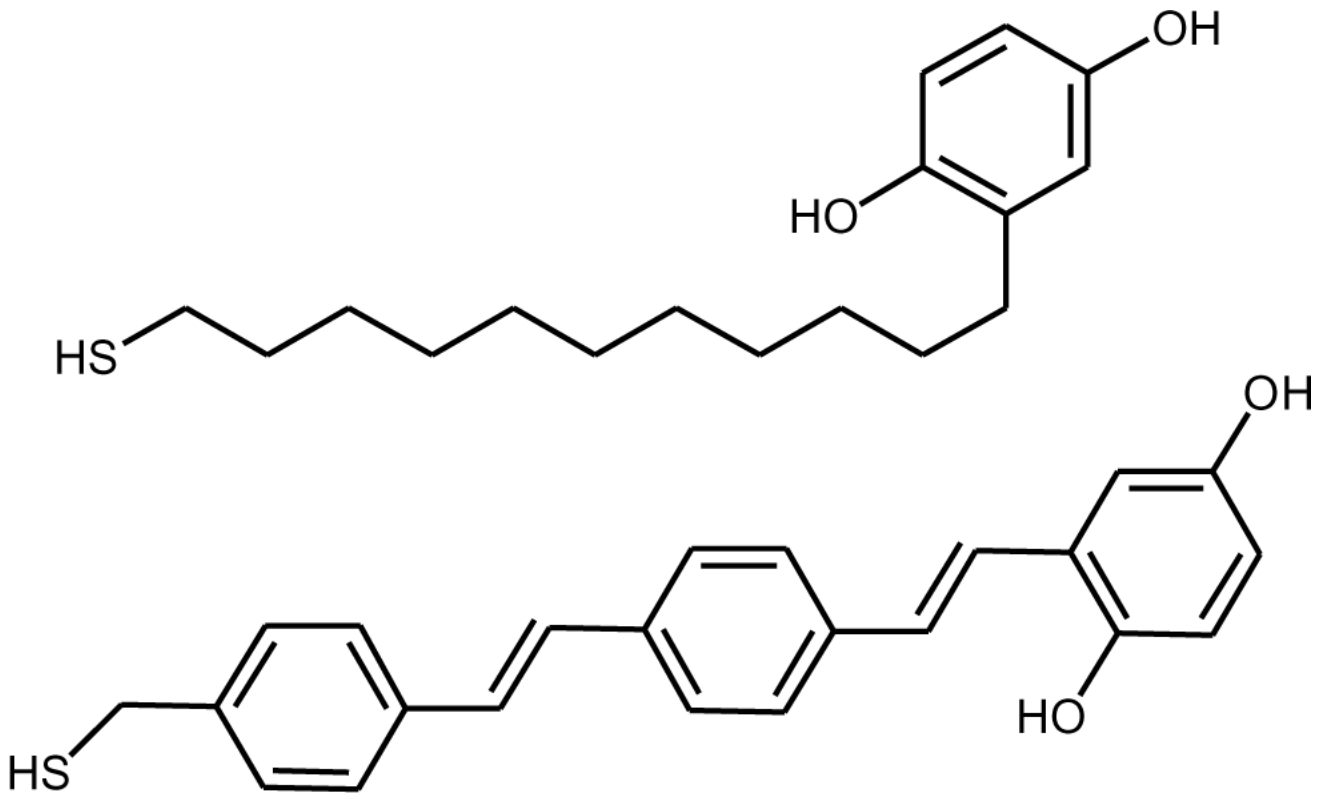

Figure 4.1.
Structures of **HQ-C11** and **HQ-OPV** that were studied in SAMs mixed with octane-1-thiol as the diluent in reference [16].

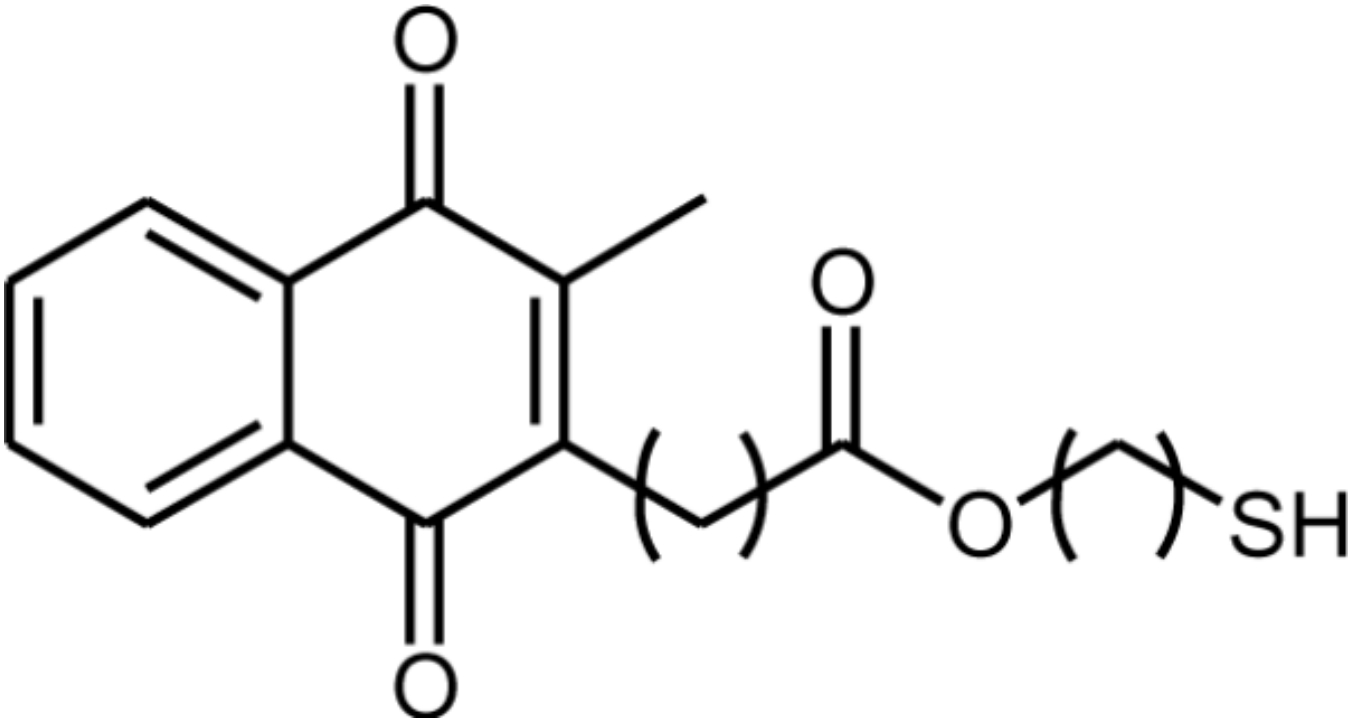

Figure 4.2.
Structure of 2-methyl-1,4-naphthoquinone studied in reference [213].

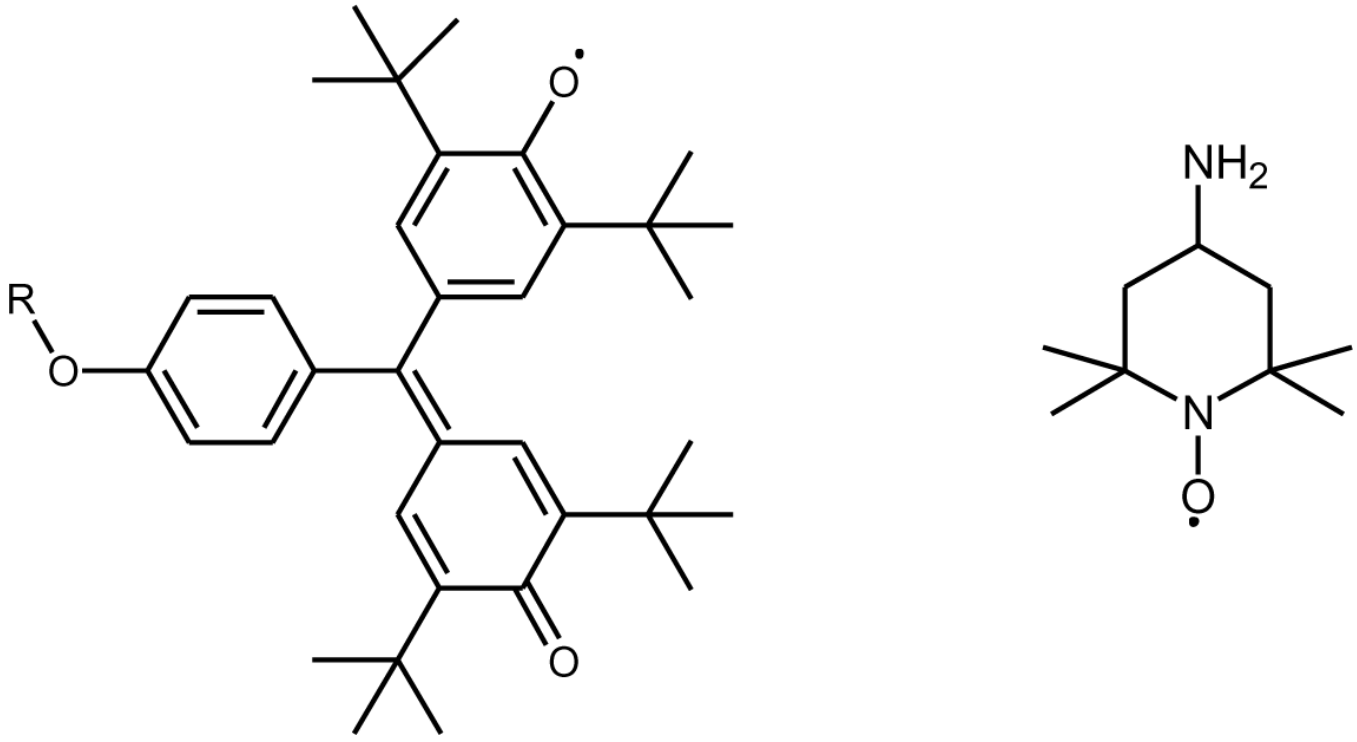

Figure 4.3.
The structures of galvinoxyl (left) and 4-amino-TEMPO (right). In references 204 and 205, the galvinoxyl was attached to the SAM via the R group, an alkane thiol.

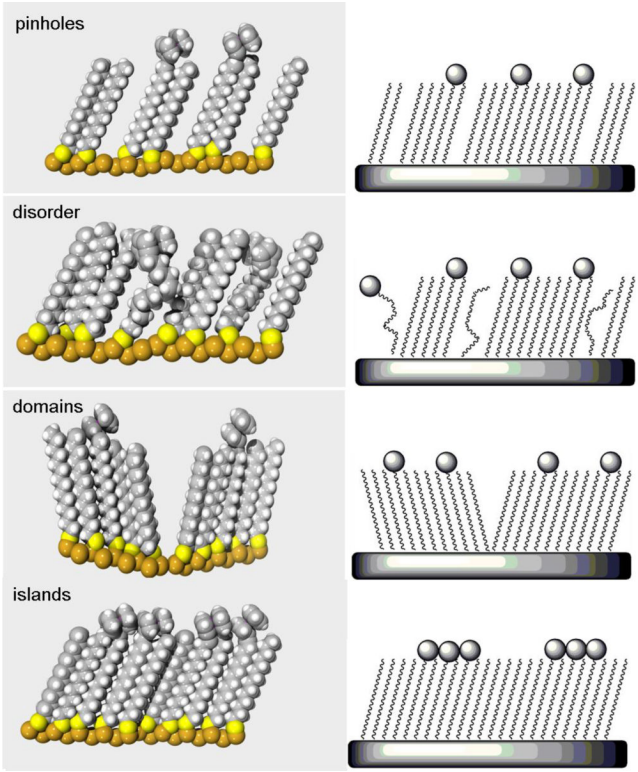

Figure 5.1.
Illustration of possible SAM defects.

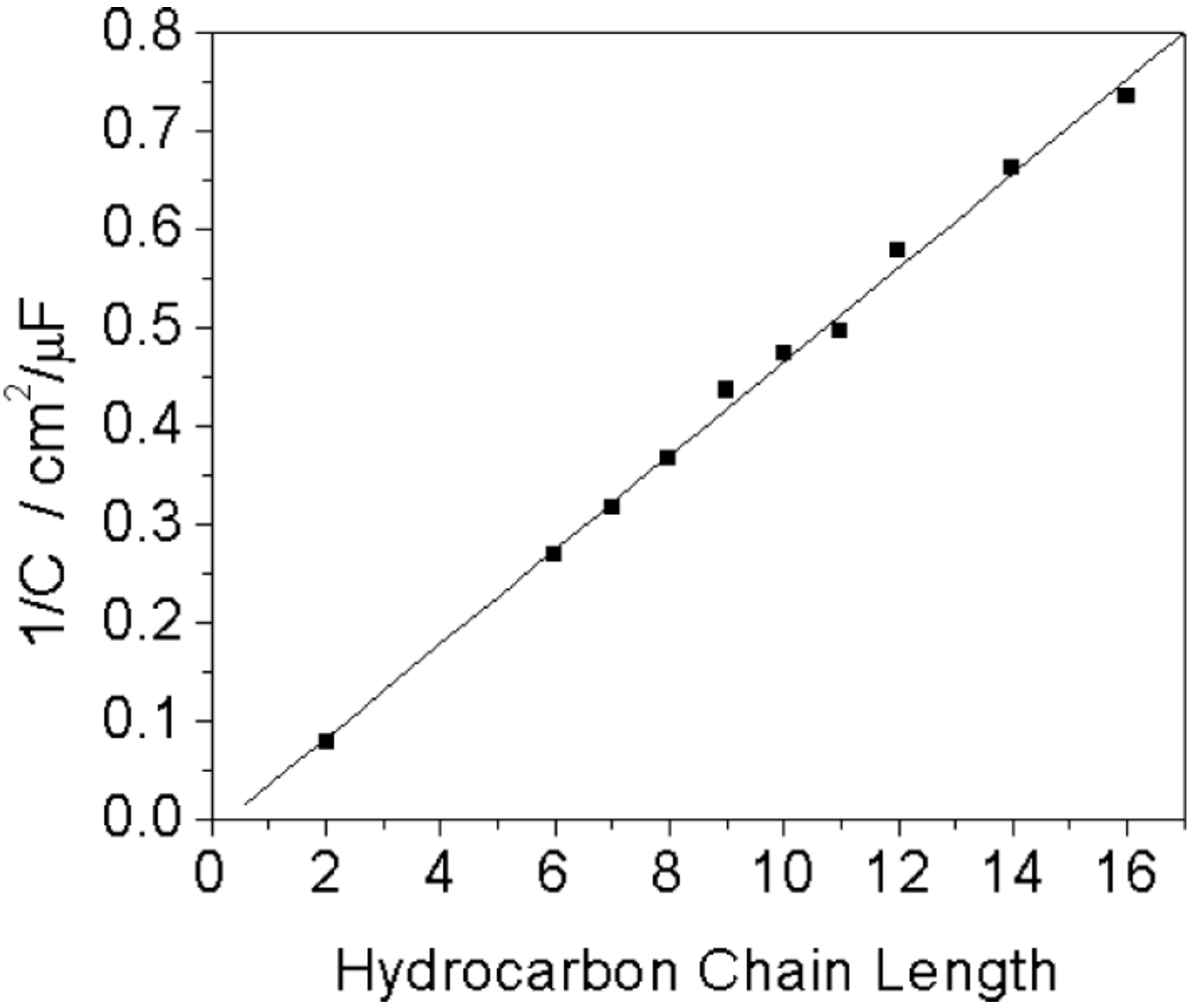

Figure 5.2.
Plot of the reciprocal of the capacitance vs. SAM hydrocarbon chain length for a series of hydroxyl-terminated alkane thiols measured by cyclic voltammetry in 10 mM pH 7.4 Tris buffer with 100 mM KCl. Adapted with permission from reference [38].

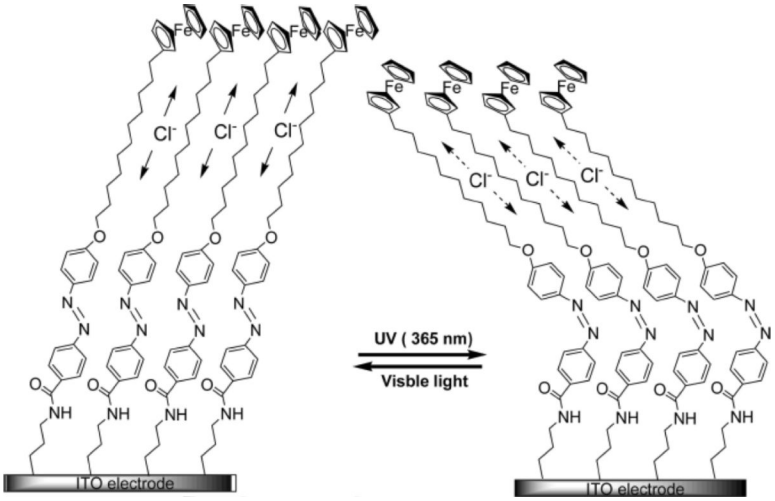

Figure 5.3.
Photoisomerization of azobenzene changes the SAM packing. Reproduced with permission from [292].

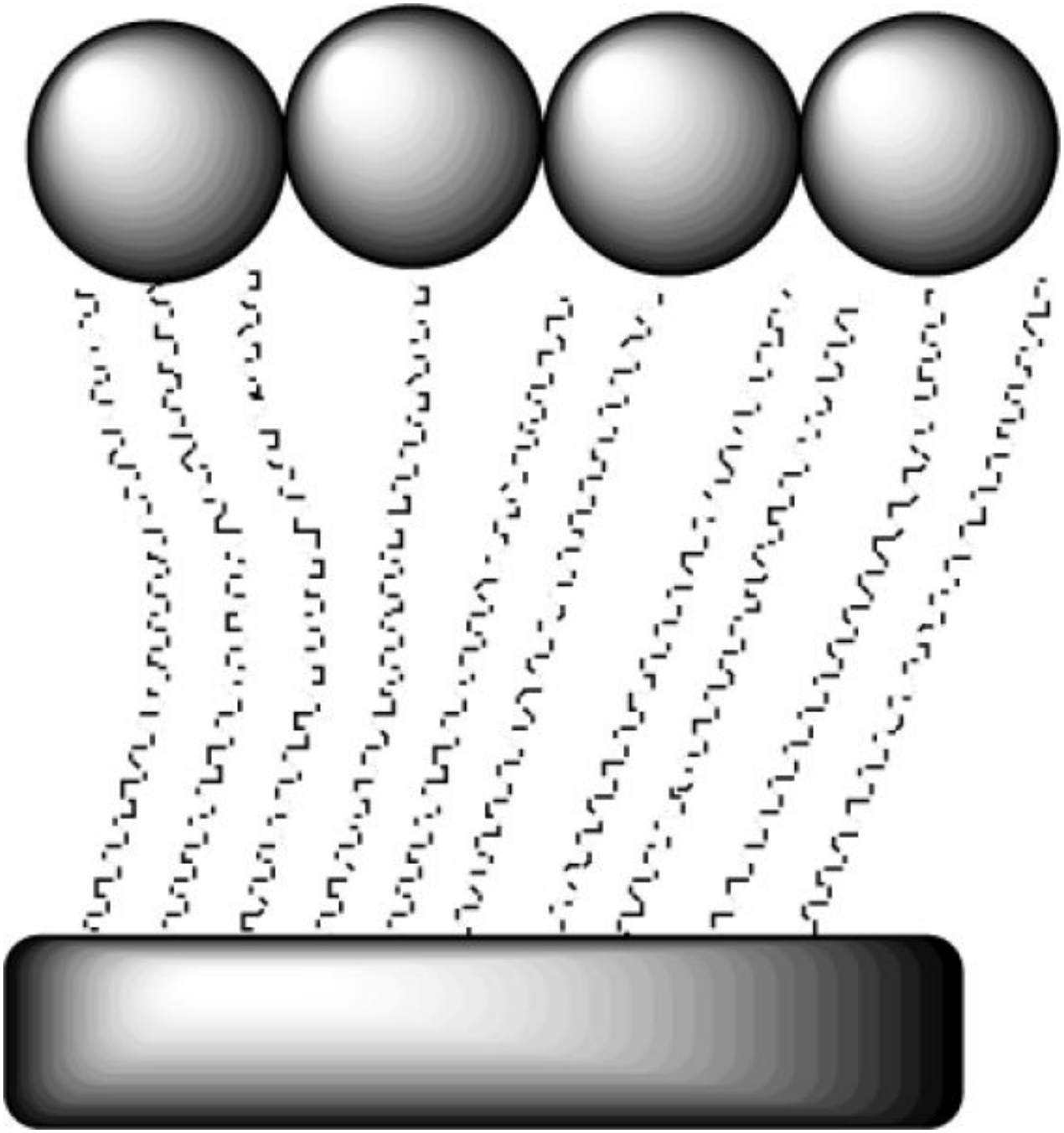

Figure 5.4.
Bulky headgroups can interfere with formation of an ordered monolayer.

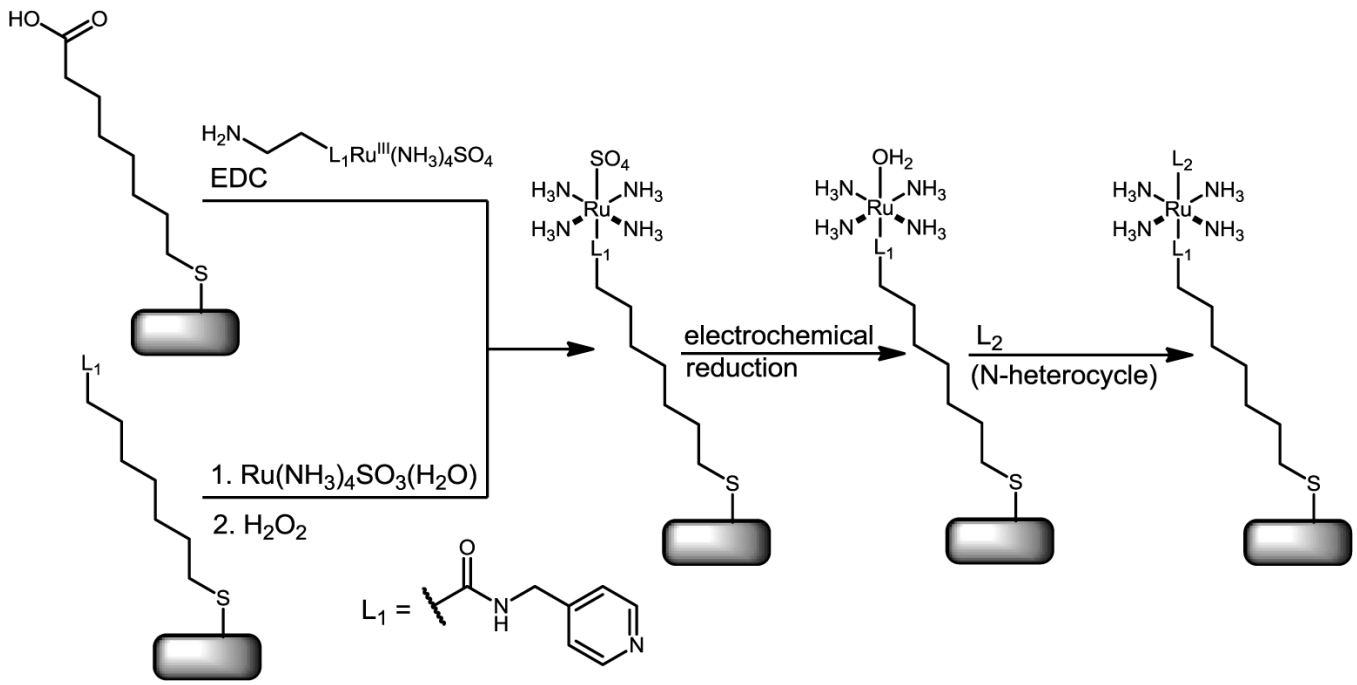

Figure 5.5.
Formation of *trans*-[Ru(II)$(NH_3)_4(SO_3)(L_1)$] SAMs after initial monolayer formation via a ligand substitution reaction and peptide coupling. Adapted from reference [312].

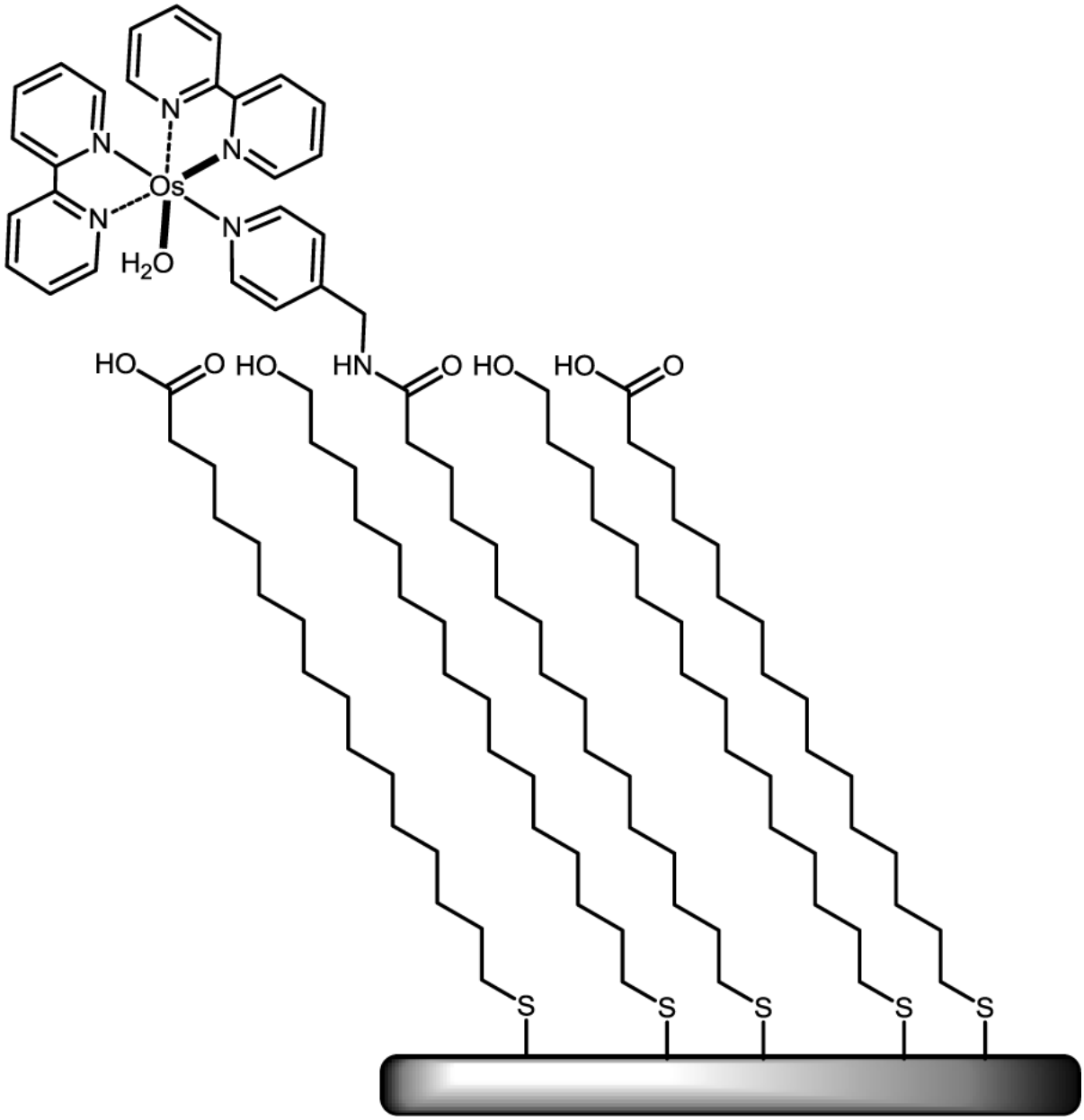

Figure 5.6.
Structure of $[Os(II)(bpy)_2(H_2O)\ (PyMeNHCO(CH_2)_{15}SH)]^{2+}$ monolayer formed via a peptide coupling reaction. Adapted from reference [192].

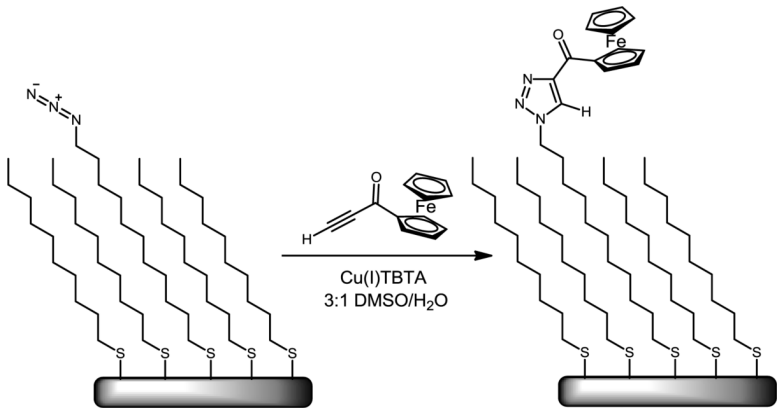

Figure 5.5.
SAM modification with ferrocene using “click” chemistry with a Cu(I)TBTA catalyst (TBTA is tris(benzyltriazolylmethyl)amine). Adapted from reference [305].

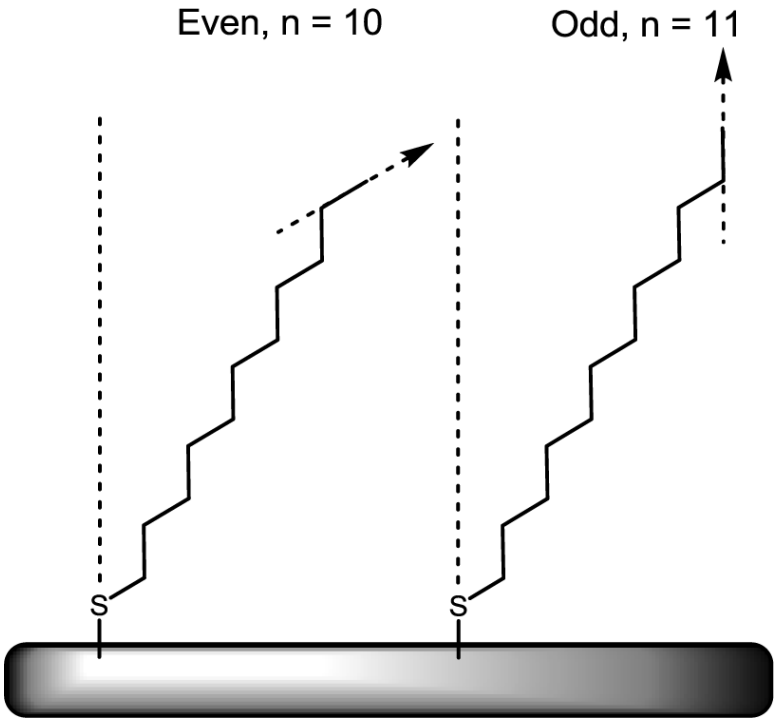

Figure 6.1.
An illustration of the odd-even effect on the SAM structure. For n = odd, the terminal CH_3-CH_2 group is parallel to the surface normal. For n = even, the terminal CH_3-CH_2 group is tilted with respect to the surface normal. Adapted from reference [279].

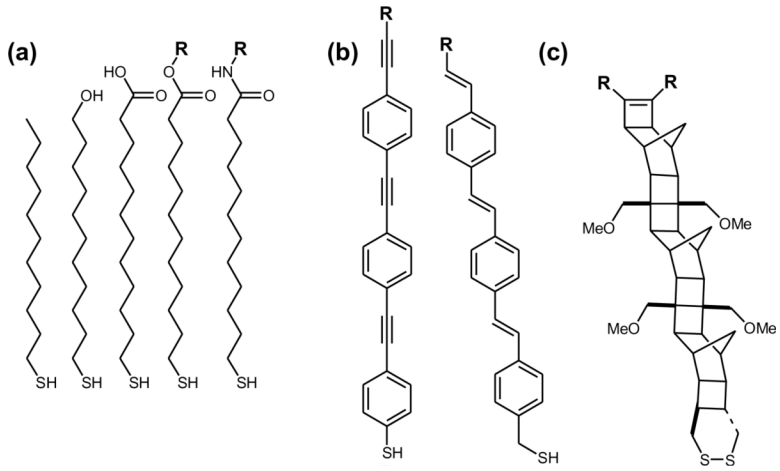

Figure 6.2.

Examples of molecules used to form SAMs where R is the attachment point for the redox center. (a) Aliphatic chains with different terminal functionalities. (b) Rigid molecules of OPE, OPV. (c) A norbornylogous bridge.

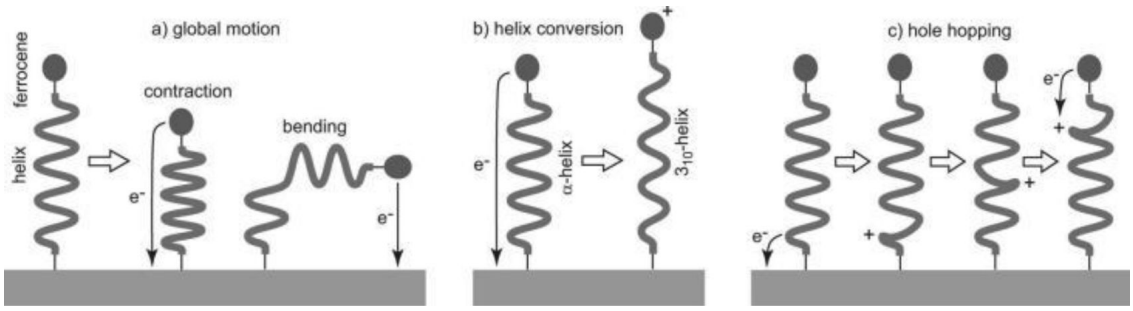

Figure 6.4.
Mechanisms for the molecular dynamics effect on ET. (a) global motion-gated electron tunneling (b) electron tunneling coupled with helix conversion and (c) hole hopping along the amide backbone. Reproduced with permission from reference [80].

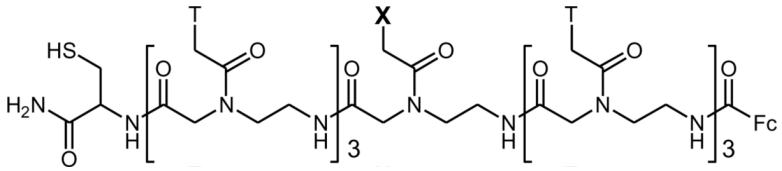

Figure 6.5.
Peptide nucleic acid oligomer with sequence T3-**X**-T3 (**X**=C, T, A, G, CH_3) from reference [136].

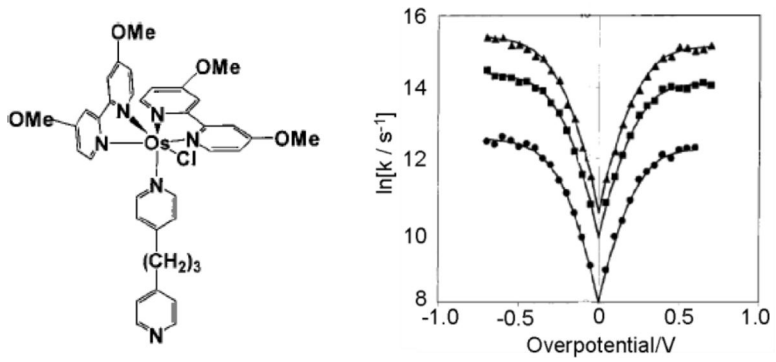

Figure 7.1.
(a) Structure of Os p3p. (b) Tafel plot for Os monolayers adsorbed on Pt (▲), Au (■) and carbon (●). Reproduced with permission from reference [378].

Table 1.1

Comparison of k_{ET} between the electrode and the redox center for ferrocene-terminated alkane bridges measured using different methods. (ILIT=indirect laser induced temperature jump, CV=cyclic voltammetry, ACV=alternating current voltammetry, EIS=electrochemical impedance spectroscopy, CA=chronoamperometry)

reference	ferrocene species in SAM	diluent	# atoms	k_{ET} (s^{-1})	method
45	$Fc(CH_2)_nSH$	$H_3C(CH_2)_nSH$	5	1.6×10^{7}	ILIT
45	$Fc(CH_2)_nSH$	$H_3C(CH_2)_nSH$	6	2.4×10^{6}	ILIT
300	$FcCO_2(CH_2)_nSH$	$H_3C(CH_2)nSH$	7	3×10^{7}	CV
45	$Fc(CH_2)_nSH$	$H_3C(CH_2)_nSH$	8	4.4×10^{5}	ILIT
45	$Fc(CH_2)_nSH$	$H_3C(CH_2)_nSH$	9	1.3×10^{5}	ILIT
299	$FcCONH(CH_2)_nSH$	$HO(CH_2)_nSH$	9	6.6×10^{4}	CV
299	$FcCONH(CH_2)_nSH$	$HO(CH_2)_nSH$	10	1.5×10^{3}	CV
83	$Fc(CH_2)_nSH$	$H_3C(CH_2)_nSH$	10	4×10^{4}	ACV
45	$Fc(CH_2)_nSH$	$H_3C(CH_2)_nSH$	11	1.2×10^{4}	ILIT
299	$FcCONH(CH_2)_nSH$	$HO(CH_2)_nSH$	11	6×10^{3}	CV
83	$Fc(CH_2)_nSH$	$H_3C(CH_2)_nSH$	12	1.7×10^{3}	ACV
299	$FcCONH(CH_2)_nSH$	$HO(CH_2)_nSH$	12	1.2×10^{3}	CV
300	$FcCO_2(CH_2)_nSH$	$H_3C(CH_2)_nSH$	15	100	CV
45	$Fc(CH_2)_nSH$	$H_3C(CH_2)_nSH$	16	28	CV
299	$FcCONH(CH_2)_nSH$	$HO(CH_2)_nSH$	17	7	CV
195	$FcCONH(CH_2)_nSH$	$HO(CH_2)_nSH$	17	9	EIS
1	$FcCO_2(CH_2)_nSH$	$HO(CH_2)_nSH$	18	1	CA

Table 4.1

Reorganization energies (eV) of $[Ru(NH_3)_5pyCH_2NHCO(CH_2)_{15}SH]^{2+}/HO_2C(CH_2)_{15}SH$ monolayers Calculated λ_o was determined using Eq. 2.10. Reproduced from reference [74].

	Anodic λ	Cathodic λ	Calculated λ_o
H_2O	0.9	0.8	0.92
DMSO	0.9	0.7	0.75
acetonitrile	0.9	0.7	0.91
DMF	0.9	0.7	0.9
methanol	0.9	0.7	0.92
ethanol	0.9	0.7	0.85
acetone	0.9	0.7	0.84
propanol	0.6–0.7	0.6	0.81
butanol	0.6	0.5	0.78
THF	0.6	0.5	0.67

Table 6.2

Comparison of rates for oligophenylethynylene (OPE) bridges

reference	*PE units	k_{ET} (s^{-1})	method
57	1	1.5×10^{7}	ILIT
57	2	3.3×10^{6}	ILIT
57	3	6.4×10^{4}	ILIT
57	3*	2.3×10^{6}	ILIT
3	3	5.0×10^{5}	ACV
57	4	1.2×10^{5}	ILIT
3	4	6.0×10^{4}	ACV
3	4*	6.5×10^{4}	ACV
57	5*	3.1×10^{4}	ILIT
3	5	5.0×10^{3}	ACV
3	6	3.5×10^{2}	ACV

* one phenyl is substituted